THÈSE

Pour l'obtention du grade de
DOCTEUR DE L'UNIVERSITÉ DE POITIERS
UFR des sciences fondamentales et appliquées
Pôle poitevin de recherche pour l'ingénieur en mécanique, matériaux et énergétique - PPRIMME (Poitiers)
(Diplôme National - Arrêté du 25 mai 2016)

École doctorale : Sciences et ingénierie en matériaux, mécanique, énergétique et aéronautique - SIMMEA (Poitiers)
Secteur de recherche : Milieux denses, matériaux et composants

Présentée par :
Chennan Jiang

Damage accumulation and recovery in Xe implanted 4H-SiC

Directeur(s) de Thèse :
Jean-François Barbot, Marie-France Beaufort

Soutenue le 12 janvier 2018 devant le jury

Jury :

Président	**Alexandre Boulle**	Directeur de recherche CNRS, Université de Limoges
Rapporteur	**Nathalie Moncoffre**	Directrice de recherche CNRS, Université de Lyon
Rapporteur	**Chonghong Zhang**	Professor, Institute of modern physics, Chinese academy of sciences
Membre	**Jean-François Barbot**	Professeur des Universités, Université de Poitiers
Membre	**Marie-France Beaufort**	Directrice de recherche CNRS, Université de Poitiers
Membre	**Erwan Oliviero**	Ingénieur de recherche CNRS, Université de Montpellier

Pour citer cette thèse :
Chennan Jiang. *Damage accumulation and recovery in Xe implanted 4H-SiC* [En ligne]. Thèse Milieux denses, matériaux et composants. Poitiers : Université de Poitiers, 2018. Disponible sur Internet <http://theses.univ-poitiers.fr>

THESE

Pour l'obtention du Grade de

DOCTEUR DE L'UNIVERSITE DE POITIERS

(Faculté des Sciences Fondamentales et Appliquées)
(Diplôme National - Arrêté du 25 mai 2016)

Ecole Doctorale : Sciences et Ingénierie en Matériaux, Mécanique, Énergétique et Aéronautique

Secteur de Recherche : Milieux denses, matériaux et composants

Présentée par :

CHENNAN JIANG

****

DAMAGE ACCUMULATION AND RECOVERY IN Xe IMPLANTED 4H-SiC

****

Directeurs de Thèse : J. F. BARBOT et M. F. BEAUFORT

****

Soutenue le 12 janvier 2018

Devant la Commission d'Examen

****

JURY

C. Zhang	Professeur, IMPCAS, Lanzhou, Chine	Rapporteur
N. Moncoffre	Directrice de recherche, IPNL, Lyon	Rapporteur
E. Oliviero	Ingénieur de recherche, ICG, Montpellier	Examinateur
A. Boulle	Directeur de recherche, SPCTS, Limoges	Examinateur
M. F. Beaufort	Directrice de recherche, Pprime, Poitiers	Examinateur
J. F. Barbot	Professeur, Pprime, Poitiers	Examinateur

Acknowledgements

I have been fortunate to meet many people to carry out the work reported in this Ph.D. thesis. They give me some friendly help, teach me some useful experience; and guide me in the right direction. I would like to acknowledge sincerely from my heart for all of them.

This work was financed by the organization of China Scholarship Council (CSC) and supported by University of Poitiers in Institute Pprime, directed by Pr. Jean-François Barbot who was also my supervisors. I would like to first deeply grateful for his encouragement. He is an excellent leader who owns full of the advantages for always active, attentive in academic, and friendly all the time. I have been influenced by this mind not only for the work and also for all my life. Secondly, I would like to appreciate my co-supervisor Marie-France Beaufort, who is always elegant. Thanks to her for carrying out the TEM measurements which were a very important and indispensable part of my study. Through their guidance, understanding, and patience that this work could be completed.

I would like to thank Mrs. Nathalie Moncoffre for reading this thesis. Her critical remarks on both physics and language have been invaluable. Also, thank Pr. Chonghong Zhang, to be also a referee and to give me a favorable opinion for the defense, although he did not come to my defense. I would like to thank M. Alexandre Boulle for accepting to be the president of my thesis defense jury. Also, he has helped me to simulate the XRD and obtained the strain profile with his program. I would like to thank M. Erwan Oliviero for his participation in the jury and for his critical comments on the work.

During the three years of my Ph.D. study, I was fortunate to work with a very dynamic and friendly team. Of course, I would like to thank again my two supervisors Marie-France Beaufort and Jean-François Barbot. Many thanks to Alain Declémy, who has taught me given me the XRD theoretical and measurement, and always provided interesting discussions. Many thanks to Marc; I took a lot of time to implant many SiC samples with help of him. Many thanks for adorable Anne-Marie, to help me carrying out the TEM sample preparations. Many thanks for Julien, who especially gave me some help for my first year.

I am indebted immeasurable to many of my friends Ph.D in this laboratory. I was happy for each wonderful moment with them during these years; they are Benjamin, Senda, Romain, Romuald, Florien, Julien, Aurelie, Maxime, Jean-Rony, Daouda, Damien, Hewei, Elodie, and Raphaël.

Especially, I am heartily thankful to my friends in France who consistently present for filling the void created by the absence of my family in China. Dr. Jian Wu, Dr. Yu Fan, Dr. Hangxiang Wu, and Dr. Pascal Lefevre who share me with their Ph.D. experience. I would like to thank my brother

Tao Wang and his wife Xichao Yu, who comes to see us from Tours. And thank Dr. Zhiyong Zhou and his wife YYY has already come back to China.

Last but not the least; I would like to thank my family: my parents Jianrong JIANG and Yongli WANG for giving birth and supporting me spiritually throughout my life, to thank two very important honey who always wait me at home: my wife Yuzhen TIAN-JIANG (big honey) and my daughter EMMA Shiyan JIANG (little honey).

Content

Introduction 5

Chapter 1 Background and literature review 9

1.1 Properties of SiC 10

1.1.1 Structural properties 10

1.1.2 Main properties of SiC 12

1.2 SiC applications 13

1.2.1 Device processing and implantation 13

1.2.2 Nuclear energy systems 16

1.3 Previous studies of implantation into SiC 19

1.3.1 Amorphization of SiC 20

1.3.2 Influence of the temperature of implantation 22

1.3.3 Damage models in ceramics 23

1.3.4 Disorder in SiC with increasing temperature of implantation 26

1.3.5 Thermal annealing and recovery of defects 28

1.3.6 He implantation in 4H-SiC 28

1.3.7 Heavy gas implantation in SiC 32

1.4 Conclusions 33

Chapter 2 Experimental methods 35

2.1 Ion implantation 36

2.1.1 Interaction process 36

2.1.2 SRIM simulation 38

2.1.3 Implantation experimental details 40

2.2 X-ray Diffraction (XRD) 42

2.2.1 X-ray Diffraction technique 42

2.2.2 X-ray diffraction curves 43

2.2.3 X-ray diffraction simulation 45

2.3 Surface measurement 46

2.3.1. Technical description of scanning broadband interferometry 46
2.3.2. Procedures for operating the scanning broadband interferometry 47
2.3.3. Step height estimation 48
2.3.4. Roughness measurement 49
2.4 Transmission Electron Microscopy (TEM) 50
2.5 Thermal annealing 52
Chapter 3 Results and discussions 57
3.1 General results 58
3.1.1 TDS measurements at 1350 °C 58
3.1.2 X-ray diffraction simulations 61
3.2 Damage evolution in the low temperature regime 63
3.2.1 Room temperature Xe-implantations 64
3.2.2 Temperature of implantation up to 300 °C 67
3.2.3 Discussion on the low temperature regime of implantation 72
3.3 Damage buildup for implantations at 400 °C 74
3.3.1 Low and medium dose regimes (< 6dpa) 74
3.3.2 High dose regime (6 to 30 dpa) 80
3.3.3 Discussion on the damage buildup at 400°C implantation 82
3.4 Evolution upon subsequent annealing 83
3.4.1 Low dose, 1 dpa 83
3.4.2 Medium doses, 3 and 6 dpa 85
3.4.3 High dose, 15 dpa 88
3.4.4 Discussion of strain and swelling recovery under annealing 89
3.4.5 TEM observations 91
3.4.6 Summary of defect evolution upon annealing 96
3.5 Strain evolution for implantation at higher temperatures (400-800 °C) 96
Conclusion 99
Reference 103

Introduction

Since the origins of mankind, the development of materials symbols the progress of the world. From the use of stone tools called ‘‘Stone Age’’, with the progress of mankind, there are ‘‘Bronze Age’’, ‘‘Iron Age’’ and ‘‘Steel Age’’. The materials characterize the point for each age. Material science and engineering is a major pillar of modern civilization. Ceramics, composites, polymers, metal alloys and semiconductors are mainly used in modern industry for nearly a century. Their properties can change according to how the material is treated. With the world development, industrial production, the sustainable energy they are indispensable for daily life. The human beings demand more than more the consumption in the recent years. The energy crisis is becoming a great problem. The issue of materials has always been one of the major bottlenecks restricting the development of science and technology in the future. Silicon carbide (SiC) is a material which can be well competent in some high technology areas. It is because the SiC can be considered as a semiconductor or as a ceramic for its good properties.

Implantation of energetic particles into target materials can lead to microstructural (via collision cascades) and chemical changes thereby affecting their physical, chemical, and mechanical properties as well their dimensions (swelling). This technique is largely used in many fields as the microelectronics industry, in the surface modifications, or to simulate the behavior of materials under a harsh environment (in space or in nuclear power plants).

Silicon carbide (SiC) is used for a long time as abrasive powders. More recently due to the waste improvements in the material properties, SiC has gained more attention as a wide band gap semiconductor with a potential to replace Si in power devices and in devices operating at elevated temperatures. However, the fabrication of electronic devices requires the use of ion implantation for which the major drawback is the as-induced defects that are difficult to remove even after high-temperature annealing or to restore the crystallinity of the crystal. Implantation at high temperature can reduce the induced defects but it is not feasible in industrial ion implanters. Understanding the formation/evolution of such defects is thus of crucial importance to improve the device performances. But, SiC is also a ceramic making it well adapted to a hostile environment in particular in the nuclear system (fission or fusion) due to its low cross-section for neutron-capture. It has thus been proposed as the structural components in nuclear fusion reactors or as an encapsulating material for nuclear fuel. The new reactors must be designed with specific objectives including sustainability, safety, and reliability - nuclear energy is considered as an important resource in managing atmospheric greenhouse gases and associated climate change. In nuclear applications, SiC would be exposed to energetic fission products such as heavy ions and light ions derived from transmutation reactions. Again the in-depth understanding of the behavior of structural irradiation-induced defects is required to make accurate predictions of the material degradation under operative conditions.

The behavior of helium and therefore the helium implantation damage in the 4H-SiC single crystal has been the subject of several studies within the Institute. This thesis deals with noble gas (NG) implantation induced defects in 4H-SiC according to the conditions of implantation (temperature and fluence). The focus has been put on xenon implantation at 400 °C for which amorphization of SiC is avoided – amorphization processes have been studied by several groups around the world by mainly using ion beam channeling. Xe is an inert gas and thus chemical effects are avoided. In addition by comparing with helium implantation previously studied by the group in Poitiers (Pprime) the ratio vacancies/xenon is high, thus minimizing the effect of the gas itself. Accumulation of damage as well as recovery processes with temperature and fluences have been studied. X-ray diffraction (XRD) has been used to study the level of damage resulting from implantation especially in the low fluence regime while transmission electron microscopy (TEM) has been chosen to study the defects and their evolution upon annealing in the high fluence regime. The as-resulting surface swelling was measured when possible.

The thesis consists of three chapters. Chapter 1 presents the material (SiC) and its physical properties; it also discusses some results previously obtained on the damage accumulation up to the amorphization as well as the phenomenological models to describe the evolution of the amorphous fraction with dose. The main results concerning previous works on helium implantation are also briefly summarized. Chapter 2 is devoted to the experimental methods used in this work (ion implantation and SRIM simulations, XRD, TEM, interferometry, annealing). Some results are also presented to validate the choices of experimental conditions we used. The last chapter focuses on results and discussions. It is divided into different subchapters according to the condition of implantation and annealing for clarity; each is followed by a short discussion. A general conclusion ends the manuscript.

This work has been done in collaboration with other laboratories and other groups inside the Pprime Institute with great help and direction by J. F. Barbot and co-direction of M.F. Beaufort who did the conventional and high-resolution TEM. All the noble gas (NG) implantations were carried out in the Institute. The TDS measurements were performed at Bordeaux by E. Gilabert; RBS at Orsay by A. Debelle and some recent XRD simulations by A. Boulle at Limoges. The modifications of mechanical studies under Xe implantation at room temperature were also studied with the help of V. Audurier and C. Tromas (Pprime Institute); the results are not presented in the manuscript but have been submitted to the publication (accepted, in press). During my Ph.D. I made the sample preparations, the XDR measurements and some simulations of XRD spectra (with the help of A. Declémy), developed the model of damage accumulation, performed the step high measurements, conducted all the annealing experiments. This work has already led to two publications following international conferences (EMRS-2015 and EDS2016, Extended Defects in Semiconductors). I also

had the chance to present a part of my results at the international conference of ceramic in Guilin (November 2015).

This work has been financed by the China scholarship council. I have also benefited from the doctoral school (SIMMEA) for a short stay at the Institute of Modern Physics (IMP) at Lanzhou in China (Prof. Zhang).

Chapter 1

Background and literature review

1.1 Properties of SiC

Silicon carbide is an almost exclusively artificial mineral that is composed of silicon and carbon. In nature, SiC exists in the form of extremely rare minerals such as moissanite, in the meteorites and etc., but in a very small quantity. Most all of the silicon carbide is synthetic, including the moxi stone which is made for jewelry. Thanks for the properties of SiC, it can be considered as a semiconductor or a ceramic. Thus it is a very multi-proposed material either for electronic applications since large single crystals grown by the Lely method [1] are now available on the market or in applications requiring high endurance.

1.1.1 Structural properties

The fundamental structural unit of silicon carbide is a covalently bonded primary coordinated tetrahedron, see figure 1.1. The four bonds directed to the neighbors have a nearly purely covalent character (ionic contribution of about 12 %). The most remarkable feature of silicon carbide crystal structure is its polytypes that is that the crystal structure exhibits a number of different one-dimensional ordering sequences without any variation in stoichiometry. It exists in about 250 crystalline forms that are viewed as layers stacked in a given sequence. It is now acceptable to refer to the cubic polytypes as β-SiC and to all non-cubic structures (hexagonal and rhombohedral) collectively as α-SiC.

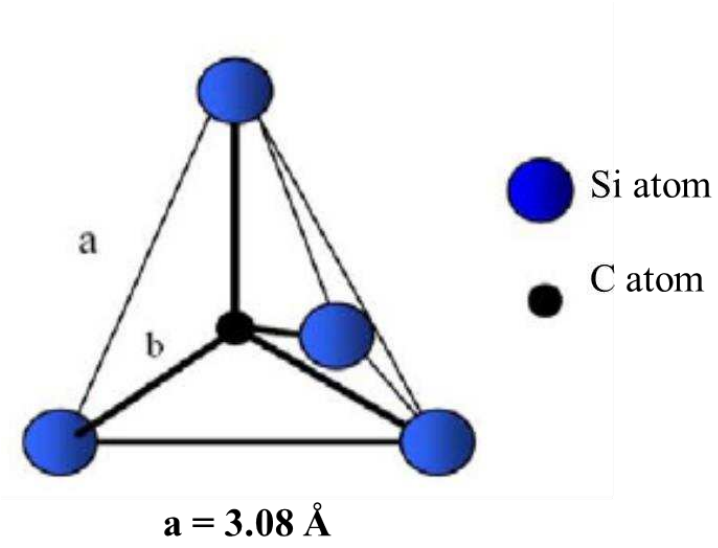


Figure 1.1: The tetragonal cell of SiC. The length of each bond a is approximately 3.08 Å, and the distance of C - Si is 1.89 Å.

For all polytypes, the SiC tetrahedron has a length **'a'** of about 3.08 Å. So for each distance of the neighboring silicon atom is the same. The carbon atom locates at the center of the tetrahedron. The distance between the carbon atoms to each silicon atom is about 1.89 Å. But the height **'c'** of the cell is different according to the structure, so the ratio c/a differs for each polytype, see table 1.1. Different structures arise as a consequence of the fact that by a characteristic succession of alterations of

tetrahedral layers, a repeating unit is formed. If every second layer is parallel to the preceding layer, the cubic structure is formed, and if every second layer is antiparallel to the preceding, the hexagonal type is obtained.

Polytypes	3C-SiC	4H-SiC	6H-SiC
Network	Cubic	Hexagonal	Hexagonal
Lattice constants (Å)	a = 4.349	a = 3.08 c = 10.05	a = 3.08 c = 15.079
Sequence	ABC	ABCB	ABCACB

Table 1.1: Characteristic of the most common polytypes of silicon carbide

All the SiC polytypes are formed by the stacking of close-packed planes of double layers of Si and C atoms, as referred to as A, B, and C in figure 1.2. Different stacking orders of the close-packed double layers are possible giving rise to the variety of different polytypes. In the Ramsdell's notation, the one commonly used in the microelectronics industry, the notation specifies both the number of layers in the repeat along the stacking direction, together with Bravais lattice type of the resultant structure (i.e., hexagonal (H), cubic (C), or rhombohedral (R)). For example, 4H has four close-packed layers in a hexagonal unit cell that is repeated. The stacking sequence is "ABACABACABAC…", see figure 1.2.

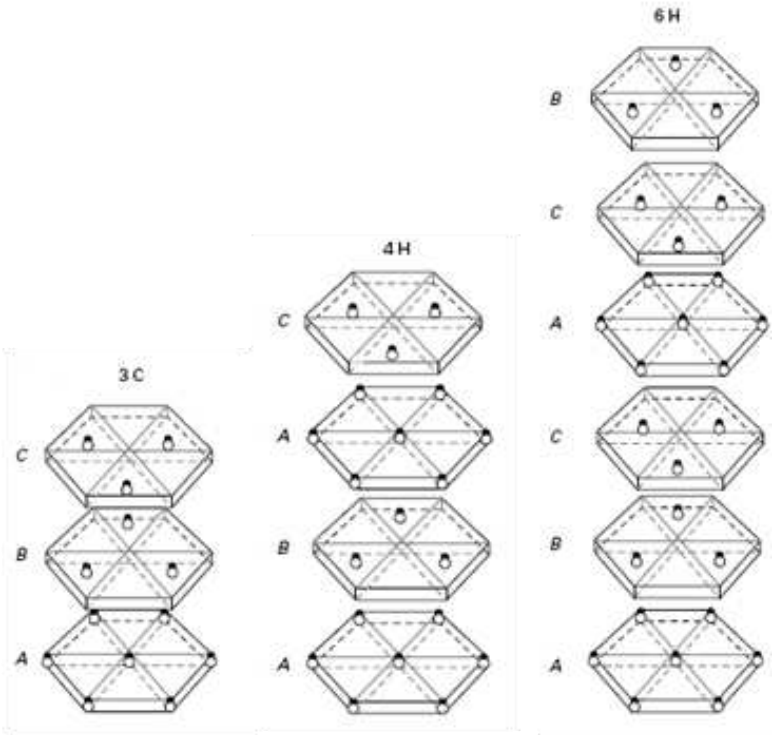


Figure 1.2: One stacking period of the three main polytypes 3C-, 4H- and 6H-SiC with different stacking orders.

1.1.2 Main properties of SiC

To evaluate the interest of SiC in the field of microelectronics, it is important to compare with others commonly used semiconductors, for example, silicon or gallium arsenide, and with other wide band gap semiconductors in development such as GaN, diamond, and ZnO. Table 1.2 reports some important properties of the most common polytypes of SiC and the other semiconductors commonly used. Historically, the main difficulty with SiC was the formation of micro-pipes which were essentially small holes of diameter ~ 1 μm running through the wafer from top to bottom. However, SiC-wafers of zero micro-pipe density is now available allowing fabricating devices of several square millimeters with reasonable yield.

	4H-SiC	3C-SiC	6H-SiC	Si	GaN	GaAs	Diamond
Density ($g.cm^{-3}$)	3.21	3.21	3.21	2.33	6.1	5.3	3.52
Melting point (K)	3100	3100	3100	1690	2770	1690	3820
Band gap at 300K (eV)	3.27	2.4	3.02	1.12	3.4	1.4	5.5
Electron mobility at 300K ($cm^{-2}.V^{-1}.s^{-1}$)	800	1000	370	1100	900	6000	2200
Electron saturated velocity (10^7 $cm.s^{-1}$)	2	2.5	2	1	2.7	1	2.7
Breakdown electric field (10^6 $V.cm^{-1}$)	2.2	2.12	2.5	0.25	5	0.4	10
Thermal conductivity ($W.cm^{-1}.K^{-1}$)	4.9	5	4.9	1.5	1.3	0.5	20
Static dielectric constant ($\parallel$C)	9.7	9.72	9.66	11.8	9	12.8	5.5
Hardness ($kg.mm^{-2}$)		3980	2130	1000	1200-1700 [2]	600	10000
Young's modulus (GPa)	392-694 [3][4]	392-694	392-694	130-188	271	85.5 SMS	1050-1210 [5]
Refractive index (nD)	2.55	2.55	2.55	3.44	2.24	3.8	2.418

Table 1.2: Physical properties of the common polytypes of SiC compare with silicon, GaN, GaAs and diamond.

One characteristic the most important for semiconductors is the width of the band gap, it refers to the distance between the band of conduction and of valence. The intrinsic conductivity is related to the width of the energy gap E_g, and only electrons with enough energy can be excited from the valence band, across the energy gap and transit to the conduction band. The large band leads to a low intrinsic carrier concentration even at **high temperature**. The indirect band gap of SiC has a beneficial effect on the lifetime of carriers. SiC is also very well adapted to **high power devices**. It resists at a high electrical voltage, about eight times higher than GaAs and Si in the absence of undergoing avalanche breakdown. The drift velocity of the electrons saturation is two times higher than Si that is well adapted to realize **high-frequency devices**. SiC offers several advantages compared to other wide band gap semiconductors including the commercial availability of substrates, known device processing techniques, and the ability to grow a thermal oxide for use as masks in processing, device passivation layers, and gate dielectrics.

The high thermal conductivity of SiC, close to 500 W/m.K so exceeding that of Cu, is also very attractive for high-temperature applications; it implies a higher efficiency of heat extraction from the device as well as a further reduction in the requirements for the device cooling. Its excellent thermal conductivity coupled with a low thermal expansion gives it a good thermal shock resistance.

The mechanical properties of SiC, its hardness and its corrosion resistance especially, are also excellent and today it is used in abrasive machining processes and numerous high-performance applications. In thin film, it can also be used as hard coatings to protect materials and to increase the lifetime and efficiency of cutting tools.

SiC is also a material of interest for fundamental nuclear materials science investigation as well as space conquest, due to its extraordinary resistance to irradiation whether in composite or in monolithic form. Today SiC is a major material in the advanced energy system. For example, the ITER (International Thermonuclear Experimental Reactor), the nuclear fusion reactors, the gas-cooled fission reactors and the encapsulating the nuclear fuel TRISO in case of high-temperature reactors [6].

For all these advanced technologies, a significant problem concerns irradiation damage and how it affects the material properties. More reliable data is necessary to enhance the development of SiC in both nuclear and electronic applications.

1.2 SiC applications

1.2.1 Device processing and implantation

As previously written (table 1.2) large bandgap semiconductor materials like SiC develop superior material characteristics compared to silicon and are therefore about to get of economic

importance in the near future. The SiC Schottky diode was the first successfully commercialized SiC power device; however, SiC JFET (Junction Field Effect Transistor) and SiC MOSFET (Metal Oxide Semiconductor Field Effect Transistor) are now currently commercialized. The considerable development effort is put into the understanding of how to fabricate devices based on this material. One ingredient is the knowledge how ion implantation can affect and tailor their semiconductor properties in a suitable manner. Because of the low coefficient of diffusion of dopants in SiC, this technique is widely used in SiC devices manufacturing. High-temperature annealing is then carried out to achieve maximum dopant activation of donors or acceptors. P-type implantation doping is achieved with both Bore (B) and Aluminum (Al). Nitrogen (N) and Phosphorus (P) act as shallow donors in SiC when residing at carbon and silicon lattice, respectively. High-temperature annealing (~ 1700 °C) is supposed to be sufficient to achieve an optimal degree of donor activation. Higher annealing temperature causes thermal decomposition of the SiC surface and is, therefore, not suitable for device processing. However, high fluence ion implantation induces the formation of defects (or damage) that is very stable in SiC and thus it is difficult to restore the crystallinity of the crystal even after a high temperature of annealing. Dislocations and large defects in a high density can be observed after annealing, see figure 1.3 [7]. In addition, the propagation of stacking faults under forwarding bias is a major problem related to SiC-based devices; it can lead to device failure [8]. Implantation at elevated temperature (400 - 600 °C) reduces the creation of defects and enhances the dopant activation [9].

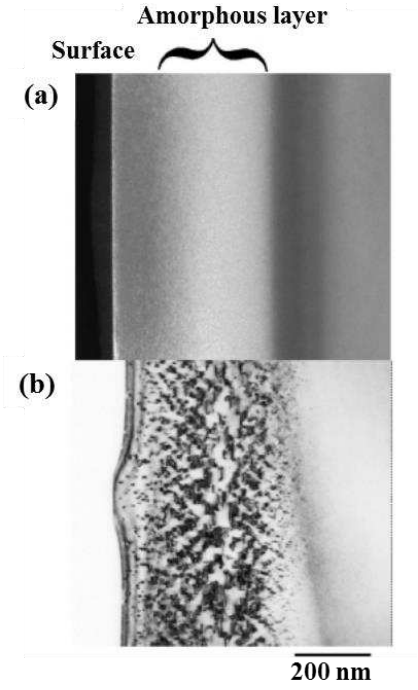


Figure 1.3: Dark field XTEM image of (0001) implanted 4H-SiC with 400keV-1x10^{15} $P^{+}.cm^{-2}$ at RT (a) and annealing at 1700 °C for 15 min. under Ar flow(b) [7].

The Smart Cut™ process allows fabricating semiconductor on insulator structure by using the light ion implantation. This process combining wafer bonding and implantation was firstly developed for silicon substrates at CEA-LETI [10]. It uses hydrogen implantation as an "atomic scalpel" to split from the bulk substrate a thin-layer via the formation of a damaged layer at a well-defined depth,

controlled by the energy of incident ions. A post-implantation annealing allows the formation and propagation of cracks developing laterally due to stiffener (preventing any blistering effects by strengthening the superficial implanted layer). This process extends beyond the silicon world and SiCOI (Silicon Carbide-On-Insulator) can be engineered [11]. SiC wafers are implanted with fluence close to 10^{17} cm^{-2} and then annealed at temperatures close to 1100 °C during which bubbles form. Their huge pressure favors the splitting of the SiC wafer and its transfer onto a handling wafer to create the final structure, see figure 1.4. An additional annealing is performed to stabilize the interface by strengthening the chemical bonds between the oxide layers [12]. The efficiency of the Smart Cut™ process and the quality of the thin film depends on the control and evolution of the implantation-resulting defects.

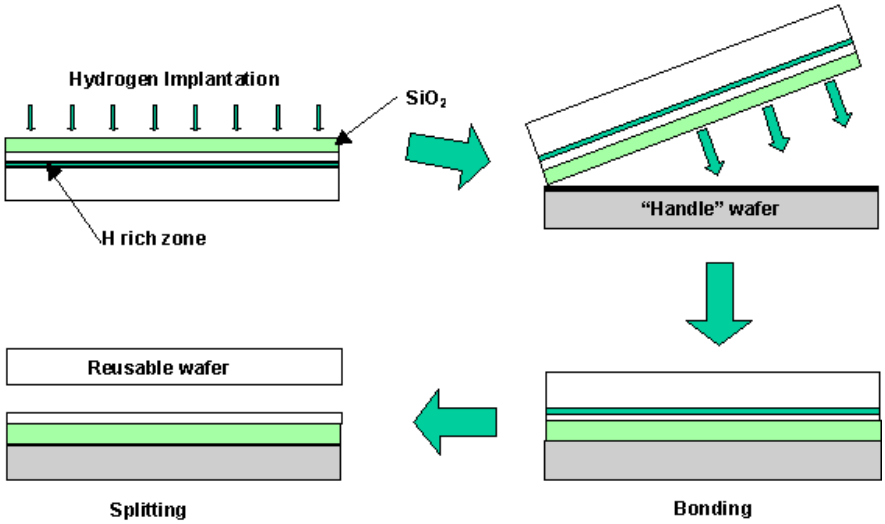


Figure 1.4: A schematic represen*tation of the Smart Cut™ process* [13].

Implantation of SiC can also be used for lowering the graphitization temperature of SiC (T_G ~ 1300 °C), by at least 100 °C [14]. By implanting Si, the decrease in graphitization is supposed to result from the enhancement in Si sublimation associated with broken Si-C bonds and crystal damage at the SiC surface. A more recent use of ion implantation lies in the elaboration of diluted magnetic semiconductor (DMS) for spintronic applications. The implantation of Fe^{+} at elevated temperature into 6H-SiC at fluences close to 10^{16} cm^{-2} is studied in the team PDP (Physic of Defects and plasticity) of the Pprime institute. The correlation between implantation-induced defects and dopants is studied in collaboration with other laboratories (GPM-Rouen). More recently the formation of Fe_3Si nano-sized clusters has been found to be responsible for the main part of the magnetic properties observed after annealing [15].

SiC is also used as a native substrate in growth for GaN, for LED and high-frequency and also for high-power applications due to the weak lattice mismatch ($\Delta a/a$ ~ -3.5 %). GaN grown on a SiC substrate may have about 10^{8} defects (or dislocation density) per square centimeter. The main limitation of silicon carbide lies in its high cost.

1.2.2 Nuclear energy systems

In fission, an atom is split into two or more smaller, lighter atoms. Today, fission is used in nuclear power plants. As we can see figure 1.5, many kinds of fission products are produced after fission nuclear reaction, such as Xe which behavior has been studied especially in this work. Radiation-induced deterioration of fission reactors is thus dominated by displacement damage due to the heavy mass of products. Fusion, in contrast, occurs when two smaller atoms fuse together, creating a larger, heavier atom. Assuming D-T (deuterium-tritium) fusion, a single fusion event releases a 14.1 MeV neutron and a 3.5 MeV helium nucleus. The inner surface of the wall will be thus subject to high flux of α-particles escaping the confinement. In both fusion and fission, energetic neutrons can interact with the structure and can lead to radiation damage (Frenkel pairs) and can also cause nuclear reactions which may produce a considerable concentration of foreign atoms. In particular, helium is produced in a high concentration by (n, α) reactions and can thus cause drastic property change of the irradiated materials. Numerous studies were conducted in metals during the 90's. It is now well-known that helium in metals precipitates into bubbles due to its low solubility. The fundamental aspects of inert gases in solid have been the subject of an international workshop in 1990 and a book was edited [16].

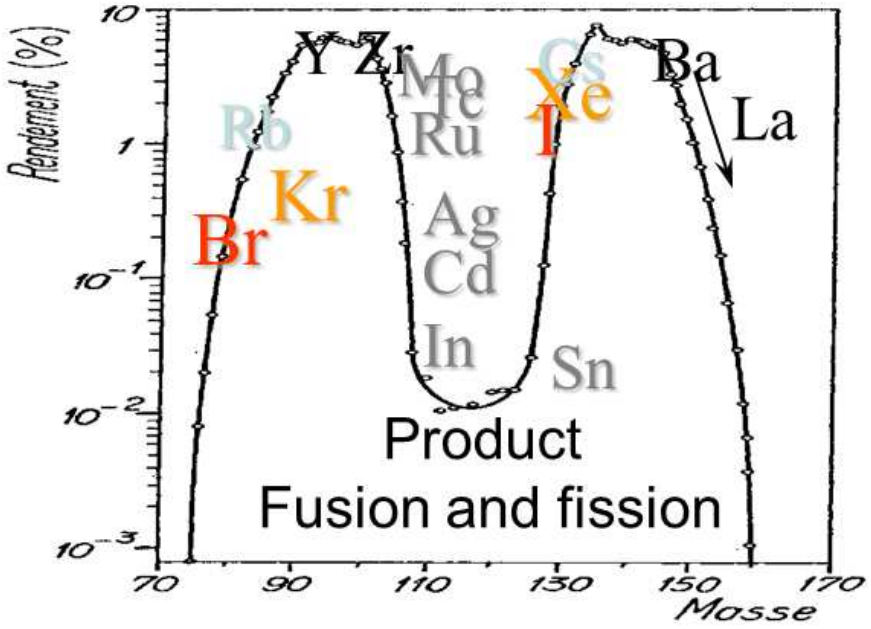


Figure 1.5: Distribution of atomic masses of fission products of uranium.

The intrinsic properties of SiC (including fiber-reinforced SiC-matrix [17]) as the high temperature of melting point, the stability, the neutron transparency and the slow oxidation provide SiC many advantages for nuclear applications in both fusion and fission systems.

However, SiC is brittle and it is essential to take into account how mechanical and physical properties are affected by radiation and temperature. In addition, swelling under irradiation must be

anticipated in SiC design. Figure 1.6 shows the variations of swelling with temperature and for different neutron doses [18]. With increasing temperature, the irradiation-induced swelling decreases according to the reduction of the number of defects surviving the cascade. Then for temperature exceeding ~ 1273 K a non-saturated void-swelling occurs. The underlying phenomena ascribed to the swelling are however not so well described to anticipate the material behavior for a nuclear application view.

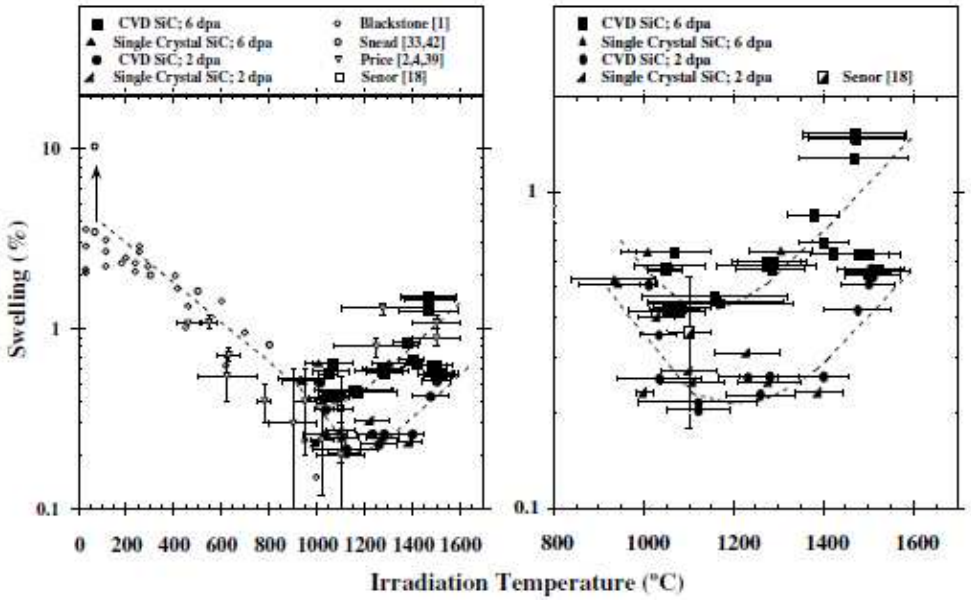


Figure 1.6: Volumetric swelling of SiC as a function of neutron irradiation temperature [18].

Helium is known to have a decisive effect on the resulting microstructure of SiC after implantation and subsequent annealing. The formation of a dense population of bubbles and dislocation loops form at relatively low displacement doses into helium implanted α - SiC while no visible damage appears after proton irradiation under similar conditions [19].

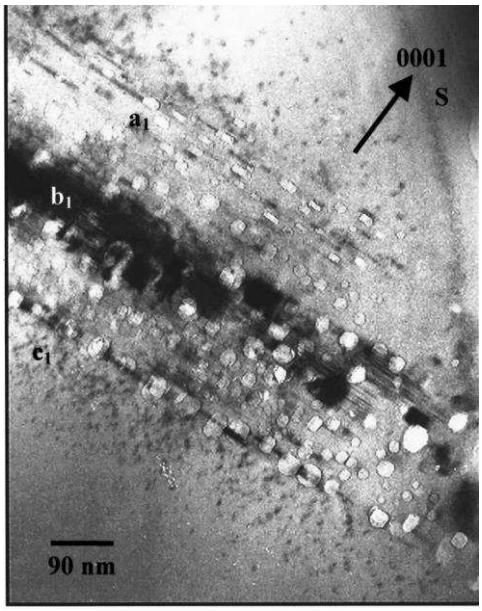


Figure 1.7: Brightfield XTEM image observed into 4H-SiC implanted with 1 x 10^{17} He.cm^{-2} at 1.6 MeV and then annealed at 1500 °C-30 min. The zones labeled a_1, b_1 and c_1 indicate the different morphologies of observed bubbles [20].

Different types of bubble configuration are reported according to their location: grain boundaries, depleted zones along GB's, and the grain interior, as well as to the conditions of implantation: fluence, annealing temperature and time. Many studies have been conducted at the Pprime institute to understand the formation of helium-bubbles into 4H-SiC. As an example, Oliviero et al. [20] showed that the form (size, shape, and density) of bubbles also depends on their localization under high fluence implantation at RT and annealing at 1500 °C, figure 1.7. The recrystallization leading to polytypism transition is observed as the formation of 3C-SiC inside the damaged zone. The different studies on helium implantation into 4H-SiC will be detailed in the next paragraph (& 1.3).

ITER (International Thermonuclear Experimental Reactor)

ITER is a nuclear fusion research reactor project located at Cadarache (Bouches-du-Rhône) in France. With ITER an important step towards the production of energy will be crossed. But for that, many technologies need to be developed, in particular in the choice of materials because of the temperature of the plasma that will reach one hundred million kelvins. Even if the plasma is confined by a magnetic field the walls will be heated by the particles resulting from the nuclear reactions and by the thermal radiation emitted by the plasma, they must, therefore, be permanently cooled [21]. Figure 1.8 shows a schematic view of ITER.

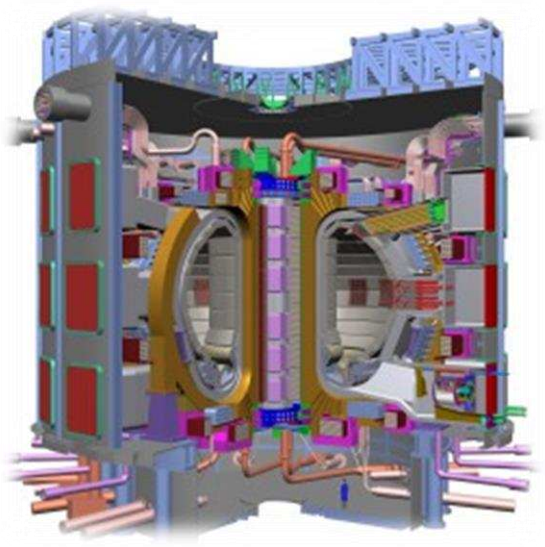


Figure1.8: Section view of Tokamak ITER.

The main features of ITER
Thermal power of the fusion: 500 MW
Plasma volume: 840 m^3
Toroidal magnetic field: 5.3 T

TRISO (tristructural – isotropic) Nuclear Fuel

With the decreasing fossil fuel supply, the problem of greenhouse gas emission coupled with an increasing energy demand, alternative energies have to be enhanced. In nuclear energy systems, one alternative is the use of High Temperature Gas-cooled Reactors (HTGR) or very high temperature reactors (VHTR) that are Generation IV reactors using helium as a coolant. They use encapsulated fuel particles to prevent any release of fission products like cesium, iodine sliver, and strontium. The

particle is termed TRISO (TRi-ISOtropic), and its schematic is presented in figure 1.9. The fuel kernel contains a mixture of uranium oxide and uranium carbide that is surrounded by a 100 µm thick porous graphite buffer layer with three different isotropic coating layers with its own functionality. They are 40 µm thick of a low density of inner pyro-carbon layer to accommodate kernel swelling (impermeable to gaseous fission products), 35 µm thick CVD SiC layer and another 40 µm thick outer pyro-carbon layer [22]. The main function of SiC layer is to act as a diffusion barrier to prevent the release of radioactive fission products. SiC layer could be retaining most fission products and is, therefore, an essential safety feature. Maintaining its integrity throughout the operative lifetime is thus essential. The SiC layer is synthesized by the decomposition of methyltrichlorosilane (MTS) in a hydrogen environment at a temperature between 1450 and 1550 °C resulting in the highest strength and Young's modulus of SiC; SiC is of cubic structure (β-SiC) [23]. The grain size increases with higher deposition temperature and with a thickness of the layer. There are thus some effects of grain boundary for the network properties occurred when the Ag across the SiC layer and escape from the fuel particle [24]–[26].

As described above, the TRISO particle uses a SiC coating as the main structural layer of the fuel particle and its properties have therefore been subject to research over the past decade.

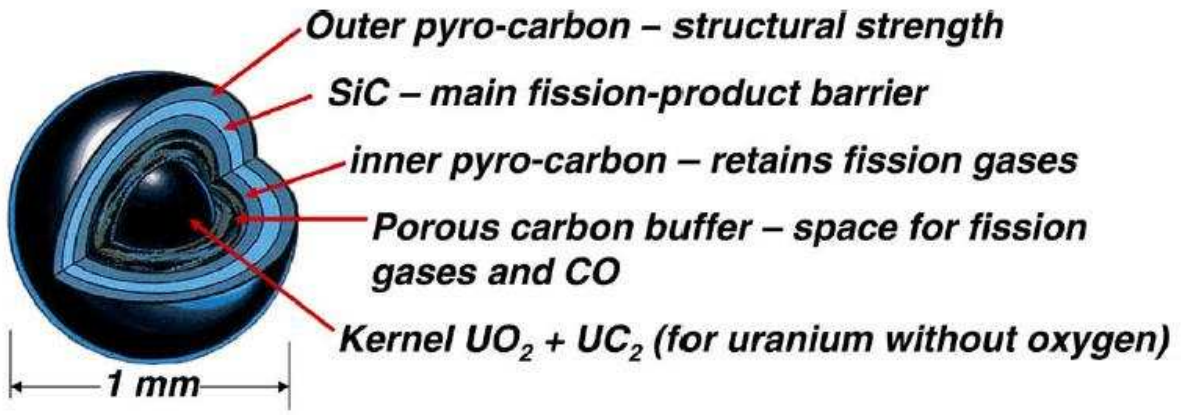


Figure 1.9: TRISO fuel for the VHTR.

1.3 Previous studies of implantation into SiC

Numerous works have been conducted to study the damage and the implantation-induced defects as well as their evolution upon subsequent annealing. The major disadvantage of implantation and irradiation is the production of defects. Most of these studies are based on RBS/C and TEM observations (techniques described in the next chapter). XRD is also used to determine the resulting as-induced strain; this technique has been particularly used in a previous work conducted in the Pprime institute on He-implanted SiC (Ph.D. Stéphanie Leclerc).

1.3.1 Amorphization of SiC

The amorphous transition under irradiation takes place when a critical defect density is exceeded. At RT, implantation of SiC leads to the amorphous transition. Amorphization induces a decrease of the SiC density leading thus to a volume expansion or a surface swelling in case of implantation. The mechanical properties: hardness, Young's modulus, fracture toughness and tribological properties are also affected by the implantation [27].

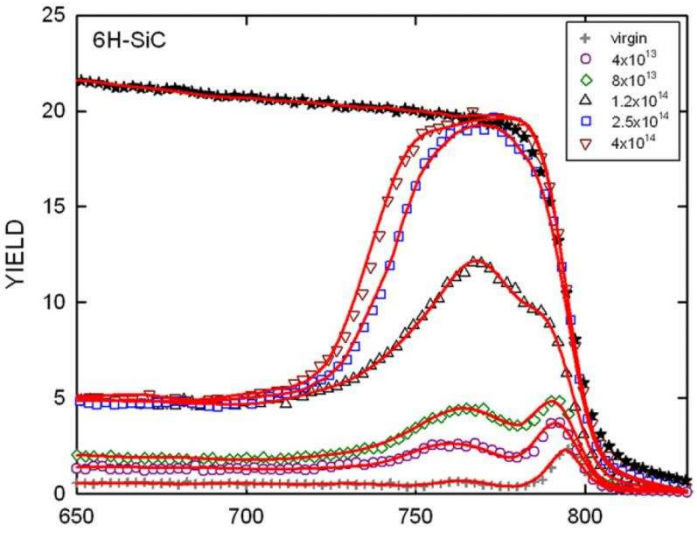


Figure 1.10: RBS spectra of 6H-SiC implanted at RT with 100 keV Fe ions with increasing fluence up to the amorphization [28].

Rutherford backscattering spectrometry channeling (RBS/C) is a useful technique to estimate the integration of the amorphous layers. Figure 1.10 shows an example of RBS/C spectra with increasing fluences up to the amorphization [28]. At a fluence of 2.5 x 10^{14} Fe.cm^{-2} the full disorder is observed, i.e. the amorphization is reached. It corresponds to a level of ~ 0.45 dpa (or a cumulative deposited nuclear energy loss approximately 29 eV/atom). Table 1.3 summarizes some results on amorphization threshold. As seen the critical dose for amorphization is in the range of 0.2 to 1.32 dpa according to the mass of ion and the implantation energy [28 – 32].

The first two rows which describe the Fe implantation in both 3C-SiC and 6H-SiC do not reveal any differences in the result, so do not show any structure effect (cubic or hexagonal). In case of He implantation, we note the dependence with incident energy [32], the amorphous dose increases with increasing energy. In the latter the resistance to amorphization with increasing energy was found to be concomitant with the resistance to the elastic strain: a higher density of defects is thus required to trigger the crystalline-to-amorphous transition (the strain was determined by using XRD measurements, see chapter 2. It was thus suggested that the amorphization transition is driven by the implantation-induced stresses. For helium implantation, it occurs when a critical strain of about 10 % is reached.

The ion mass may affect defect formation and thus modify the rate of disordering, see figure 1.11 [33]. The dose required to achieve the amorphous transition increases to ~ 0.35 dpa and > 1.1 dpa for the Au^{2+} and He^{+}, respectively. This difference is ascribed to a higher dynamic recovery rate with the ion mass.

Ion	E (keV)	R_p (nm)	SiC type	Tech	$\emptyset_{amorp}$(dpa)	Ref.
Fe^{+}	100		6H- 3C-	RBS	0.45 0.45	[28]
Xe^{26+}	7000		6H-	TEM	0.6	[29]
Kr^{+}	360	139	6H-	RBS	0.83	[30]
Sr^{+}		130			0.71	
Ag^{+}		109			0.52	
I^{+}		97			0.27	
Xe^{+}		102			0.85	
Cr^{+}		106			0.89	
Ar	1000		6H-	TEM	0.42 ± 0.02	[31]
Xe	1500				0.35 ± 0.02	
Au	2000				0.2 ± 0.01	
He^{+}	50	260	4H-	TEM	0.87	[32]
	160	590			1.2	
	1600	3700			1.32	

Table 1.3: Investigation of amorphization threshold with different ion masses implanted at RT and determined by using different techniques (the displacement energies of C and Si were taken as 20 and 35 eV, respectively).

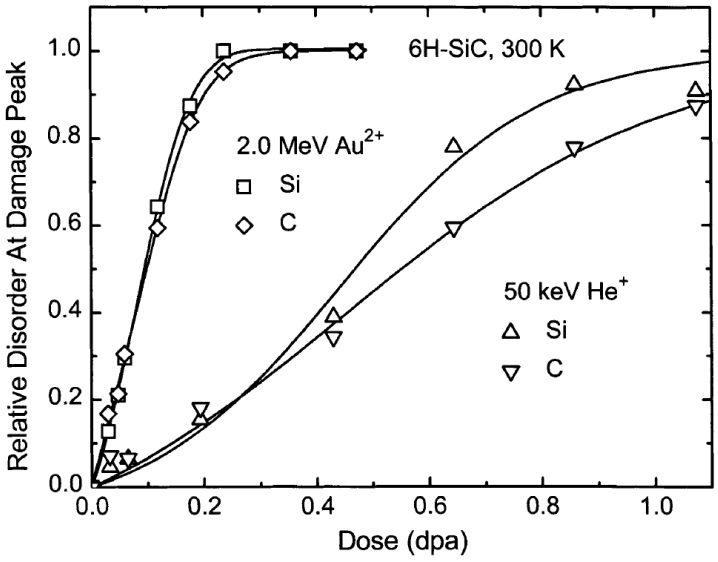


Figure 1.11: A relative disorder of the Si and C sublattice as a function of dose at the damage peak for 2 MeV Au^{2+} and 50 keV He^{+} ions irradiated 6H-SiC at RT [33].

1.3.2 Influence of the temperature of implantation

With increasing temperature, the dynamic recovery increases leading to defect annihilation. Figure 1.12 shows the effect of increasing temperature of silicon implantation on the RBS/C spectra [34]. As seen the RBS spectrum of SiC implanted at 20 °C reaches the level of random spectra. Which means this damaged layer created could be defined as amorphous (0.57 dpa). With increasing implantation temperature the disorder decreases; it can be modeled by an Arrhenius process leading to the activation energy of 0.08 eV. Defect distributions are also found to shift to greater depths with increasing implantation temperature and dose. The shift of the damaged peak was not reported after C^+ implantation at 180K suggesting no significant diffusion of defects at this temperature [35]. Figure 1.13 shows the critical dose to amorphized α-SiC under irradiation of different particles as a function of temperature [36]. As seen the threshold dose for complete amorphization with ions is significantly less than measured under electron irradiation which predominantly produces isolated Frenkel pairs and therefore probably presents a higher recombination-annealing rate.

The noble gases (Ne, Ar, and Xe) were implanted at different temperatures to determine the critical amorphization dose. In the low-temperature regime which is below the room temperature, the amorphization takes place around 0.3 dpa. But with increasing irradiation temperature, the critical limit for amorphization increases due to simultaneous recovery processes. No amorphous transition occurs at the irradiation temperature higher than 500 K. The activation energy for recovery processes is on the order of 0.11 ± 0.02 eV [36]. The increased efficiency of dynamic damage recovery with decreasing particle mass, figure 1.13 is also reported in silicon and called retard to amorphization [37]. The disordering rate at the damage peak was found to exhibit a sigmoidal dependence on ion dose and temperature [35]. In disorder behavior, models have been developed; they are briefly presented in the following section.

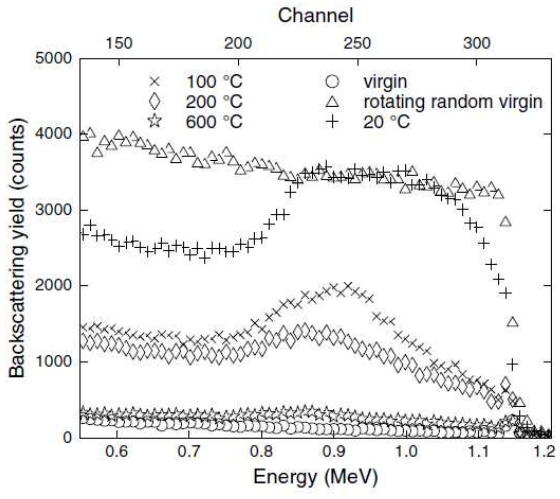


Figure 1.12: Spectra of RBS/C in implanted SiC with 370 keV – 1 x 10^{15} $Si^+ \cdot cm^{-2}$ at temperatures ranging from 20 °C to 600 °C [34].

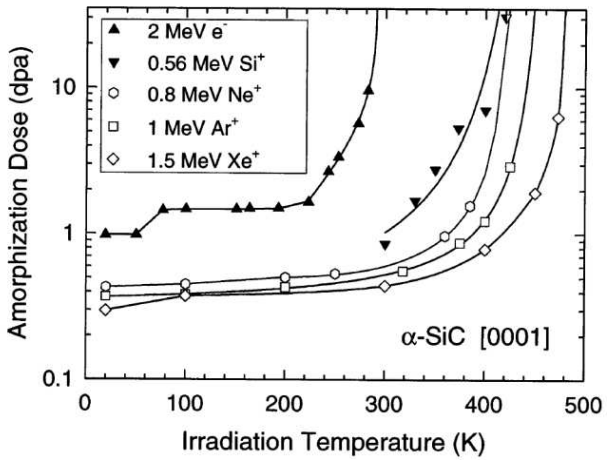


Figure 1.13: Amorphization dose as a function of irradiation temperature with different ions under high energy [36].

1.3.3 Damage models in ceramics

Amorphization results from a dynamic competition between damage production and recovery processes taking place during irradiation. A number of models have been developed to describe the damage accumulation up to the amorphization and the effects of temperature on the kinetics of amorphization; they are reviewed by W.J. Weber [38]. The first and more general phenomenological description of the damage build-up was provided by Gibbons [39], who assumed that the variation of the amount of damage f_a, accumulated during irradiation as a function of the ion fluence ∅ follows the general equation (Eq. 1.1) derived from Poisson's law:

$$f_a = f_a(\infty)\left[1 - \sum_{k}^{n-1} \frac{(\sigma\emptyset)^k}{k!} exp(-\sigma\emptyset)\right] \quad \textbf{(Eq. 1.1)}$$

where $f_a(\infty)$ is the value of f_a measured at saturation i.e. for very large ion fluences (for instance f_a = 1 in the case where irradiation leads to amorphization of the irradiated layer), σ is the disordering effective cross-section, and n is the number of ion impacts required to create permanent damage to the material. Figure 1.14 shows the results predicted by the Gibbons model, they are based on the value of the n parameter.

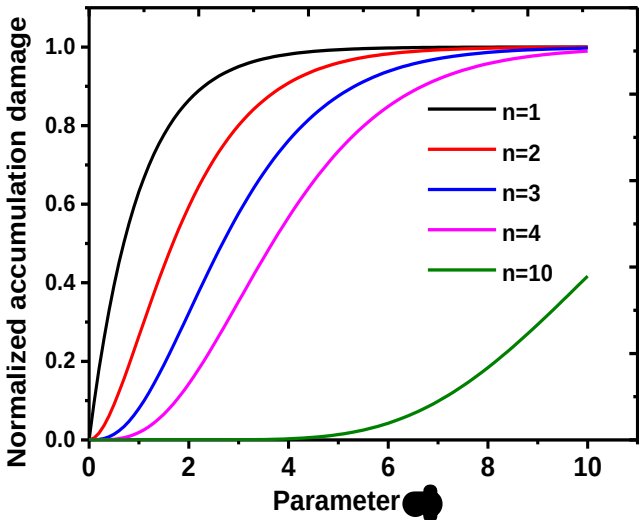


Figure 1.14: Damage accumulation calculated from equation (1).
n = 1 is the Direct-Impact model (DI);
n = 2 is Cascade-overlap model (CO);
n = 10 (n >> 1) represents the defect accumulation (DA) model.

For n = 1 called direct-impact model (DI), each incident ion creates permanent disorder in a given volume of the target and the damage accumulation is given by:

$$f_a = f_a(\infty)[1 - exp(-\sigma\emptyset)] \quad \textbf{(Eq. 1.2)}$$

At low doses, this expression can be approximated by a linear law $f_a \approx \sigma\emptyset$ which means that the disorder is achieved through a single cascade, probably by point-defect accumulation.

In the defect accumulation (DA) process (n >> 1), the damage results from the accumulation of a large number of ion impacts in the same volume of the target. The damage kinetic is thus delayed relative to the DI model.

Other models are used to describe the amorphous transition as the cascade-overlap (CO) model. The double-overlap model (n = 2) generally provides an excellent fit to data for a number of materials exhibiting a sigmoidal dependence of f_a on dose and is given by the following expression:

$$f_a = 1 - [(1 + \sigma_t \emptyset + \sigma_t^2 \emptyset^2/2) exp(-\sigma_t \emptyset)] \quad \textbf{(Eq. 1.3)}$$

where σ_t is the total damage cross-section.

In the Direct-Impact/Defect-Stimulated (DI/DS) model the amorphous transition occurs by both processes: direct impact (DI) and interface stimulated production. The latter results from the implantation-ion-stimulated growth of the amorphous state at the c/a interfaces by the as-induced defects and cascades overlapping and is described by:

$$f_a = 1 - \frac{(\sigma_a + \sigma_s)}{(\sigma_s + \sigma_a \exp[(\sigma_a + \sigma_s)\emptyset])} \quad \textbf{(Eq. 1.4)}$$

where σ_s is an effective cross-section for stimulated amorphization.

Figure 1.15 shows the damage accumulation up to the amorphization for several ceramics of interest [38] that can be compared with the accumulated amorphous fraction as a function of the dose for several mechanisms figure 1.16.

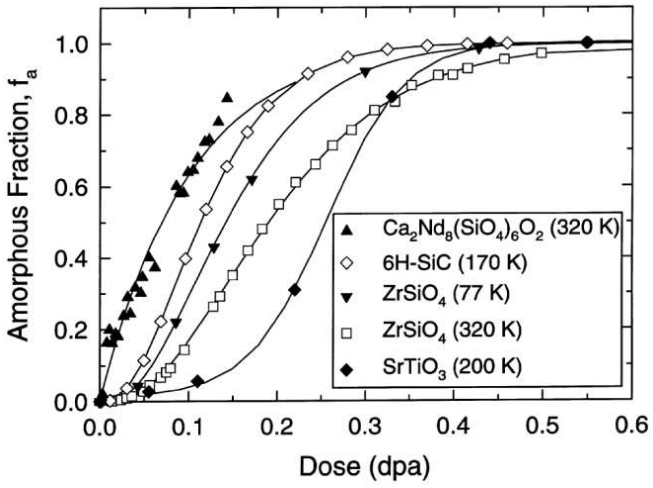


Figure 1.15: Amorphous fraction with increasing dose for common ceramics implanted at low temperature [38].

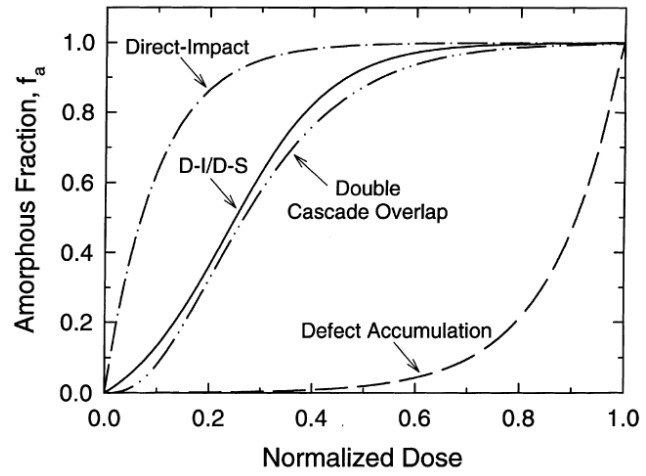


Figure 1.16: Models for amorphous fraction f_a as function of normalized dose including Direct-impact (DI), Direct-impact/defect-stimulated (DI/DS), Double-cascade-overlap (CO) and Defect accumulation (DA) models [38].

Another model has been more recently developed to predict the damage accumulation, involving more than one step [40]. This model called MSDA model for Multi-Step-Damage-Accumulation suggests that the damage build-up results from a series of successive atomic reorganizations which are triggered by microscopic or macroscopic solicitations. Each new step occurs when the current structure of the irradiated material is destabilized by accumulated damage i.e. becomes less energetically favorable than other possible atomic configurations. In this model the damage accumulation is given by the equation:

$$f_D = \sum_{i=1}^{n} \left(f_{d.i}^{sat} - f_{d.i-1}^{sat}\right) G\{1 - exp[-\sigma_i(\emptyset - \emptyset_{i-1})]\} \qquad \textbf{(Eq. 1.5)}$$

where n is the number of steps (1 to 3), but not the same meaning in the first accumulation model developed by Gibbons. In this equation, G is a function which transforms negative value to zero and leaves positive values unchanged, $f_{d.i}^{sat}$ is the level of damage at saturation in the ith step. And $\emptyset_i$ is the threshold fluence for the transformation. Figure 1.17 shows the accumulated damage of irradiated cubic zirconia that is well described by the MSDA model [41]. But no clear explanation exists up to now about the meaning of the fitting parameters.

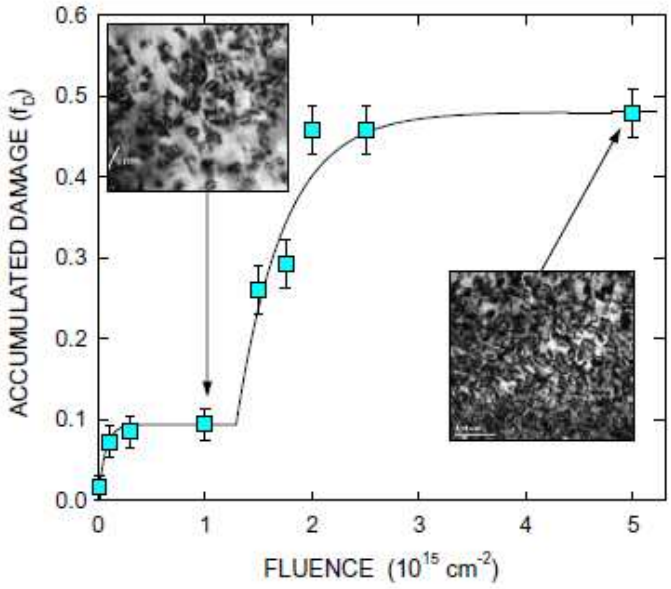


Figure 1.17: Damage accumulation in CZ (Cubic Zirconia) crystals irradiated with 4 MeV Au ions. The solid line fits the RBS data according to Eq. 1.5 (MSDA model with n = 2). TEM micrographs are also included showing the as-resulting microstructure [41].

It is sometimes difficult to discriminate the different models. Figure 1.18 clearly shows that the accumulated damage observed in Fe^+ irradiated 3C-SiC can be relatively well described by the MSDA and DI/DS models. More recently, Debelle et al. [42] suggest that amorphization of SiC is a two-step process. In the first step, only point defect clusters are supposed to produce leading to lattice

swelling. Then in the second step, defects relax towards amorphous domains. Amorphous domains then grow at the expense of defective crystalline region and finally lead to complete amorphization.

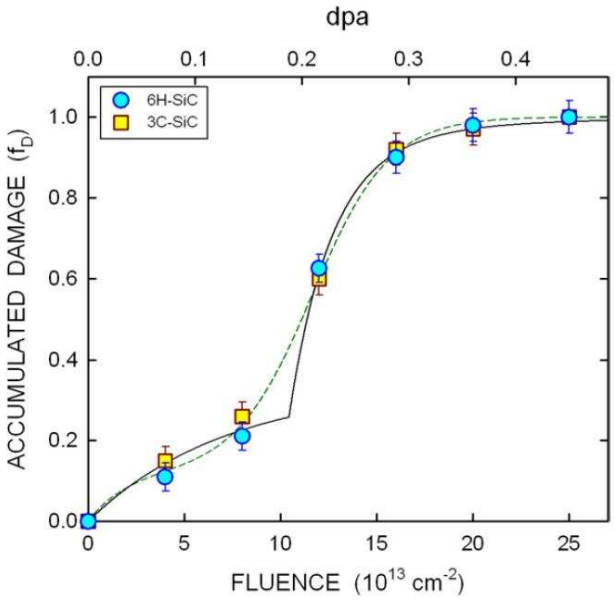


Figure 1.18: Simulation of the disorder accumulation on Fe^{+}-implanted 3C-SiC at RT. Dashed and solid lines are fits to the data with the DI/DS (Eq. 1.4) and MSDA model (Eq. 1.5), respectively [28].

1.3.4 Disorder in SiC with increasing temperature implantation

The disorder accumulation with temperature ranging from 150 to 550 K has been studied in detail by Jiang et al. [43]. Figure 1.19 shows the relative Si disorder of Au-irradiated 6H-SiC (RBS measurements) for three given temperatures of 300, 500 and 550 K.

To fit their RBS data, the authors used a model in which the disorder is the sum of three contributions: the amorphous fraction, f_a described using the DI/DS model (Eq. 1.4), the contribution of irradiation-induced point defects based on simple defect accumulation model and a third term, S_c, due to the contribution of extended defect clusters or precipitates formed at elevated temperature. S_c has a form similar to the point defect production:

$$S_c = S_c^*[1 - \exp(-R\emptyset)](1 - f_a) \qquad \textbf{(Eq. 1.6)}$$

where S_c^* is the saturation value of disorder due to the formation of extended clusters, and R is proportional to effective sink strength to form extended clusters. As seen in figure 1.19, this third term (Eq. 1.6) is not include in the data fitting at 300 K (R = 0) meaning that defect precipitation is not operative. On the contrary, at 550 K, defect precipitation plays a major role in disorder accumulation and stimulated amorphization is no more effective, $f_a = 0$. An intermediate temperature, T = 500 K, the irradiated-induced point defects are predominant in the low dose regime and the amorphous contribution at high dose (> 1dpa). Note also that the C sublattice disorder behavior is similar than Si sublattice.

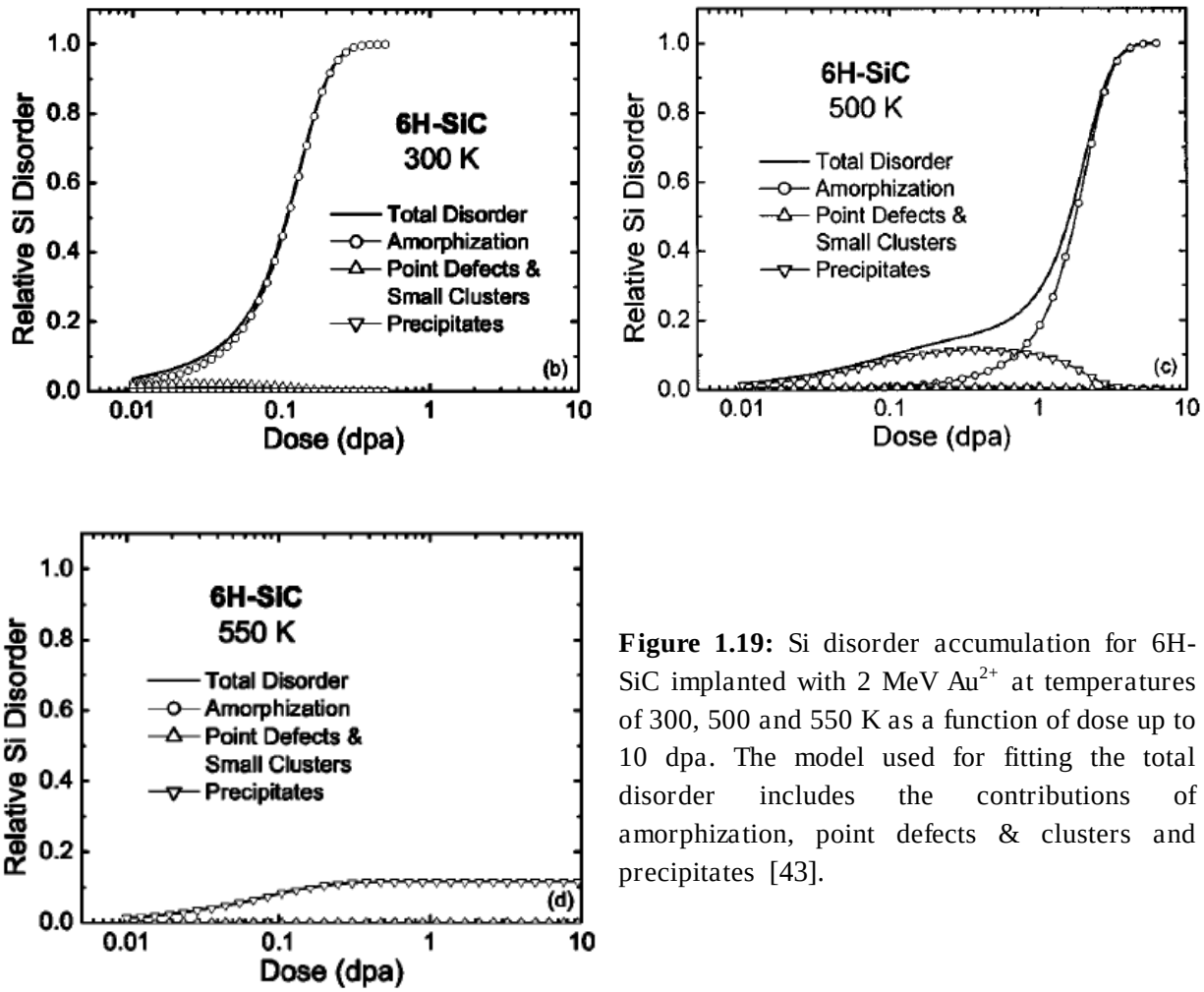


Figure 1.19: Si disorder accumulation for 6H-SiC implanted with 2 MeV Au^{2+} at temperatures of 300, 500 and 550 K as a function of dose up to 10 dpa. The model used for fitting the total disorder includes the contributions of amorphization, point defects & clusters and precipitates [43].

More recently Wallace et al. [44] studied the accumulation of radiation damage in 3C-SiC with Ar ions in the temperature range 25 - 250 °C. They showed that above 150 °C the damage buildup exhibits a two-step shape up to amorphization as seen in figure 1.20. They proposed a phenomenological model based on two contributions: the point defect clustering f_c and the amorphous fraction f_a. The accumulation of amorphous phase takes place above a critical fluence $\emptyset_{crit}$, and is described by the following equation:

$$f_a = h(\emptyset - \emptyset_{crit})(1 - \exp\left[-\frac{\xi_a}{2}\left(\emptyset^2 - \emptyset_{crit}^2\right)\right]) \qquad \textbf{(Eq. 1.7)}$$

where h(x) is the Heaviside function and ξ_a the constant amorphization cross-section reflecting a non-constant effective amorphization cross section σ_a^{eff}. The latter is supposed to dependent on the defect state in the lattice, and is suggested to be linear with dose. It is given by:

$$\sigma_a^{eff} = \xi_a \emptyset h(\emptyset - \emptyset_{crit}) \qquad \textbf{(Eq. 1.8)}$$

The fitting parameters exhibit monotonic dependencies on temperature with activation energies that are not straightforward to understand from a physical point of view.

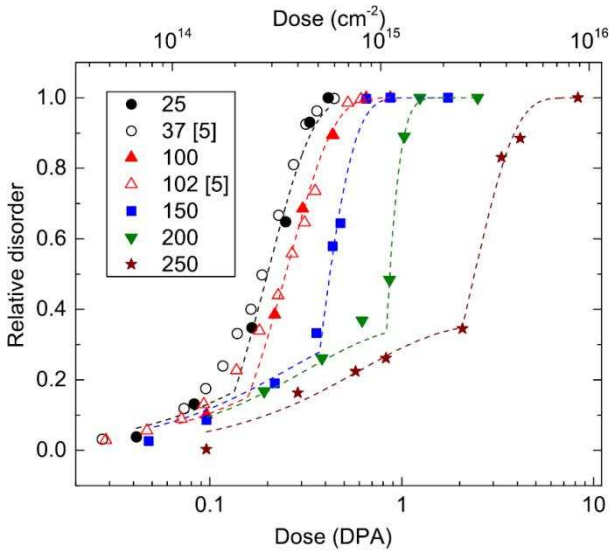


Figure 1.20: Relative disorder on 500 keV Ar^+ implanted 3C-SiC at different temperatures. The dashed lines result from the fitting procedure [44].

1.3.5 Thermal annealing and recovery of defects

Subsequent annealing leads to significant damage recovery. The annealing of amorphous layer shows two stages of recovery. In the low temperature regime (< 700 °C) it is observed that the step height gradually decreases with temperature according to an Arrhenius law with an activation energy close to 200 meV ascribed to short range of defect annealing [45]. This does not change the basic structure of the amorphous network but slightly reduces the amorphous thickness with a near linear rate [46]. Point defect recombination also leads to an increase of the density of the amorphous zone [47]. In the low dpa regime (< 0.04 dpa) for which only point defects appear to be created the defects can be completely recovered by thermal annealing except in the case of inert gases that can induce effects of trapping. The vacancy defects are supposed to be unaffected by the recovery process in this low temperature annealing regime.

1.3.6 He implantation in 4H-SiC

The implantation of helium into 4H-SiC has been the subject of many studies in the PDP team of the Pprime Institute; two thesis were defended in 2001 by E. Oliviero [48] and in 2007 by S. Leclerc [49]. In this section I will present the main results previously obtained by the group that will be useful in this study.

Thermal desorption studies [50] in helium implanted SiC samples showed that helium behavior strongly depends on its association with defects. Two desorption peaks were reported at different temperatures giving rise to dissociation energies of 1.5 and 3.2 eV. It was assumed that the first group would be due to interstitial helium and the second to the de-trapping of helium from vacancy-helium clusters i.e. the helium bubble precursors. In 3C-SiC activation energy for interstitial migration was calculated to be 2.5 eV by using the density functional theory (DFT) [6].

Microstructure evolution under implantation/annealing

One of the consequences of ion implantation is the production of defects that induces the development of an elastic strain in the implanted zone. Leclerc et al. [32, 52] showed that the strain profile is similar to the nuclear energy loss profiles when the helium concentration does not exceed 0.5 % meaning that the strain results from the point defect generation all along the ion path. For fluences exceeding 0.5 % of helium the strain profile is proportional to the helium concentration showing that the He-vacancy complexes have a dominant effect on strain development. Under subsequent annealing the relaxation of strain progressively occurs. suggesting point defect annihilation [51]. Post-mortem TEM observations, see figure 1.21, conducted on the highly perturbed region into $1x10^{16}$ cm^{-2} implanted 4H-SiC (0.2 dpa) shows first the formation of platelets evolving into bubble clusters expelling dislocation loops by a loop punching mechanism.

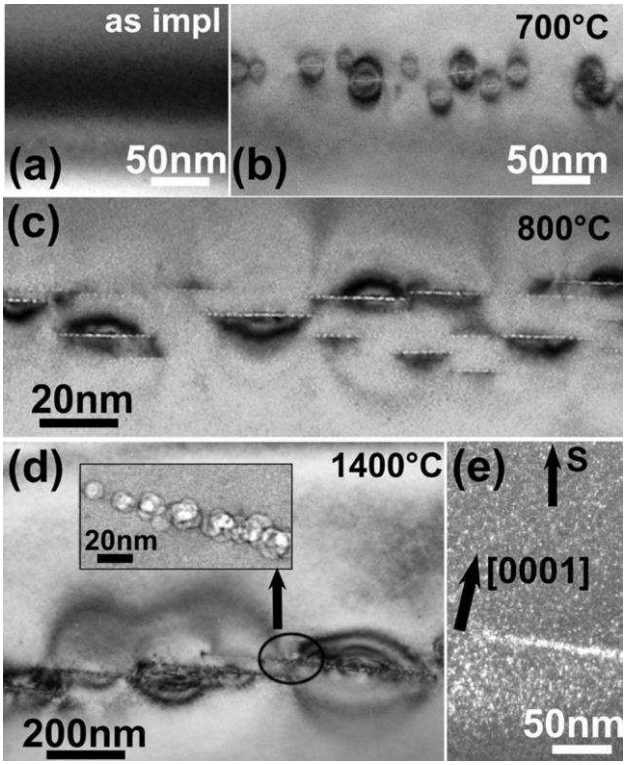


Figure 1.21: Evolution of the microstructure of RT 4H-SiC implanted with 1 x 10^{16} $He.cm^{-2}$ (160 keV) and then annealed at different temperatures [51]. S denotes the surface.

a) as-implanted state
b) 700 °C annealing: formation of platelets
c) 800 °C annealing: 2D clusters of bubbles
d) 1400 °C annealing: large bubble clusters
e) Migration of loops

When implanting helium at a higher dose and elevated temperature bubbles readily form under implantation. For a fluence of 1 x 10^{17} cm^{-2} and for a temperature of 750 °C tiny bubbles form along rows parallel to the surface i.e. in basal planes. Under annealing bubbles coarsening is observed, see figure 1.22. A huge density of stacking faults also appears in the highly damaged zone. HRTEM experiments and atomic structure calculations were conducted to get quantitative insights into the mechanism operating in the stacking fault formation [52].

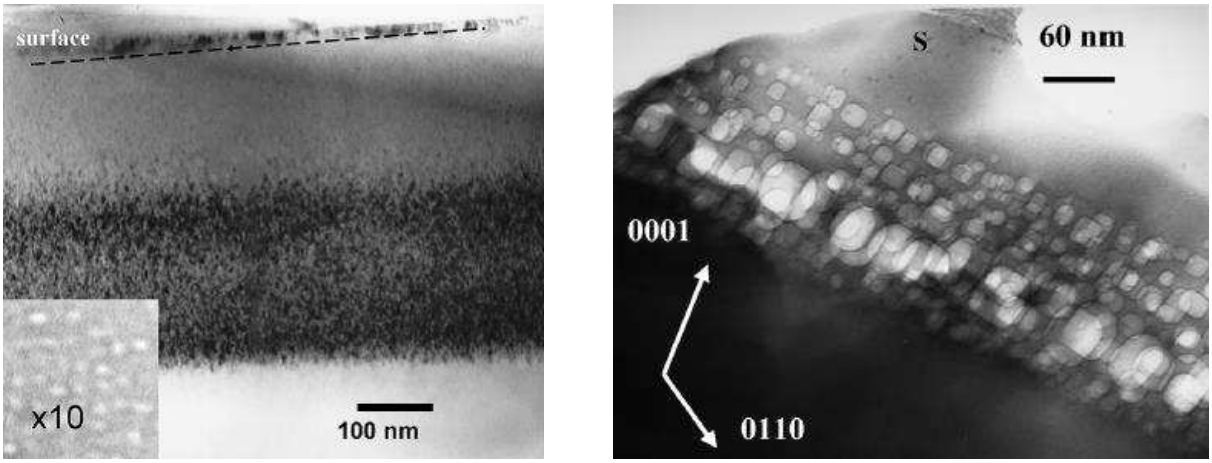


Figure 1.22: XTEM images of 4H-SiC implanted with 50 keV - 10^{17} He.cm^{-2} - 750 °C (left). After a 1400 °C - 30 min annealing (right) [53].

Swelling

Surface swelling is observed in many semiconductors; however the mechanism behind such expansion in not understood properly. In particular in SiC except for C_{Si} antisite, all other defects cause the cell to expand (even vacancy-type defects) [54]. Amorphization itself induces a strong volume expansion or swelling of about 15 - 20 % in SiC according to the literature. Implantation at elevated temperature showed the step height increases linearly with dose [55]; the contribution of the elastic strain, calculated by integrating the normal strain profile, is not sufficient to explain the step height.

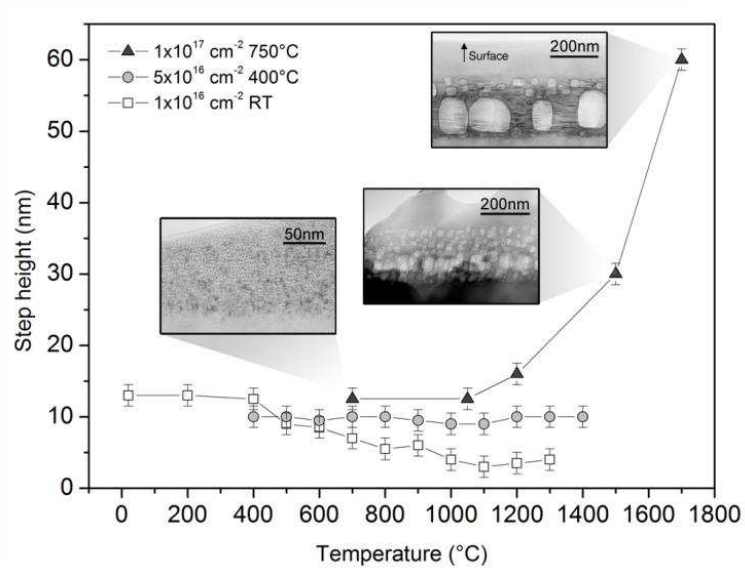


Figure 1.23: Evolution of the step height with annealing temperature in helium-implanted 4H-SiC under different conditions of implantation [56].

Moreover, it has been shown that the evolution of swelling strongly depends on implantation conditions [56]. In particular under severe conditions of implantation figure 1.23 shows that a significant increase of surface swelling is observed to be concomitant with the growth of helium-

related cavities and the formation of other defects, such as the pile-up of stacking faults observed in the highly damaged region.

Changes in mechanical properties

The mechanical properties have been studied by nanoindentation tests available in the laboratory. This study conducted on RT implanted SiC showed an unexpected abrupt increase of the hardness observed at 0.21 dpa, see the arrow in figure 1.24 [57]. To explain this hardness increase complex defects involving helium-vacancy clusters are supposed to act as pinning obstacles for gliding dislocations (the physical mechanism for plastic deformation in SiC). The implantation is also found to suppress the crack formation and to enhance the dislocation generation avoiding thus the pop-in effect (that is an abrupt increase of the penetration depth at a given load) [58].

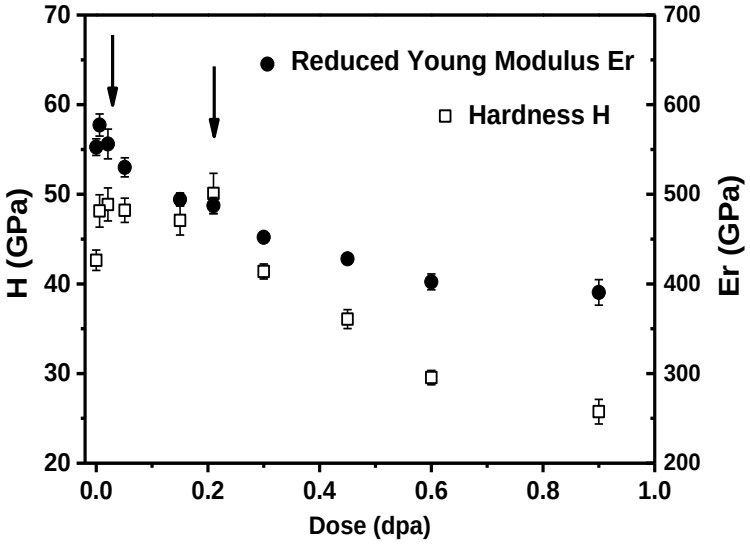


Figure 1.24: Hardness and reduced elastic modulus versus dpa in RT helium implanted in 4H-SiC [57]. Arrows highlight specific hardness increases.

Elastic strain build-up

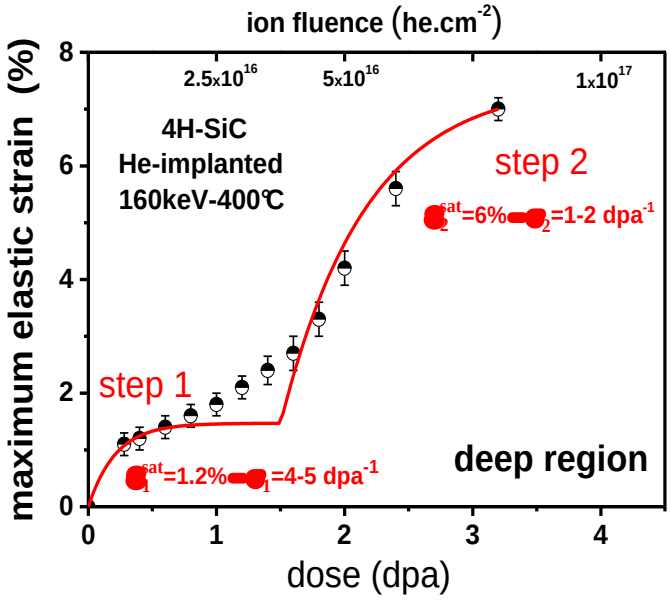
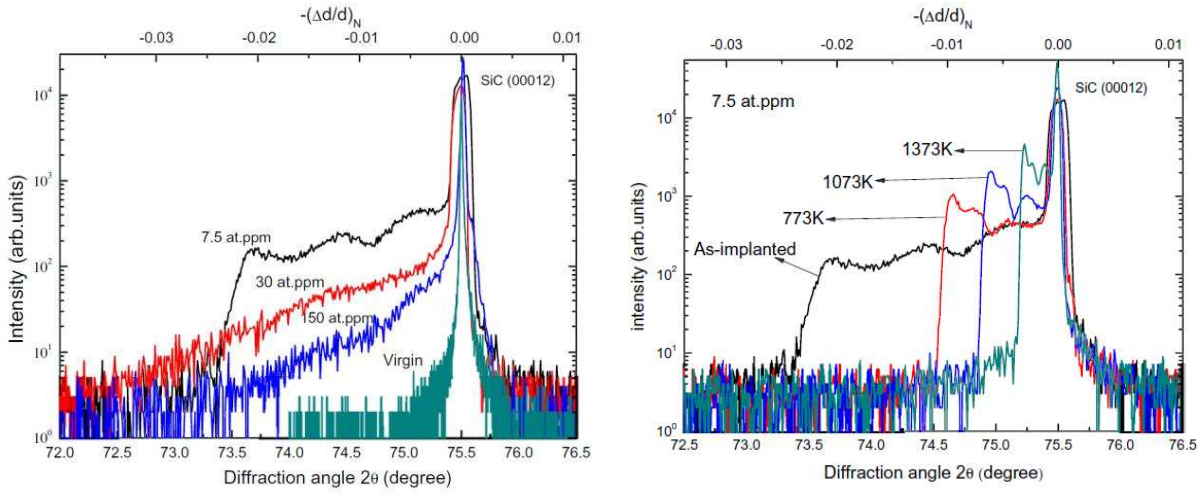


Figure 1.25: Variation of the maximal strain with dose of 400 °C implanted SiC with 160 keV helium ions. The solid line (red) is a fit of data by using the MSDA model (Eq. 1.5) [59].

The defect accumulation in helium-implanted 4H-SiC was studied in a large range of temperatures (RT - 800 °C) through the elastic strain build-up determined by using X-ray diffraction measurements [54, 56]. Figure 1.25 shows the evolution of the maximal strain with dose on 400 °C helium implanted SiC. As seen the strain seems to accumulate in two steps; they were thus fitted by using the MSDA model (m = 2 two steps). But the deviations to the MSDA model in the intermediate range of doses show that this model is not fully adapted to reproduce the strain evolution. Nevertheless, it informs about the nature of the as-created defects since the apparent cross-sections are of the same order in both steps. Figure 1.25 also shows that models must be improved to fully reproduce the elastic strain variation with dose.

1.3.7 Heavy gas implantation in SiC

Very few studies concern the implantation of heavy gases (Kr, Ar, and Xe). As an example of Li et al. [60] studied on the RT Xe implantation in 6H-SiC and its evolution under subsequent annealing. As you can see the XRD spectra, figure 1.26a, the occurrence of a plateau toward the low angle side only in case of low dose implanted, and the absence of coherent diffraction at higher doses due to the amorphization of the implanted region (b). At low concentration 7.5 at.ppm, the strain of the damaged region recovers gradually with increasing annealing temperature (b) due to the migration of interstitials. For specimens implanted at higher concentration, a satellite peak appears at a given position. This peak is supposed to result from the buried strain layer located between the surface amorphous layer and the bulk unperturbed SiC crystal. The similar position of the peak at 30 and 150 at.ppm suggests that a threshold concentration of point defects has been reached under annealing [49].



(a) (b)

Figure 1.26: HRXRD spectra on Xe implanted 6H-SiC at RT with different concentrations (7.5, 30 and 150 at.ppm) compared with virgin SiC specimen (a). Evolution of spectra under subsequent annealing up to 1373 K at 7.5 at.ppm (b) [60].

1.4 Conclusions

In the first chapter, the main properties of SiC have been presented such as structure, properties and applications. Thanks for the SiC properties; it can be considered as a semiconductor or as a ceramic, it is thus a multi-proposed material. For example, large bandgap is an important characteristic in electronic field and SiC-based Schottky diodes, JFET and MOSFET are available in the electronic market. The high temperature of melting point, the stability, the neutron transparency and the slow oxidation, all these advantages permit SiC can be used to work in nuclear applications.

Numerous previous studies have been carried out to understand the effect of implantation in SiC in order to improve its use. In particular, the damage accumulation up to the amorphization has been the subject of many works. The amorphous transition can be quantitatively described by different models, but all the models have been developed according to data based on ion channeling techniques. Few works have also been done on the SiC-behavior under implantation conducted at elevated temperatures for which amorphization are avoided. Few works also reported the behavior of heavy ions. During my Ph.D. I focused my studies on the behavior of Xe-induced damage introduced under different experimental conditions. In particular, the elastic strain evolution under implantation and then annealing was the guideline in conducting our study. No existing models were designated to reproduce the evolution on strain (based on XRD experiments: the out-of-plane strain).

The second part of this thesis will present experimental methods with their principles and the application procedures. The third is dedicated to results and discussions.

Chapter 2
Experimental methods

In this chapter, we briefly describe the main methods (XRD, TEM, interferometry) used in this work. Furthermore, some experiments are presented to validate the choices we made in the experimental conditions, in particular, those relative to the annealing conditions.

2.1 Ion implantation

Ion implantation is a technology which consists to introduce chemical species in a material like semiconductors (Si, SiC). The principle is the following: atoms or molecules are ionized in an ion source and then accelerated through an electrostatic field to energy between a few thousand electron volts (keV) and several million electron volts (MeV). Then, an analyzing magnet allows separating the ions by mass. Finally, the chosen ions pass through a quadrupole magnet to concentrate them into a beam toward the material (target). This process is widely used in physic, chemistry and high technology industries. In the electronic field, the ion implantation is used to dope the material to produce the electronic devices and chips. This technique is also used in nuclear research to simulate the irradiation damage.

The advantage of this technique is that implantation is very precise in controlling dose and depth profile by varying the conditions such as energy, fluence with an excellent lateral uniformity. It also allows realizing a more complex profile by using multi-energy implantations.

2.1.1 Interaction process

Stopping power

When a solid material is bombarded with an ion beam, a number of mechanisms operate to slow the ion and dissipate its energy. These mechanisms can be subdivided into two general categories: electronic and nuclear energy losses. Nuclear energy transfer results of elastic collisions whereas electronic energy losses occur as a result of inelastic scattering events. The rate of energy losses per unit path length, $\frac{dE}{dx}$, can be explain by following formula:

Energy loss rate
(N is the target atom density)

$$\frac{dE}{dx} = -N\left[S_n(E) + S_e(E)\right] \qquad \textbf{(Eq. 2.1)}$$

or

$$\frac{dE}{dx} = \left(\frac{dE}{dx}\right)_e + \left(\frac{dE}{dx}\right)_n \qquad \textbf{(Eq. 2.2)}$$

The dependences of electronic and nuclear contributions to the stopping cross section as a function of the ion velocity are plotted in figure 2.1. At low energies, the nuclear stopping dominates while at high energy it decreases and electronic stopping dominates, then reaches a maximum and decreases at the very high energy region or Bethe-Bloch region. This is caused by the shorter amount

of time which the ion has to interact with the electrons of the target atom owing to its high velocity electronic.

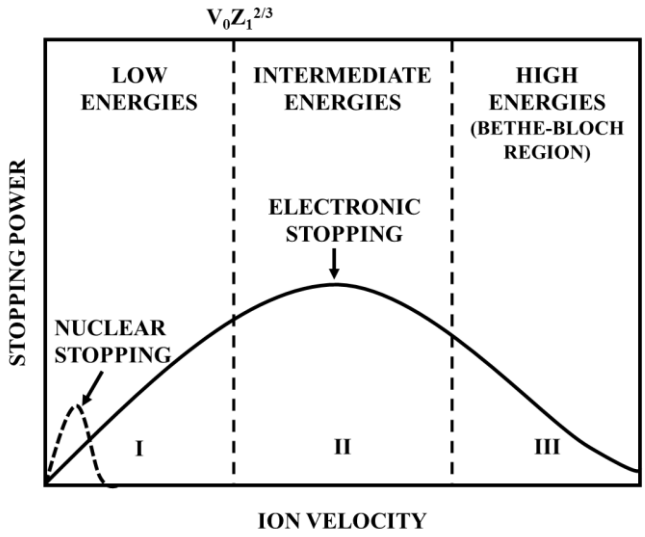


Figure 2.1: Nuclear and electronic stopping powers $S_n(E)$ and $S_e(E)$ as a function of ion velocity. The quantity v_o is the Bohr velocity and Z_1 is the ion atomic number.

The nuclear stopping power represents the defect distribution which is often characterized by the depth of the defect concentration R_D which corresponds to the maximum of the nuclear stopping power.

Range of ion and damage distribution

Ion implantation is a random process due to each ion follows its own random trajectory, scattering off the lattice silicon atom. Since implantation fluences are high, ion trajectories are predicted by employing statistical means. The average length path (composed of both lateral and vertical motions) is called the range R and is given by:

$$R = \int_0^R dx = \frac{1}{N}\int_0^{E_0} \frac{dE}{S_n(E) + S_e(E)} \qquad \textbf{(Eq. 2.3)}$$

The projected range, R_p, describes the peak of the implanted profile, it is thus the average distance traveled normally to the surface. The straggling ΔR_p represents the ion path in statistically scattered which is described as the square root of the variance. The distribution of the implanted ions versus depth, n(x), can be approximated as Gaussian with a standard deviation ΔR_p:

$$n(x) = \frac{\emptyset}{\sqrt{2\pi}\Delta R_p} exp\left[-\frac{(x - R_p)^2}{2\Delta R_p^2}\right] \qquad \textbf{(Eq. 2.4)}$$

where $\emptyset$ is the total number of ion fluence (the number of ions implanted per unit area). The area under the distribution is the implanted fluence, given by the equation:

$$\int_0^{+\infty} n(x)\, dx = \emptyset \qquad \textbf{(Eq. 2.5)}$$

In general, distributions are characterized in terms of their moments. The normalized first moment of an ion distribution is the projected range, R_p. The second moment is the standard deviation, ΔR_p. The third moment is the skewness (γ) and the fourth moment the kurtosis (β). Qualitatively, skewness is a measure of the asymmetry of the distribution; $\gamma > 0$ indicates that the peak is right-skewed, $\gamma < 0$ indicates that the peak is far from the surface (the distribution is left-skewed or left-tailed). Kurtosis is an indication of how flat the top of a distribution is; $\beta > 3$ indicates broad tails. A true Gaussian distribution has a skewness of 0 and a kurtosis of 3**.**

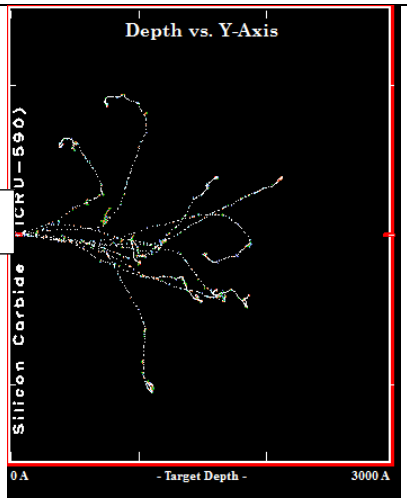
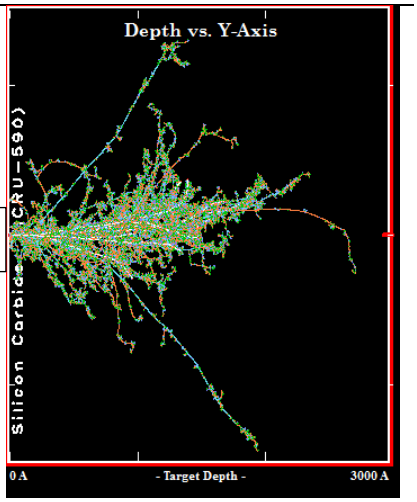
2.1.2 SRIM simulation

The SRIM (the Stopping and Range of Ion in Matter) program, developed J. F. Ziegler and J. P. Biersack [61] is simulation software which calculates the interaction of ions in matter by using a Monte-Carlo code (ion trajectories, phonon production, sputtering, ionization and target damage …). Each interaction which corresponds to a section efficiency of interaction is dependent on following parameters: the **nature of the incident particle** and its energy and **the nature of the target particle** ($E_c = 0$ in case of an atom of crystal). SRIM profiles are independent of fluence as the simulation does not include dynamic effects caused by the implanted ions. The implanted ion concentration is then plotted in normalized units and simply scales linearly with fluence.

Figure 2.2 compares 10 ion paths from SRIM Monte Carlo calculations for 22 keV He ions and 540 keV Xe ions in SiC, and the ion recoils generated by the nuclear collisions (full cascade damage). As expected the deposited energy density is larger for heavy ions and sub-cascades appear. The implantation damage is thus a function of mass ratio ion/target atom, energy, fluence, fluence rate, temperature). Moments of the distributions (mean depth, straggling, and so on) have been calculated by using more incident ions to improve statistics. Incident energies have been chosen to obtain a similar mean projected range, $R_p \sim 140$ nm.

In this work all the SRIM calculations have been done using displacement energies of 20 and 35 eV for the C and Si sublattice, respectively [62]**.**

Figure 2.2 also highlights mass effects: for instance, the number of target vacancies per incident ion is 70 times larger for Xe than for He implantation. The distribution of ion implanted Xe is narrower and is Gaussian-shaped ($\gamma \sim 0$ and $K \sim 3$) in contrary to the He-profile which shows a noticeable skew toward the surface ($\gamma < 0$ and $K \sim 3$). Figure 2.3 shows the resulting normalized ion distribution and the energy deposited by nuclear collision as a function of depth. The ion mass effects are also visible in the vacancy profile which shows in Xe-implanted SiC a more pronounced shoulder toward the implanted surface. Therefore, the near-surface region is expected to be more damaged for Xe implantation.

Target layer	SiC	**Density:** 3.21 g/cm^3
Simulation (10 ions) Full cascades	**He** 	**Xe** 

Report: simulation of 10000 ions

Ion Energy	22 keV	540 keV
Total Target vacancies	64 / Ion	4425 / Ion
Total Target displacements	71 / Ion	4686 / Ion
Replacement Collisions	7 / Ion	262 / Ion
Straggling	410.4 A	333.5 A
Skewness γ	-0.5358	0.0376
Kurtosis K	3.2108	2.8007
Ion range R_p	138.9 nm	143.9 nm

Figure 2.2: SRIM simulations for 10 incident ions showing the helium and xenon ion tracks in SiC. Data obtained with 10000 ions are also reported.

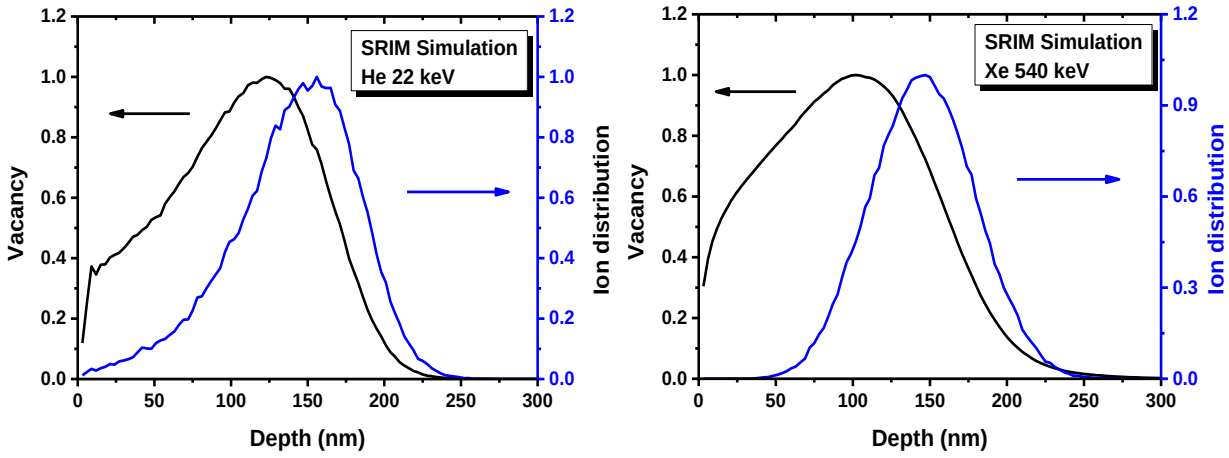


Figure 2.3: SRIM simulation for He implantation - 22 keV (left), for Xe implantation - 540 keV (right).

The displacement per atom (dpa) is the number of times that an atom is displaced for a given fluence. This is a useful parameter to compare radiation damage by different sources of radiation. Irradiation-induced changes of material properties are thus specified as a function of dpa given by:

$$dpa\left({}^{vac}/_{atoms}\right) = \frac{total\ fluence\left({}^{ions}/_{cm^2}\right) \times vacancy\ \left(\frac{vacancies}{ion \cdot \text{Å}}\right) \cdot 10^8}{atomic\ density\ \left({}^{atoms}/_{cm^3}\right)} \qquad \textbf{(Eq. 2.6)}$$

The ion concentration versus depth is determined according to the implanted fluence by the following formula:

$$Concentration\ (\%) = \frac{fluence\left({}^{ions}/_{cm^2}\right) \times ion\ distribution\ ({}^{ions}/_{cm})}{atomic\ density\left({}^{atoms}/_{cm^3}\right)} \times 100\ \% \qquad \textbf{(Eq. 2.7)}$$

160 keV - He - implanted: The group of research in which I did my Ph.D. has previously done a great deal of work on helium implantation in SiC, in particular by using different energies in the range from keV to MeV. As an example, 160 keV He-ion implantation gives rise to a mean projected range of 550 nm approximately and a more pronounced skewness ($\gamma \sim -1.6$). In the following chapter results concerning 540 keV-Xe-implanted will be compared with 160 keV-He-implantation for which a detailed study has been done.

2.1.3 Implantation experimental details

Implanter EATON

To study the damage created by ion implantation in 4H-SiC, we use the implanter EATON™ NV3206, see figure 2.4, which is available in our laboratory. The maximal operating voltage is 180 kV. Therefore, the ions would be multi-charged to be accelerating up to 540 keV in case of Xe^{3+} implantation. The implantation temperature is ranging from -200 °C up to 800 ºC. Many atoms are available to implant such as H, He, C, N, O, Ne, P, Ar, Kr, and Xe. During implantation, the pressure in the implantation chamber remains below 10^{-5} Torr.

The implantation duration t_{imp} is calculated by the following formula:

$$t_{imp} = \frac{S \times \emptyset \times q}{I} \qquad \textbf{(Eq. 2.8)}$$

where S represents the implanted surface, $\emptyset$ the fluence, I the ion beam current and q the electron charge.

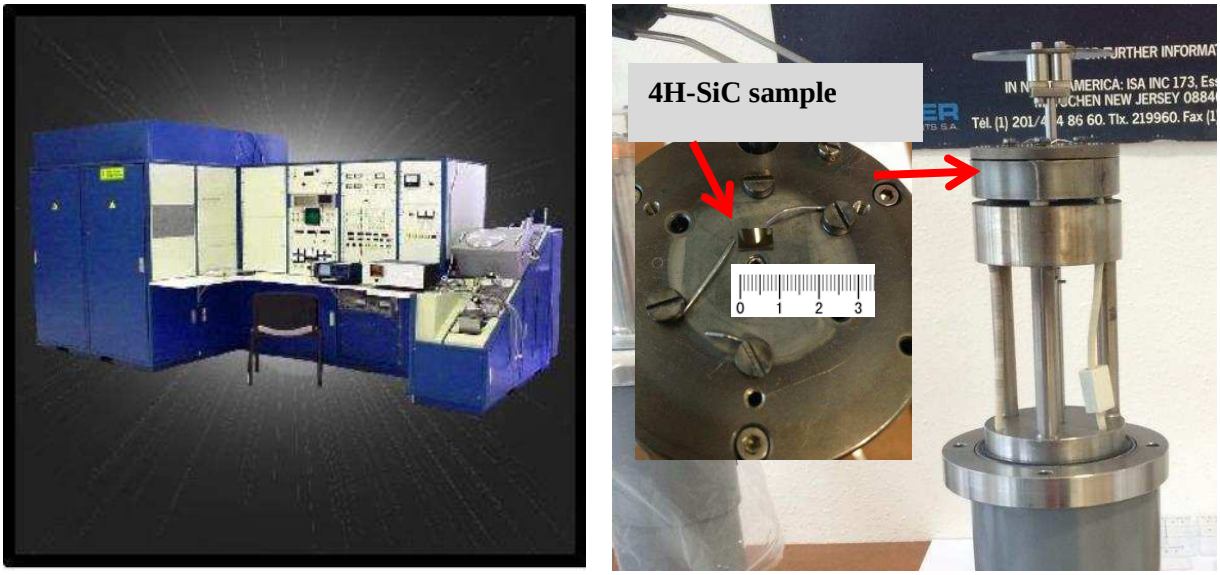


Figure 2.4: Implanter EATON NV3206 and sample holder.

Experimental details

The 410 µm thick $(0001)_{Si}$ 4H-SiC wafers used in our study were n-type with a resistivity of 0.018 Ω.cm and were supplied from Cree research. The surface normal direction [0001] is 8° tilt toward the direction of $[11\bar{2}0]$ avoiding any channeling effects during the implantation. The implantations were performed at different energies from 110 to 540 keV according to the ion mass in order to create a damage/ion profile at a given depth according to SRIM simulations ($R_p \sim 150$ nm). The conditions of implantation are summarized in table 2.1. To avoid any additional heating effects, the Xe-implantations conducted at low temperatures (< 200 °C) were carried out with a mean current density close to 0.4 µA.cm^{-2}. At elevated temperature, the mean current density was fixed at higher values especially for the high fluence implanted samples to reduce the duration of implantation.

Atom implanted	Implantation energy	Used ions	Implantation voltage	Temperature
Ar	210 keV	Ar^{2+}	105 kV	400 ºC
Ne	110 keV	Ne^{+}	110 kV	400 ºC
Xe	540 keV	Xe^{3+}	180 kV	RT 200 ºC 250 ºC 300 ºC 400 ºC 600 ºC 800 ºC

Table 2.1: Implantation conditions used in this study. Energies of implantation were chosen to fix the mean projected range close to 150 nm (SRIM calculations).

Furthermore, in the study of surface swelling induced by the ion implantation, a small part of the sample was covered by a silicon mask during the implantation process, see figure 2.5. The step height was then measured by using a scanning broadband interferometry (Talysurf CCI 600, &2.3).

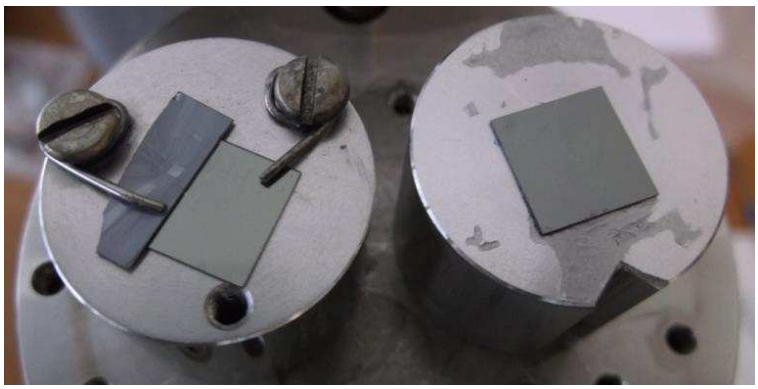


Figure 2.5: Sample holders to fix the 4H-SiC sample in the implantation chamber. As seen a piece of silicon is put on a part of the sample (left) to act as a mask during the implantation (determination of the surface swelling).

2.2 X-ray Diffraction (XRD)

2.2.1 X-ray Diffraction technique

When sending a monochromatic beam of X-rays on a crystal, each atom which becomes a diffusing center returns a wave might interfere with other waves from the other atoms. The diffracted wave in a given direction is the resultant of the waves emitted by all the atoms of the crystal. If these waves are in phase, it means the optical path difference between these waves is equal to an integer number of the wavelength of the incident beam, and their amplitudes are added resulting in non-zero intensity. But if there is a phase difference between the scattered waves, then these elementary waves cancel by interference.

Consider a family of the atomic plane (h, k, l) of parallel and equidistant of the d_{hkl}. All atoms of the same plane diffuse in phase, the distances traveled by two rays passing through both of the atoms being identical.

Interferences are constructive when the waves scattered by the atoms of two consecutive planes have the same phase. This condition can be written, according to the figure 2.6 and the wavelength lambda of the incident beam.

Thus, an incident ray of length λ at θ angle with a set of lattice planes (h, k, l) gives rise to a diffracted beam in the direction of the reflected beam with a non-zero intensity if the condition of Bragg's law is fulfilled. Furthermore, for a given family of plane (h, k, l), there are as many diffraction angle as there are integers n such that: $n \lambda < 2 d_{hkl}$ .The number n is the order of reflection, a reflection

of order n on a family of planes (h, k, l) can be considered as a reflection of the first order on a family of planes (nh, nk, nl) equidistant of d / n. The Bragg condition is then written $2d_{hkl}\sin\theta = n\lambda$. Thus with a constant wavelength is possible to measure inter-planar spacing by measurements of the diffraction angles 2θ.

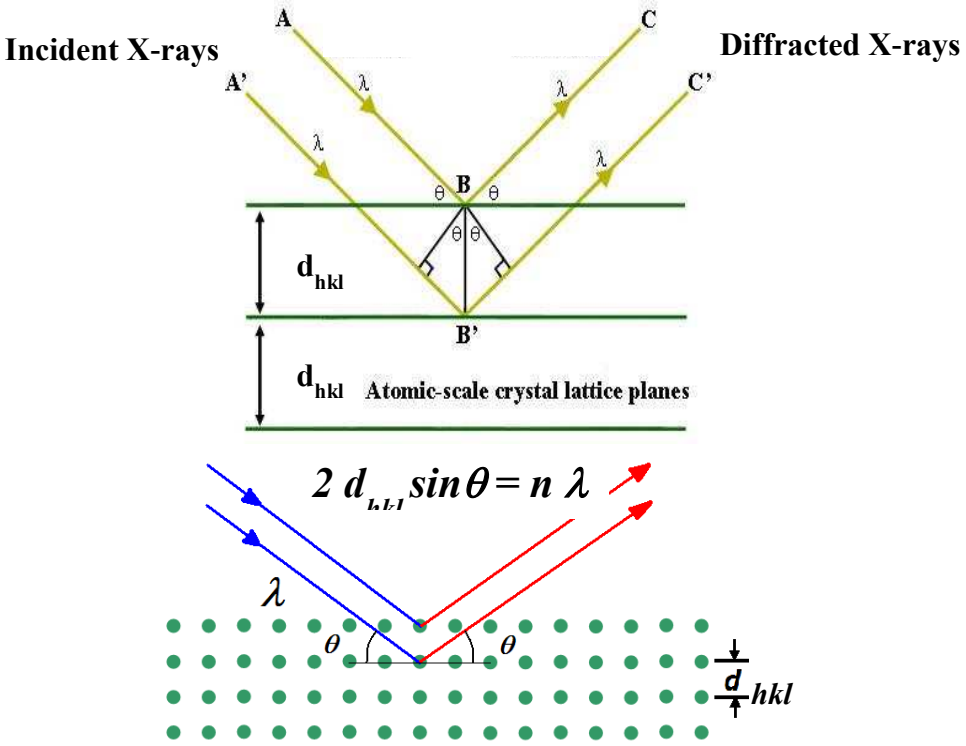


Figure 2.6: Reflection of X-rays by a family of lattice planes spaced by a distance d [63].

X-ray techniques and especially X-ray diffraction are widely used to obtain information in crystalline materials namely the crystal structure, the crystallographic phases, and the stress distribution.

2.2.2 X-ray diffraction curves

Let us now consider a damaged crystal. The structural modifications induced by implantation involve variations in the spacing of the lattice planes, i.e., strain, and displacements of the atoms from their sites, i. e., disorder, in the upper implanted layer. The strain produces an angular shift of diffracted intensity from that of unperturbed crystal and is easily quantified from XRD measurements. $\omega - 2\theta$ scans performed along the direction normal to the surface allow to determine values of this normal strain $\varepsilon_\perp$ or $\Delta d/d$ [49]**.** The relation connecting the normal strain to the Bragg angle θ_{Bragg} is obtained from the derivation of the Bragg's law:

$$-\frac{\Delta d}{d} = -\frac{d - d_{hkl}}{d_{hkl}} = \frac{\theta - \theta_{Bragg}}{\tan\theta_{Bragg}} \qquad \textbf{(Eq. 2.9)}$$

Where d is the interplanar distance of lattice planes (h, k, l) in the implanted layer and d_{hkl} is the interplanar distance of lattice planes (h, k, l) in the un-implanted sample. In such XRD

measurements, the scattering vector $\vec{K}$ is such as $\vec{K} = \vec{H} + \vec{q}$, where $\vec{H}$ is the diffraction vector of the (h k l) reflection corresponding to the studied Bragg peak, and $\vec{q}$ is the deviation vector which coincides with the scan from the Bragg peak in the direction normal to the sample surface. Then, $q/H \approx -\Delta d/d$.

Figure 2.7 gives the intensity distribution measured along the surface normal direction around the symmetric Bragg reflection (0004) of a Xe-implanted 4H-SiC sample (400 °C – 540 keV -5 x 10^{13} cm^{-2}). The XRD pattern of a virgin sample is given as a reference. The pristine specimen exhibits a symmetrical peak around the Bragg angle. The same peak is observed at q/H ~ 0 on the implanted sample. In our experimental conditions (λ = 1.54 Å; θ_{Bragg} = 17.8°), the XRD penetration depth is > 10 µm larger than the thickness of the implantation-induced damaged region (R_p < 1 µm). Thus, this peak corresponds to the unperturbed bulk of the implanted sample. The scattered intensity for θ < θ_{Bragg} (i.e.$-\Delta d/d < 0$) observed on the implanted sample is the result of the dilatation of the crystal lattice along the normal to the surface in the upper implanted layer. Conversely, a compression of the crystal lattice would result in a scattered intensity at higher angles (i.e. $\theta > \theta_{Bragg}$).

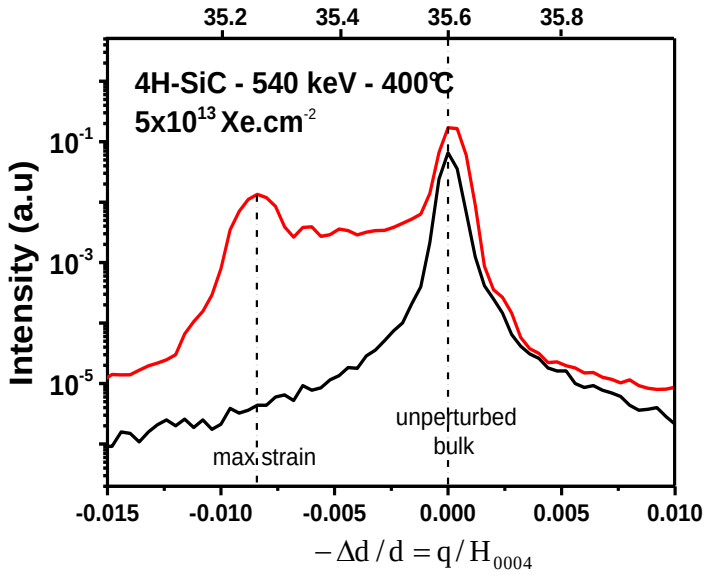


Figure 2.7: X-ray scattered intensity distribution along the normal surface direction close to the symmetric (0004) reflections in xenon implanted 4H-SiC (at 400 °C, 540 keV 5 x 10^{13} $Xe.cm^{-2}$)

The scattered intensity of the implanted sample also displays interference fringes which are characteristic of a Gaussian tensile strain gradient due to the ion implantation [49]. They result from the coherent diffraction of X-rays between two damaged zones with the same level of strain from part to part of the maximum of the Gaussian tensile strain gradient. The width of these fringes is inversely proportional to the distance between the two damaged zones. The width between two zones of same low strain is consequently higher than in the region of maximum strain. The maximum strain is given by the position of the last fringe.

In a previous study conducted in helium-implanted SiC it was shown that single or cumulative implantations to reach a given fluence are equivalent to the as-induced elastic strain [49]. And this behavior is also verified in Xe-implanted SiC sample (our study), see figure 2.8.

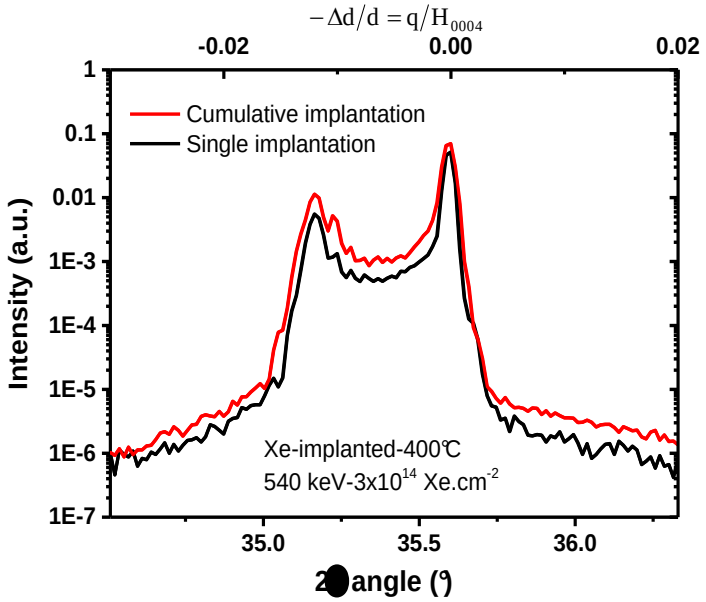


Figure 2.8: Comparison of X-ray scattered intensity for single and cumulative Xe-implanted 4H-SiC (at 400 °C, 540 keV 3 x 10^{14} Xe.cm^{-2}).

2.2.3 X-ray diffraction simulation

The profile of strain can be obtained by simulating experimental curves with the GID_sl web-based program written by S. Stepanov [64]. The program implements a discrete algorithm; the crystal is divided into sublayers having different parameter as the Debye-Waller factor (DW) and the normal strain. The XRD simulation has been successfully applied for helium implantation [49]. However, there is no way to know from XRD data the absolute position along the depth of each section of the deformation profile: X rays are insensitive to the symmetry of the strain profile [65]. As a starting point for the simulations, the normal strain has been taken to be proportional to the nuclear energy profile. In case of helium implantation, it has been shown that there is a strong correlation between the strain profile, determined using the large angle convergent beam electron diffraction, and the nuclear stopping curve given by SRIM simulation [66].

In the case of helium implantation, it was found that at a low fluence of RT-implantation (C_{He} < 0.5 %) the strain profile follows the nuclear energy loss profile [51]. On the other hand in RT - N^+-implanted SiC the normal strain profile appears lower than the nuclear energy profile in the near surface region and then follows the nitrogen concentration. Figure 2.9 shows an example of strain profile as calculated [67]. These differences show that different mechanisms are operative according to the incident ions.

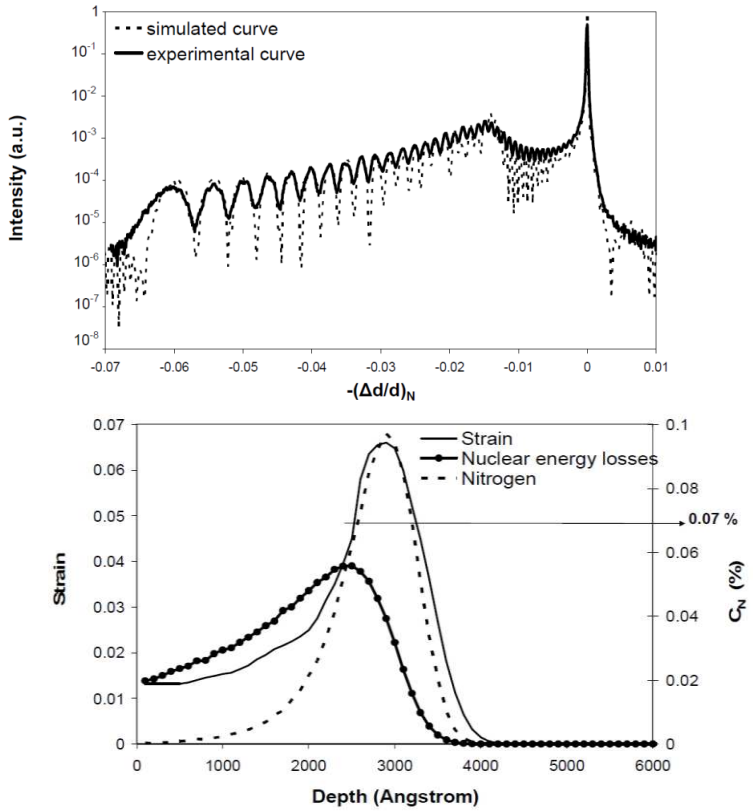
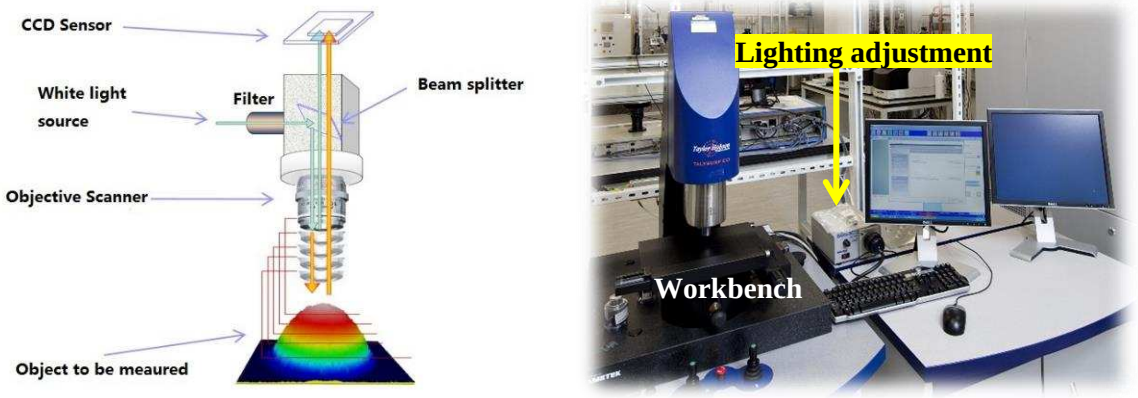


Figure 2.9: Simulated XRD curve obtained in RT - N^+-implanted SiC with 1 x 10^{15} cm^{-2}(top). Normal strain profile compared with the normalized nuclear energy loss and N concentration (bottom).

2.3 Surface measurement

2.3.1. Technical description of scanning broadband interferometry

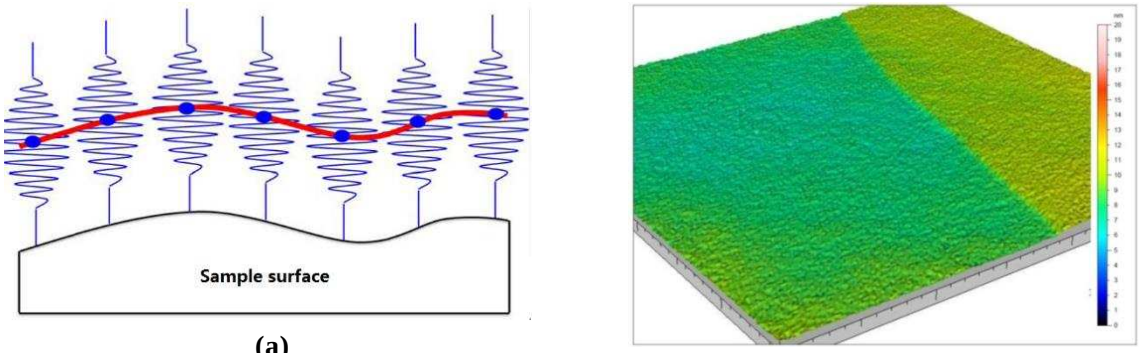
An interferometer is a non-contact surface profiler system that can be used for surface height measurements. It is an optical device dividing a beam of light into two separated beams: one onto a reference surface and the other onto the sample's surface; forming then an interference pattern. A CCD array is used to take the image and collect the information, see figure 2.10a. The apparatus used in this study was a Talysurf CCI600 driven by a computer (windows, see the picture in figure 2.10b).



(a) **(b)**

Figure 2.10: Interferometer schematic (a). The interferometry Talysurf CCI used in this study (b).

Three resolution modes are available depending on the different usages. The XY resolution mode gives the greatest lateral detail with 1024 x 1024 pixels. The XYZ mode applies 2x binning which is averaged the results in 3D. And the most suitable to our case is the Z mode which applies 4x binning to give the best result in the step height measurements. A 3D map of the surface can thus be formed by tracking the position of the interferometer, see figure 2.11.

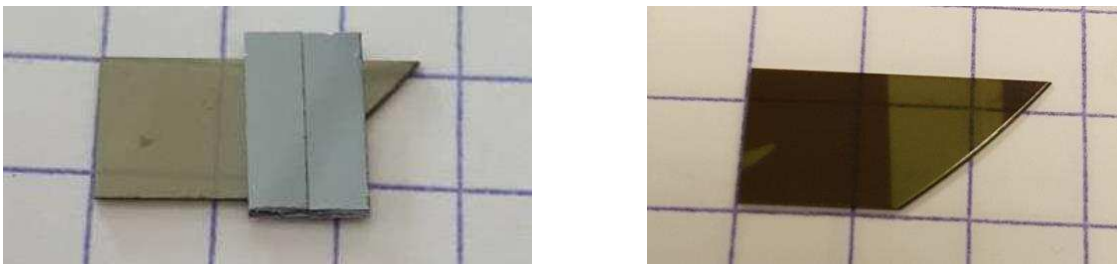


(a) **(b)**

Figure 2.11: Schema of interference wave to realize the surface data (a). 3D map of the masked surface after Xe-implantation (b).

2.3.2. Procedures for operating the scanning broadband interferometry

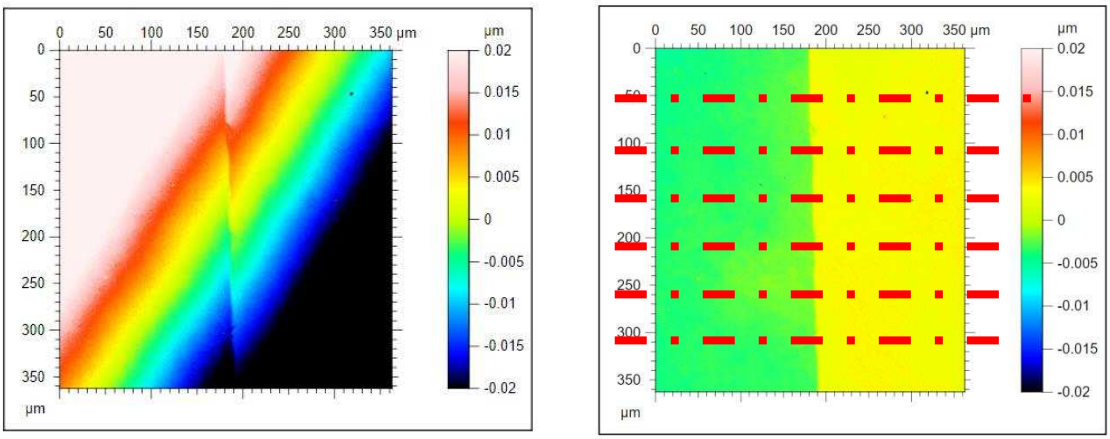
During the implantation part of the 4H-SiC samples was masked by a piece of silicon, figure 2.12. After implantation, the implanted part (non-masked) is of dark color showing that the as-created defects modify the band structure of the implanted part (introduction of deep levels in the band gap of the SiC, 4H- or 6H-). The scanning broadband interferometry measures the step height (surface swelling) between the two zones. A procedure in sample preparation should be respected before any measurement. The specimen should be clean and free of grease, fingerprints, and dust.



(a) (b)

Figure 2.12: 4H-SiC sample with a piece of silicon playing the role of the mask (a). After Xe implantation at 400 °C - 540 keV- 6 dpa showing the change in the color of the specimen (b).

The first operation is to observe the fringe pattern by using the objective lens x50. Then, the interferometer scans the objective surface and exports an image. But it is sometimes difficult to adjust at a relative level, a distortion image is frequently obtained, see figure 2.13. So a re-leveling option is required and available in the analysis software to get a perfect leveling surface. The re-leveling and optimization of the originally measured surface are then convenient to measurement.



(a) **(b)**

Figure 2.13: Before (a) and after (b) re-leveling optimization. 6 lines will be used to measure the step height. The surface image was obtained after scanning in 350 µm x 350 µm with a height scale according to the color.

2.3.3. Step height estimation

The surface is presented in 2-D horizontal and vertical, the color bar represents the height of the surface, see figure 2.14. The left green part is lower it is the virgin surface, and the right yellow part is higher: the implanted zone. A line anywhere on the surface is used to determine the variations of heights. To get more reliable experimental data, we plotted 6 straight paralleled lines on the sample, in order to calculate the standard deviation. The step height, h_s, is thus:

$$h_s = h_m \pm 2 \times \sqrt{\frac{\sum_{i=0}^{n}(h_i - h_m)^2}{n-1}} \qquad \textbf{(Eq. 2.10)}$$

Where h_m is the mean value and n the number of lines.

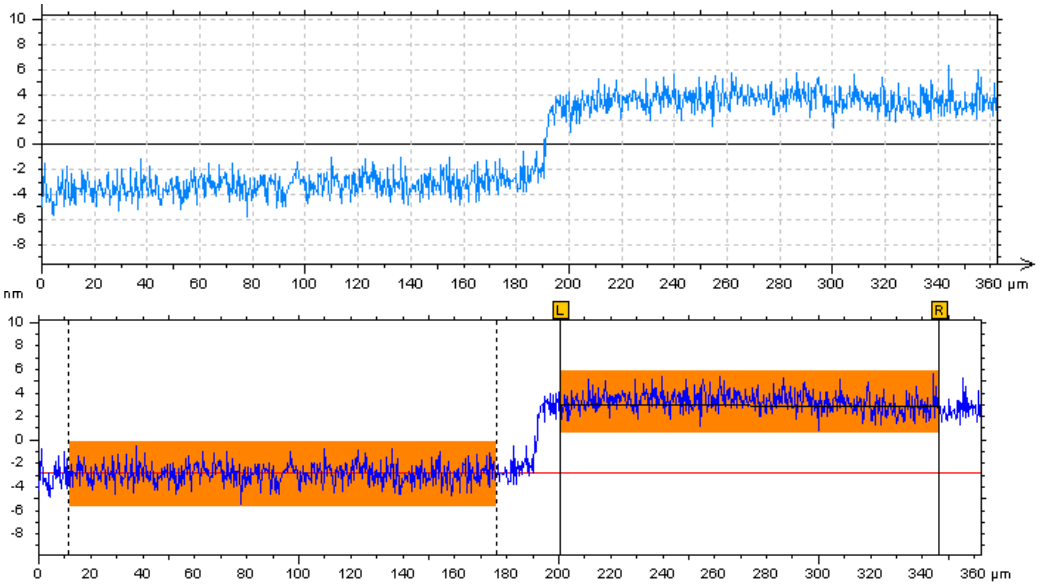


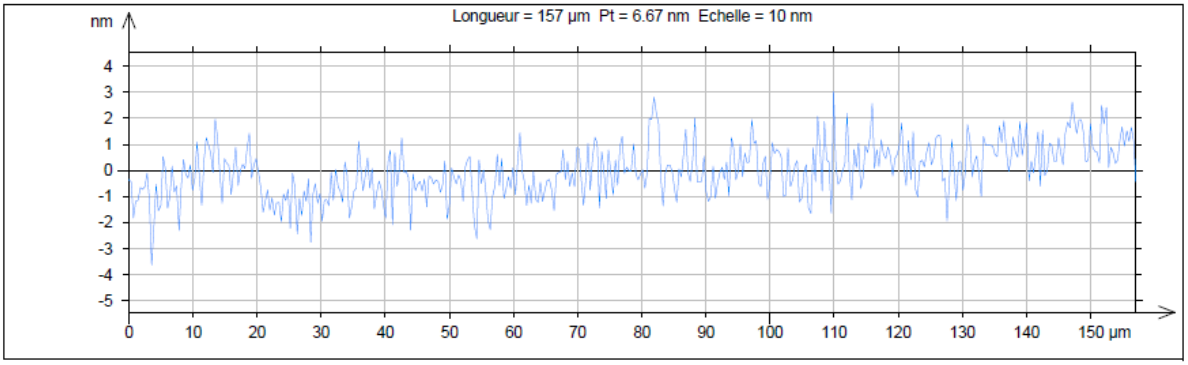
Figure 2.14: Section view of step height measurement (scale in nm) (top). Determination of the step height between the un-implanted zone and the implanted one (swelling) (bottom).

Figure 2.14 is an example of one height-line obtained after implantation. As you can see the line shows a background noise that can induce errors in the step height determination. To minimize such errors the line was integrated over a large distance and its mean value is then calculated. In this case, the step heightt h_s was estimated to be :

$$h_s = 6.3 \pm 0.3 \text{ nm}$$

2.3.4. Roughness measurement

The surface roughness, R_q (root mean square) and R_a (arithmetic average), can be measured by the same method with the scanning image, see the profile of the surface figure 2.15. Both surface roughnesses can be determined by an automatic program. To get more reliable results, the procedure was applied three times. In the as-studied case both roughness, R_q and R_a were estimated to be 0.6 nm and 0.5 nm, respectively.



Paramètres calculés sur le profil 6pda 400 > ...
> Profil extrait

* Paramètres calculés par moyenne de toutes les longueurs de base.
* Un filtre de microrugosité a été utilisé, avec un cut-off de 2.5 µm.

Paramètres de rugosité, Filtre gaussien, 78.5 µm

Rq = 0.598 nm
Ra = 0.487 nm

Figure 2.15: (top) Section view of the surface roughness measurement showing the irregularities of the SiC surface. (bottom) average roughness calculated by the roughness measurement option for all of the measured profiles.

2.4 Transmission Electron Microscopy (TEM)

TEM is a technique whereby a uniform and coherent beam of energetic electrons are transmitted through a thin specimen, interacting with the specimen atoms. This interaction modulates the intensity distribution of the transmitted beam, thus providing information of the sample microstructure which can be recorded as electron diffraction pattern or magnified images.

TEMs are capable of imaging at a significantly higher resolution than light microscopes, owing to the small de Broglie wavelength of electrons. This enables the instrument's user to examine fine detail—even as small as a single column of atoms, which is thousands of times smaller than the smallest resolvable object in a light microscope. TEM forms a major analysis method in a range of scientific fields, in both physical and biological sciences. TEMs find application in cancer research, virology, materials science as well as pollution, nanotechnology, and semiconductor research.

At smaller magnifications TEM image contrast is due to absorption of electrons in the material, due to the thickness and composition of the material. At higher magnifications complex wave interactions modulate the intensity of the image, requiring expert analysis of observed images. Alternate modes of use allow for the TEM to observe modulations in chemical identity, crystal orientation, electronic structure and sample induced electron phase shift as well as the regular absorption based imaging.

In my work cross-sectional TEM (XTEM) was used to study the damaged region induced by Xe implantation before and after annealing. TEM images were obtained from a JEOL 2200 FS with FEG operating at 200 kV (figure. 2.16), equipped with a STEM mode, a high angle annular dark field (HAADF) detector and an in-column Omega Filter.



Figure 2.16: JEOL 2200FS is available in the department of physics and mechanics of materials.

Sample preparation

In TEM, the preparation of ultra-thin samples is required to be transparent to electrons. Typically the thickness of samples is ranging from few nanometers for studies in high resolution to about hundreds of nanometers for conventional studies. Cross-sectional samples were prepared in order to characterize the microstructure evolution induced by Xe implantation as a function of depth. It is a delicate preparation as the sample must be transparent to the electron beam.

We have used the mechanical milling and the ion etching to prepare the TEM specimen. See following figure 2.17 which shows the sample preparation procedure. At first, we need to cut the desirable sample to a right width about 2.5 mm. Second, we glue the implanted faces together and cut it into serval lamella of thicknesses of about 300 µm. Then a mechanical polishing is proceeded by using diamond discs from 15 to 1 µm with a tripod until all scratches are removed. The specimen is slicked to a special 3 mm TEM grid or slot for TEM observations. Finally, the specimen is then submitted to a low Ar^+ flow (3 kV) until electron transparency (small hole in the as created cross-section).

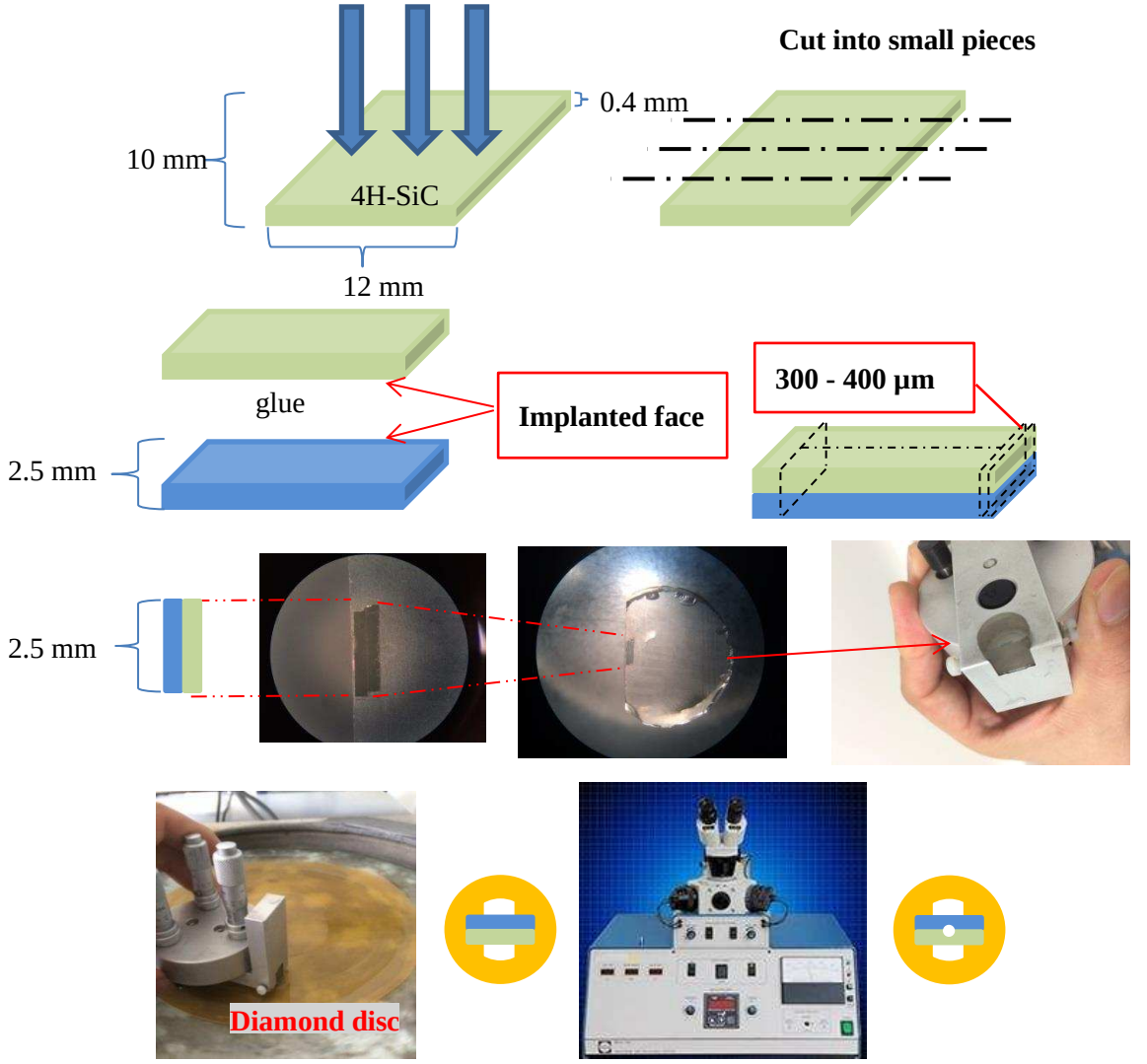


Figure 2.17: Schema of TEM specimen preparation by using a tripod and PIPS.

2.5 Thermal annealing

In our study, we used a home-made lamp oven allowing temperature annealing up to 1400 °C, see figure 2.18. The oven is made up of different parts including a high-temperature chamber of a cylindrical structure with 6 halogen lamps achieving the uniformity of the given temperature. It is controlled by a temperature regulator that permits us to monitor the heating rate. Before heating, the chamber was submitted to an Ar flow. For all the experiments the heating rate was fixed at 20 °C/sec and the vacuum was around 10^{-7} Pa. The sample holder (in the inset of figure 2.18) is in graphite and allows annealing SiC samples of 1 x 2 cm^2 in this configuration. Different experiments were conducted to test the reproducibility of the oven (calibration, duration, cumulative experiments, annealing sequence…).

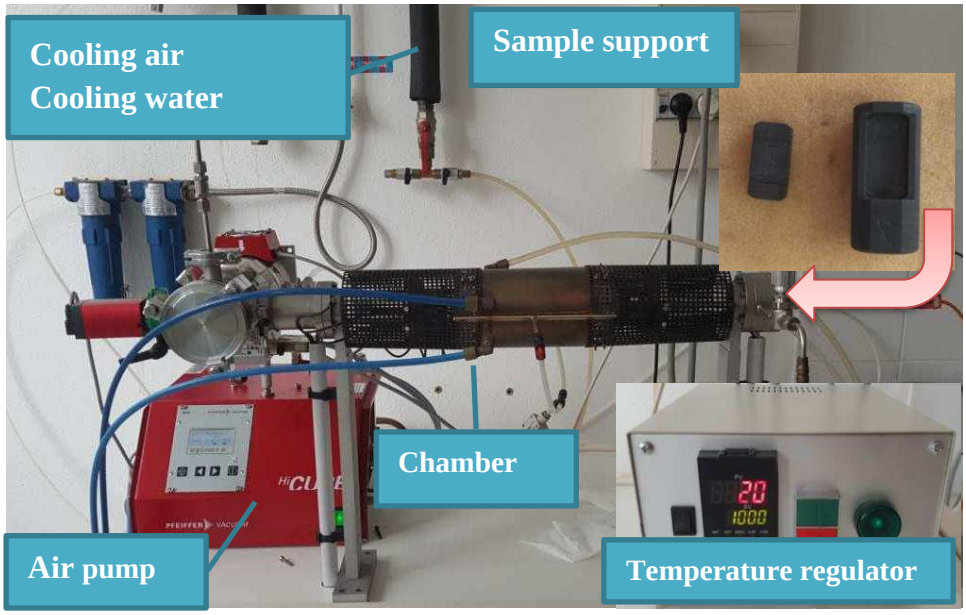


Figure 2.18: Illustration of the lamp-oven used in this study. In the inset the sample holder.

Calibration of the lamps annealing oven

To check the temperature consign we proceeded the following experiments; the temperature was fixed at 800 °C (and at 500 °C) and its evolution in the chamber was recorded as a function of time, see figure 2.19a. As seen the curve can be divided into 4 parts. After a short time of starting (less than 10s), the temperature rises rapidly up to 850 °C (heating rate of about 20 °C/s) that is over the set temperature of 800 °C. This 6 % of overheating is called the transition phase for a duration of about 20s. Then the temperature of 800 °C is stabilized: this is the annealing phase. So the set temperature is reached is about 1 min. But in the case of the 500 °C-annealing, the maximal temperature reached 600 °C, figure 2.18b. This 20 % of over-temperature is estimated too high and could affect the final result. So to minimize any temperature error, we decided to conduct annealing experiments with **temperature differences of 200 °C**.

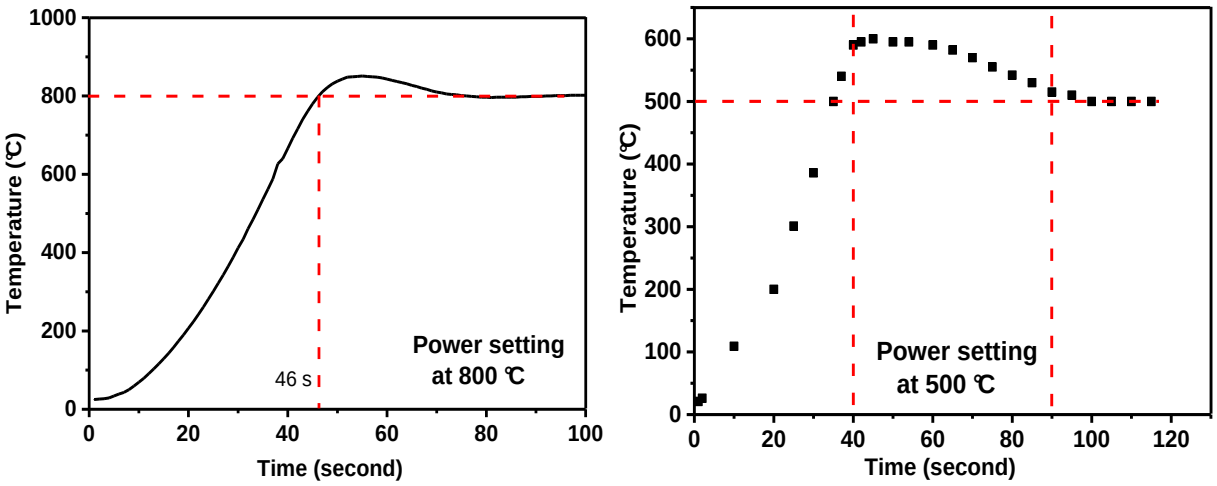


Figure 2.19: Calibration of the annealing oven at 800 °C (a) and 500 °C (b). Curves show that the measured temperature exceeds the setpoint during a few of seconds.

Duration of annealing

The efficiency of annealing must be understood especially in the study of strain recovery. A 4H-SiC specimen was implanted at 400 °C - 540 keV with a fluence of 3 x 10^{14} Xe.cm^{-2} (1 dpa) and then cut into different parts. Annealing durations of 4 and 30 min. were then conducted. X-ray diffraction technique was used to compare the differences between the annealing duration on the elastic strain recovery, in a large range of temperatures from 400 to 1200 °C. Figure 2.20 shows the XRD spectra of Xe-implanted SiC and then annealed at 4 and 30 min. As seen, no difference in the spectra is evidenced showing that **annealing durations are equivalent to the range 4 - 30 min (for the strain recovery).** Table 2.2 shows that this equivalence is operative over the entire temperature of annealing.

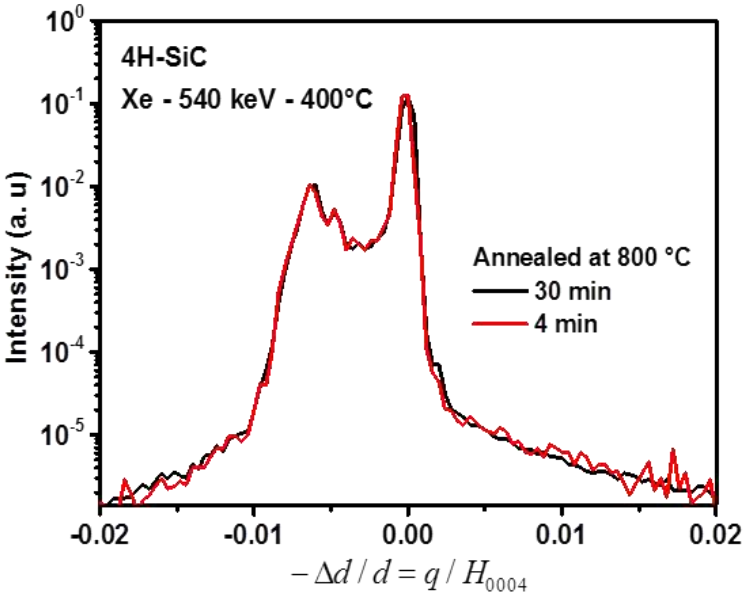


Figure 2.20: X-ray diffraction profiles after annealing at 800 °C for 30 min and 4 min. The SiC samples were implanted (together) with 1 x 10^{14} Xe.cm^{-2} at 400 °C-540 keV.

Temperature	30 min	4 min
	maximum strain %	
400 °C	1.24	1.24
600 °C	0.76	0.76
800 °C	0.64	0.60
1000 °C	0.48	0.48
1200 °C	0.16	0.16

Table 2.2: Comparison of the elastic strain (XRD) for annealing duration of 30 and 4 min.

Annealing sequence (single or cumulative)

It is very curious to understand the difference if a sample is annealed little by little to reach the final target temperature (multi-temperature annealing) or annealed in only once (single annealing). Consequently, a Xe-implanted 4H-SiC was cut into 4 small pieces (labeled A, B, C, and D) and then annealed at given temperatures but with different procedures. The resulting elastic strain was determined, as usual, by using XRD. Sample A was annealed successively from 500 to 1200 °C whereas sample B, was annealed at 600 °C, sample C was annealed at 800 °C and sample D at 1000 °C. Table 2.3 indicates that the maximal strain for each temperature annealing is similar by using the two methods (single or cumulative). Deviations are negligible allowing us to spare money (SiC samples are so expensive!). To illustrate the similarities of both procedures, Figure 2.21 shows no difference in the XRD spectra of samples annealing at one time or by using successive steps up to 1000 °C. **Single or cumulative annealing are similar (strain recovery).**

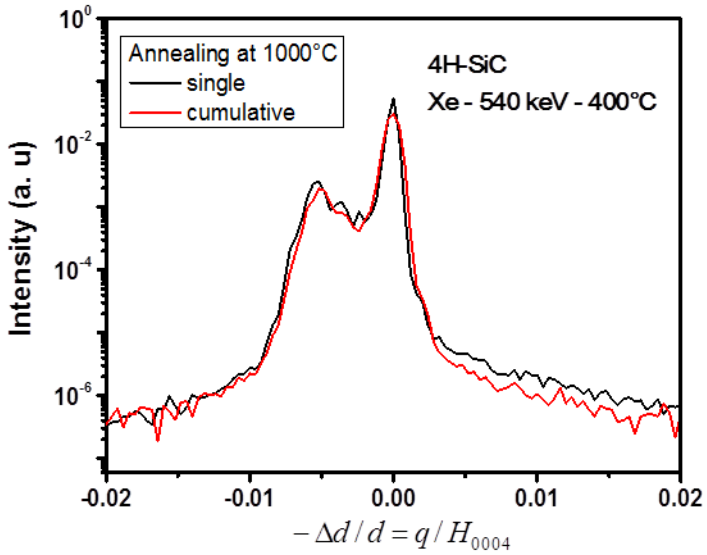


Figure 2.21: X-ray diffraction profiles after annealing at 1000 °C for 30 min according to the annealing procedure (single or cumulative). The SiC samples were implanted (together) with 10^{14} Xe.cm^{-2} at 400 °C-540 keV.

Temperature	Multi-temperature	Single-annealing		
	Maximum strain %			
	A	B	C	D
400 °C	1.24	1.24	1.24	1.24
500 °C	0.76			
600 °C	0.76	0.72		
800 °C	0.60		0.64	
1000 °C	0.48			0.48
1200 °C	0.16			

Table 2.3: Comparison of different annealing sequences on the strain.

Concluding remarks

This chapter has presented the main techniques used during this thesis and allowed us to specify the following points:

In SiC :

- **Unique or multiple implantations are equivalent in the strain build-up**
- **Strain recovery occurs during the first minutes of annealing (< 4min)**
- **Cumulative (or step by step) and unique annealing are equivalent in strain recovery**

Chapter 3

Results and discussions

This chapter represents the backbone of our work on the effects of Xe-implantations on single crystals 4H-SiC according to the conditions of implantation (temperature and fluence) and subsequent annealing up to 1400 °C. It is divided into four main subsections. In the first section, general results are presented. The Xe-migration was studied trough TDS experiments conducted at high temperature and considerations concerning the elastic strain profile are highlighted according to simulations of XRD curves. Then the evolution of damage under implantation is presented with increasing temperature of implantation: low-temperature regime up to 300 °C, at 400 °C for a large range of fluences and its evolution under subsequent annealing and finally in the high-temperature regime up to 800 °C. The implantations at 400 °C were studied in details by using different techniques (XRD, TEM …) and compared with previous works on helium-implanted SiC conducted in the laboratory. This allows us suggesting a phenomenological model to describe the evolution of the strain with implantation parameters (temperature and dose). Results are discussed all in the manuscript.

3.1 General results

3.1.1 TDS measurements at 1350 °C

In order to analyze the mechanisms involved in Xe diffusion, we carried out Thermal Desorption Spectrometry (TDS) measurements on the PIAGARA (Plateforme Interdisciplinaire pour l'Analyse des GAz Rares en Aquitaine) platform at CENBG laboratory in Bordeaux (collaboration E. Gilabert). TDS experiments were carried out on Xe implanted SiC samples implanted at 400 °C in the low fluences range, from 10^{12} to 5 x 10^{13} Xe.cm^{-2}. The experiment involves heating a sample in a small furnace to induce rare gases movement and release and using mass spectrometry to monitor the amount of gases released as a function of time. Interpretation of the release experiments enables us to determine xenon diffusion coefficients in Xe-implanted SiC. Experimental details are given in [68]. All the TDS experiments were conducted at a fixed temperature (furnace) of 1350 °C. Note also that this apparatus is very sensitive to roughly 10^8 rare gas atoms with an error of about 2.5 %.

Figure 3.1 plots the isothermally TDS desorption data measured at 1350 °C in 400 °C-Xe-implanted SiC in the low fluence regime (< 5 x 10^{13} cm^{-2} – 0.15 dpa - $c_{at.}^{max} = 0.005$ %). As seen at the lowest fluence, 1 x 10^{12} cm^{-2}, the released fraction of Xe reaches almost 100 % after 100 min of annealing. With increasing fluence, the rate drastically changes. For implanted fluence of 3 x 10^{12} cm^{-2}, the amount of xenon released is only of 3 % after 100 min of annealing. It slightly increases to reach 4 % after 350 min (saturation regime). The value at saturation decreases with increasing fluence. At 5x10^{13} Xe.cm^{-2}, less than 1 % of Xe-atoms are released after a 300 min annealing at 1350 °C suggesting a very low coefficient of diffusion.

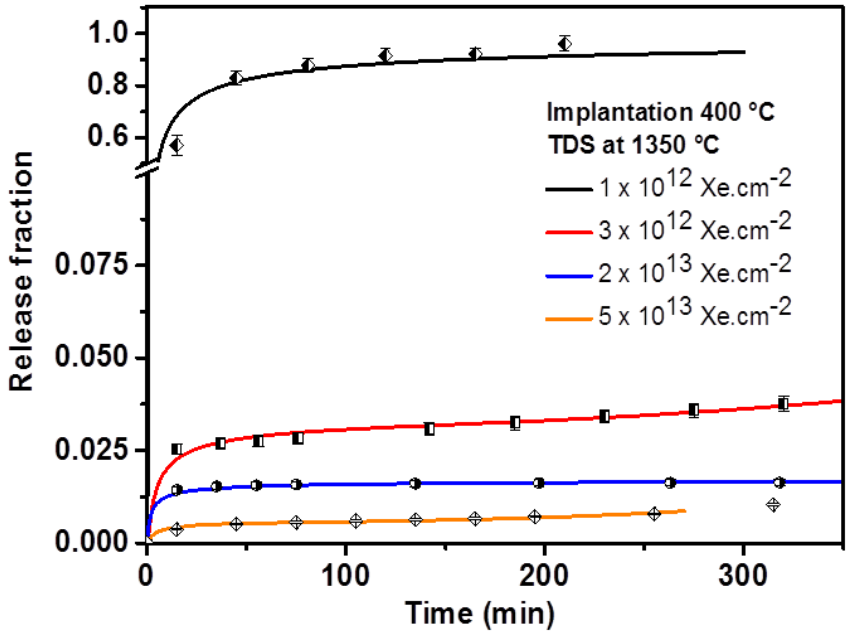


Figure 3.1: TDS measurements conducted at 1350 °C in 540 keV-Xe-implanted 4H-SiC.

The evolution of the released-gas fraction during the annealing was simulated using the diffusion equation, namely:

$$\frac{\partial c(x,t)}{\partial t} = \frac{\partial}{\partial x}\left(D(x)\frac{\partial c(x,t)}{\partial x}\right) \qquad \textbf{(Eq. 3.1)}$$

and by using the following limit conditions:

$$c(0,t) = 0\,; c(\infty,t) = 0 \;\; and\; by\; taken \;\; c(x,0) = SRIM - profile \qquad \textbf{(Eq. 3.2)}$$

where x is the depth, t the annealing time, and D the coefficient of diffusion (m^2s^{-1}).

Burst release is sometimes observed in the first minutes of experiments; its origin is generally ascribed to surface oxidation or intergranular diffusion. In our experiments, this burst release is weak and was thus not taken into account. The simulations based on Fick's law have been optimized by taking two coefficients of diffusion; there are the continuous lines in figure 3.1. The fitting parameters are listed in table 3.1.

T=1350°C	$D_1(cm^2s^{-1})$	$F_1(\%)$	$D_2(cm^2s^{-1})$
1 x 10^{12} cm^{-2}	~ 7 x 10^{-17}	100	-
3 x 10^{12} cm^{-2}	~ 5 x 10^{-17}	3.6	~ 1 x 10^{-25}
2 x 10^{13} cm^{-2}	~ 2 x 10^{-17}	1.65	~ 1 x 10^{-28}
5 x 10^{13} cm^{-2}	~ 7 x 10^{-17}	0.65	~ 1 x 10^{-25}

Table 3.1: Fitting parameters of TDS experiments at 1350 °C in Xe-implanted 4H-SiC at 400 °C.

Table 3.1 shows that the coefficients of diffusion are roughly the same in the studied range of fluences suggesting the same mechanism of Xe diffusion at this temperature of 1350 °C. On the other hand, the fraction of Xe release in the first stage varies enormously. For the lowest fluence, all the Xe atoms are released in the first stage, D_1(1350 °C) ~ 2 - 7 x 10^{-17} cm^2s^{-1}, whereas at higher fluence the waste majority of Xe does not migrate or diffuse. The second stage of diffusion characterized by the coefficient D_2 is low, too low in some cases to be simulated (within the limit of errors). This clearly shows the trapping of Xe for fluences higher than 1-3x10^{12} cm^{-2}. This is in good agreement with recent results obtained on 6H-SiC reporting no diffusion or loss at 1400 °C of the implanted noble gases (Xe and Kr) at fluences larger than 1 x 10^{16} cm^{-2} [69]. Similarly, implantations were conducted at elevated temperature, 600 °C, to avoid amorphization.

Discussion on TDS measurements

TDS results suggest that Xe-atoms are in two different configurations according to the implanted fluence. At low fluences, they are mobile whereas at higher fluences not. The properties of noble gas atoms were investigated by Pizzagalli et al. [70] by using first-principles calculations. Interestingly they compare the formation energies of the noble gas depending on possible conditions. They showed that it more energetically favorable to form a divacancy containing the Xe-atom than a Xe interstitials. For heavy gases, it is even energetically cheaper to create a mono or divacancy. On the contrary, He-atom can be in interstitial positions. Figure 3.2 shows the formation energies of the different noble gas atoms under different conditions.

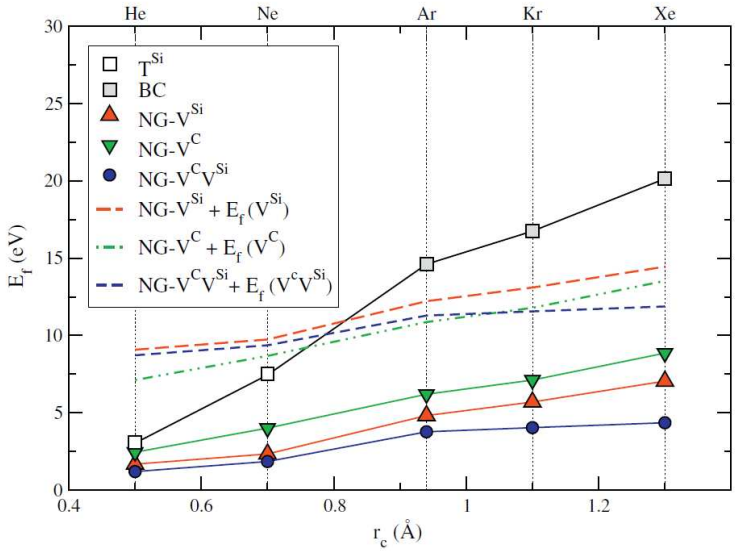
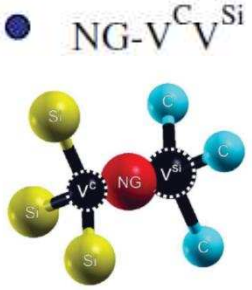


Figure 3.2: Formation energies of NG defects under different configurations; electronic structure calculations [70].
T: Tetrahedral interstitial position
BC: Bond Centered position



So, calculations display that Xe-atoms prefer to occupy divacancies if available. SRIM calculations show that Xe-implantation creates a large number of vacancies (~ 4450 Vac/Xe with no dynamic recombination). We can thus suggest that the "rapid" diffusion of Xe at 1350 °C, D_1(1350 °C) ~ 2 - 7 x 10^{-17} cm^2s^{-1}, results from the diffusion of I_{Xe} or Xe-V defects since it is dominant at low

fluence for which the number of as-created vacancies is not sufficient. With increasing fluence, the number of available vacancies becomes sufficient to trap the Xe-atoms by forming vacancy-type defects such as Xe-V^cV^{Si} limiting thus the Xe-release even at 1350 °C.

Above a fluence of 10^{13} Xe.cm^{-2} all the Xe-atoms are trapped in the SiC matrix: no significant long-range Xe-diffusion occurs at 1350 °C

3.1.2 X-ray diffraction simulations

Experimental XRD curves were simulated to determine the strain profile by using a web-based program written by S. Stepanov [64] and according to a procedure similar to the one already used for helium implantation by S. Leclerc [49]. The surface layer was divided into 100 sublayers of 30 Å width; the Debye-Waller-like factor W_h was taken equal to 1 in the all strained zone except after amorphization (no diffraction lines on the XRD curves) for which W_h=0. The input parameters of the simulation are given as an example in Figure 3.3. The simulations were performed with the geometry coplanar diffraction with the Bragg plans parallel to the surface. The Miller indices of the Bragg reflection are (0004). The normal strain $(da/a)_z$ will be noted $(\Delta d/d)_N$. According to Dederichs [71] the normal strain is supposed to be proportional to the point defect concentration and independently of their state of clustering: $(\Delta d/d)_N^{Cluster} = n(\Delta d/d)_N^{Point\ defects}$, where the cluster is created by n point defects. As the beginning for the simulations, the normal strain $(\Delta d/d)_N$ was taken similar to the vacancy distribution calculated by TRIM 2008 [61], see figure 3.4. This $(\Delta d/d)_N$ profile has been modified progressively to fit with the experimental XRD curve.

Figure 3.3 shows an example of simulation made on a 5 x 10^{13} Xe.cm^2 implanted SiC at 300 °C (0.15 dpa). As seen the simulation pattern fits well the experimental curve. The as-resulting strain profile is compared with the ion and vacancy profile. The maximal strain is simulated to be 1.1-1.2 % in good agreement with the one given by the position of the last fringe on the experimental XRD curve. At 300 °C - 0.15 dpa the strain profile seems to be the combination of the vacancy and ions profile, extending up to 250 nm in depth. The resulting elastic surface swelling, h_e, can thus be calculated by using:

$$h_e = \int_0^{+\infty} \left(\frac{\partial d}{d}\right)_N (z)\, dz \qquad \textbf{(Eq. 3.3)}$$

In this example, 5x10^{13} Xe.cm^2 implanted SiC at 300 °C (0.15 dpa), the elastic contribution, h_e, to the step height, h_s, is estimated to be 1.9 nm. The simulation of XRD curves being sometimes long and tedious, the elastic contribution will be estimated by simply taken $h_e = \left(\frac{\Delta d}{d}\right)_N^{max} \times R_p$. Note also

that the implantation induced strain deduced from XRD measurements differs from the one of free standing solid due to the substrate reaction. This difference has been recently estimated to be of 16% [72].

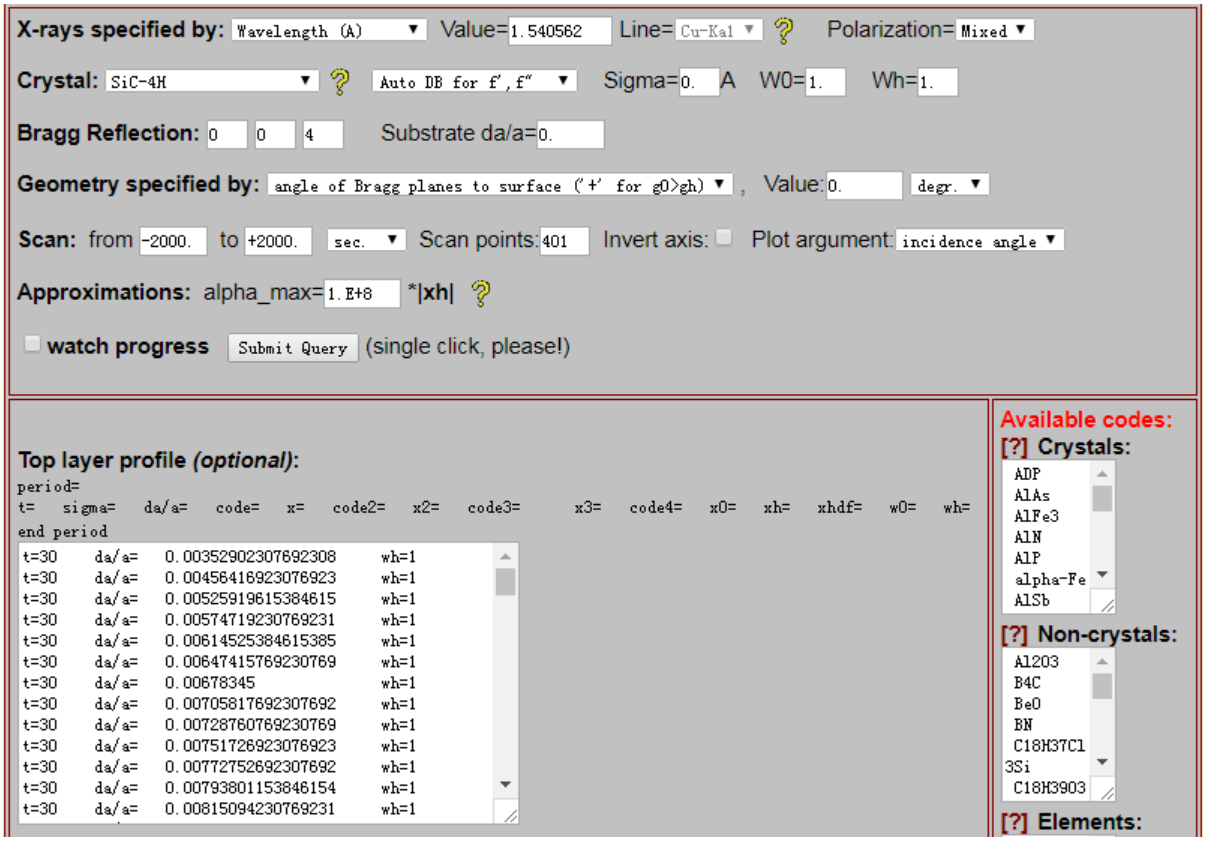


Figure 3.3: Input simulation template to determine the strain profile in Xe-implanted SiC.

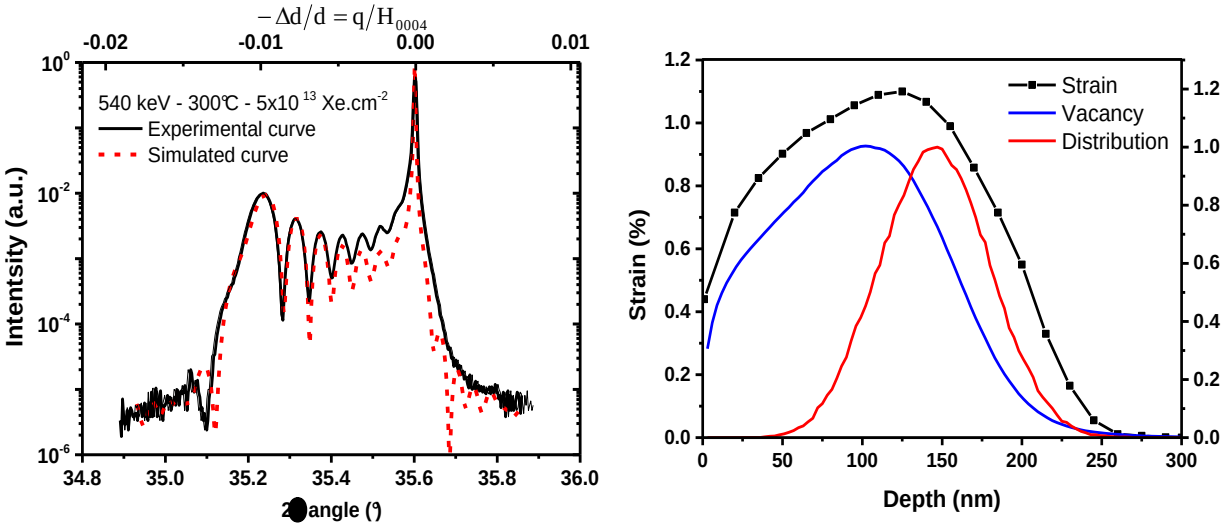


Figure 3.4: Comparison of experimental XRD and simulated curves (red) for 300 °C –5 x 10^{13} Xe.cm^{-2} implanted SiC (left) and the as-determined strain profile (right). For comparison, the vacancy and ion profiles are also plotted (SRIM simulation).

However, with increasing fluence, it is increasingly difficult to obtain a reliable and unique profile, and this is supported by the fact that the X-ray diffraction is not sensitive to depth and the absolute distribution of the strain profile with respect to the implanted surface. It may, however, be stated that the strain profile can be produced deeper than the distribution of Xe-atoms. Figure 3.5 shows that a relatively good fit can be observed on a 400 °C – 5 x 10^{14} Xe.cm^{-2} (1.5 dpa) implanted SiC resulting in a strain profile extending up to 400 nm approximatively suggesting that another mechanism is operative at high fluence (as the defect-assisted-diffusion under irradiation).

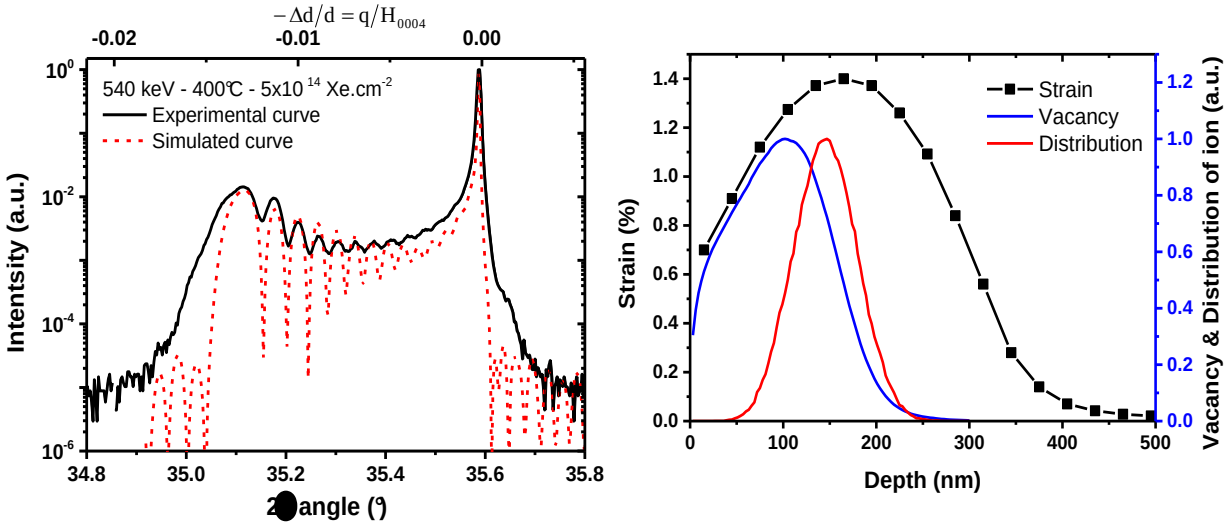


Figure 3.5: Comparison of experimental XRD and simulated curves (red) for a 400 °C – 5 x 10^{14} Xe.cm^{-2} implanted SiC (left) and the as-determined strain profile (right). For comparison, the vacancy and ion profiles are also plotted (SRIM simulation).

This spreading out of the Xe-implanted-strain towards the depth was not reported or observed with helium atoms. On the contrary, with increasing fluence it has been reported that the He-induced strain profile becomes narrower in the region of maximum deposited energy at higher fluences [49]. This last point will be discussed in relation to the TEM observations when possible (or when they were done). Nevertheless, the maximal strain fits well with the one experimentally determined by the position of the last fringe (2 - 2.1 %). In this case, the elastic contribution could not be approximated but only calculated by using the Eq. 3.3.

3.2 Damage evolution in the low-temperature regime

The low implantation-temperature regime, from RT to 300 °C, refers to the temperature of implantation leading to the amorphization of the SiC target or being at the limit of the transition. The four temperatures of implantation, RT, 200, 250 and 300 °C were studied through the implantation damage.

3.2.1 Room temperature Xe-implantations

XRD measurements

The implantations were performed with fluence ranging from 2 x 10^{12} to 1.45 x 10^{14} Xe.cm^{-2} related with doses from 0.006 to 0.435 dpa. Figure 3.6 displays the XRD intensity patterns with increasing fluence. All the XRD curves show a similar shape: a main Bragg peak ($-\Delta d/d$ = 0) and then a diffracted intensity characteristic of dilatation gradient along the surface normal surface direction [55]. The maximum strain value ε_{max} *is* determined from the position of the last fringe of the XRD curve: it increases with dose.

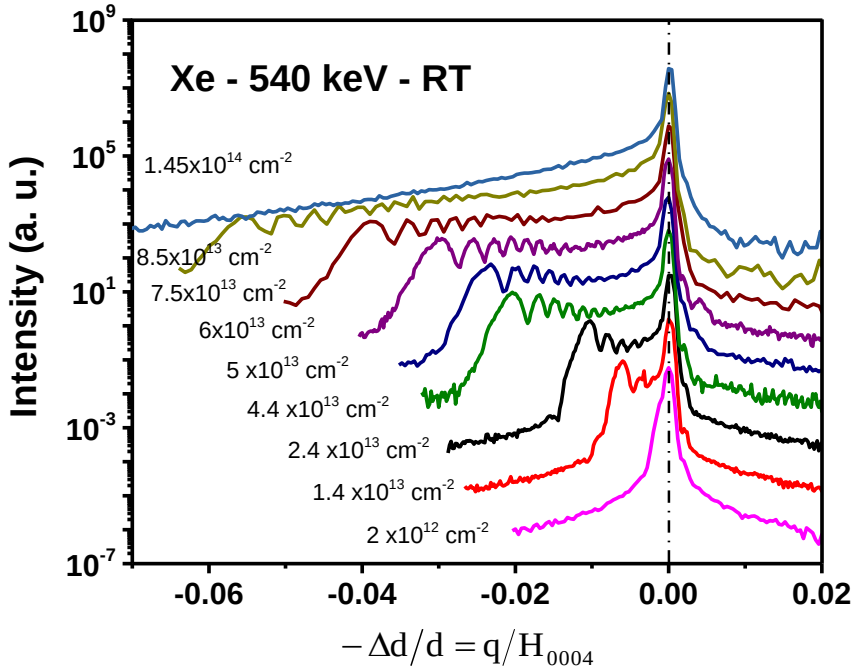


Figure 3.6: X-ray scattered intensity distributed along the normal surface direction close to the (0004) reflection, in room temperature Xe-implanted 4H-SiC with fluences ranging from 2 x 10^{12} (0.006 dpa) to 1.45 x 10^{14} cm^{-2} (0.435 dpa).

Figure 3.6 shows that all XRD curves result in a Bragg's peak and a diffracted intensity toward the low angle side. Up to 8.5 x 10^{13} Xe.cm^{-2}, fringe pattern is observed that is characteristic of a dilatation gradient, with a maximal strain value increasing from 0.12 % at 2 x 10^{12} cm^{-2} to 5.6 %. At higher fluence 1.45 x 10^{14} cm^{-2}, there are no more interference fringes observed on XRD pattern suggesting that the amorphous transition is reached. The crystalline to amorphization transition is thus in the range 0.25 - 0.43 dpa in good agreement with previous results, see table 1.3. The maximal strain is plotted versus dose in figure 3.7.

As seen the evolution is roughly linear in the whole range of dose, with an apparent cross-section of $\sigma_{app}^{RT} \sim 20\ \%.dpa^{-1}$. Linear dependence of strain with dose was also reported in RT-helium-implanted SiC at RT [55].

$$\varepsilon_{max}^{RT} = \sigma_{app}^{RT}.\emptyset \qquad \textbf{(Eq. 3.4)}$$

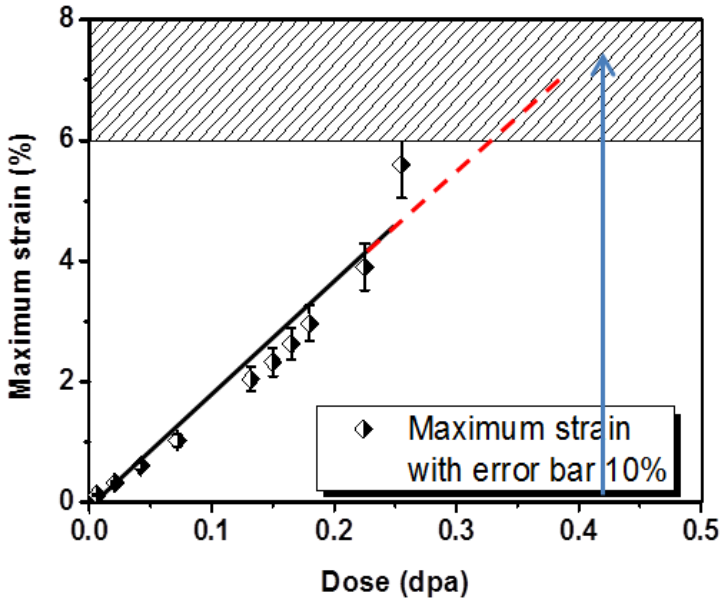


Figure 3.7: Evolution of the maximal elastic strain as a function of dose (dpa) in Xe ions implanted at RT for 540 keV (estimation of error of 10 %). For a 0.4 dpa implantation, the amorphous state is reached (blue arrow).

Swelling measurements

Figure 3.8 displays the variations of the step height versus dose. For comparison, the data of elastic strain are also plotted (the elastic strain has been approximated, see &3.1.2). As seen in the low dose regime, the height seems to increase linearly with increasing implantation dose as the elastic contribution. Only point defects are thus supposed to play a role in the swelling effect in this low dose regime. The step height measurements are however difficult to exploit because of the additional errors providing from the position of the mask for cumulative fluences, see figure 3.8.

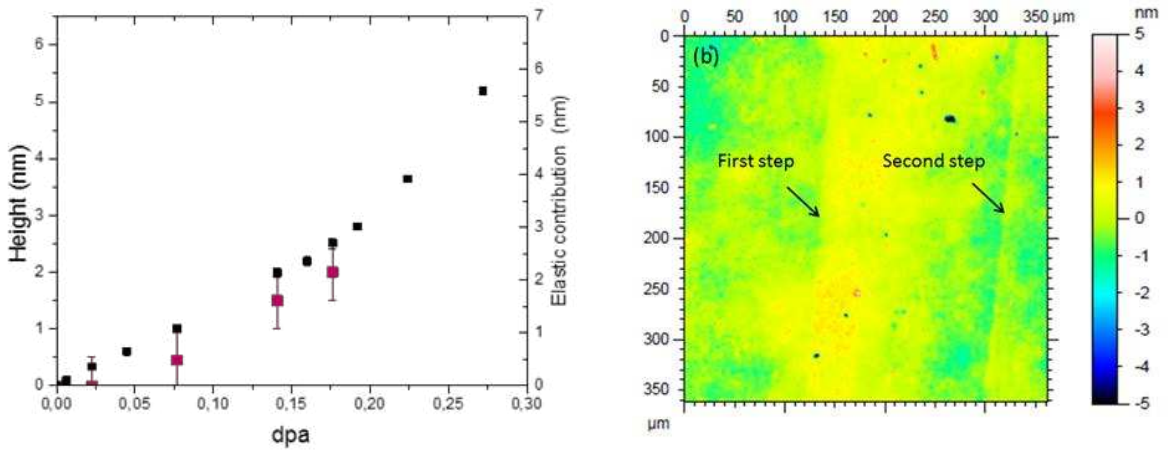


Figure 3.8: Swelling measurements (red point) compared with the expected elastic contribution (black plot) (left). Step height measurement image obtained for the two cumulative fluences of 4.4 and 5.5 x 10^{13} Xe.cm^{-2} (right).

TEM observations

Figure 3.9 shows the XTEM observed in the 2.4 x 10^{13} Xe.cm^{-2} implanted SiC at RT (0.072 dpa). A zone made of different spots of dark contrast is clearly seen around the mean projected range of Xe-ions, distinguishing the damaged zone up to a depth of 250 nm approximately. The diffraction pattern in the most damaged zone shows that the area is still crystalline; the maximal strain is of about 1 %. HRTEM observations were also conducted in this sample, see figure 3.10. On the undamaged area, the dense planes (0004) are clearly seen whereas after implantation the HRTEM image shows a blurred aspect. The basal planes are still observed: no discontinuity is evidenced. The contrast is ascribed to small distortions that have not impact on the crystallinity.

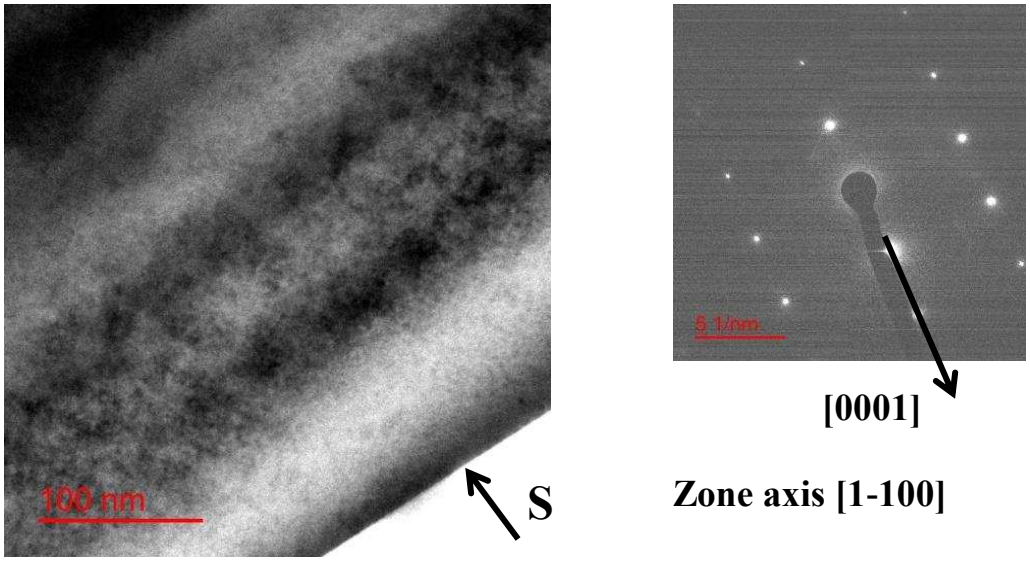


Figure 3.9: XTEM image showing a zone highly perturbed close to the mean projected range of Xe-ions. The sample was implanted at RT with 540 keV - 2.4 x 10^{13} Xe.cm^{-2} (a). The diffraction pattern was taken on the damaged area which is still crystalline (b).

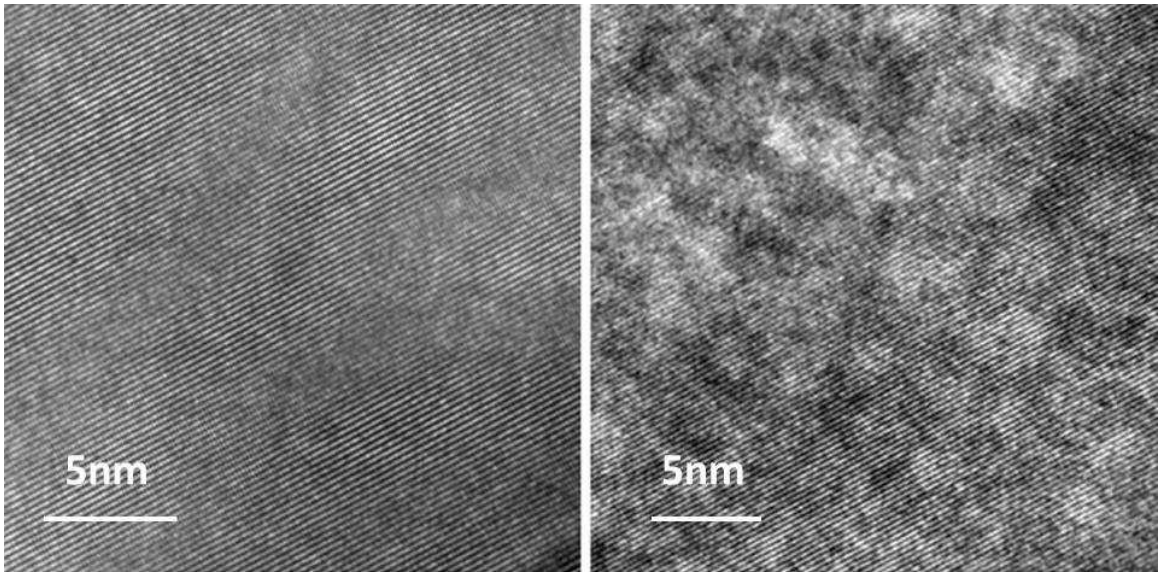


Figure 3.10: HRTEM images taken (left) on a perfect part of SiC and (right) on the highly damaged zone of a RT -540 keV - 2.4 x 10^{13} Xe.cm^{-2} implanted SiC (see figure 3.9).

3.2.2 Temperature of implantation up to 300 °C

200°C implantation

Figure 3.11 displays the corresponding XRD curves in 200 °C Xe-implanted SiC in the range 5 x 10^{12} to 4 x 10^{14} cm^{-2}. As observed for RT implantations the maximal strain increases with fluence up to the amorphization occurring in the range 1.6-1.9 x 10^{14} $Xe.cm^{-2}$ (or 0.6 - 1.2 dpa), at higher fluences compared to the RT-observations (&3.2.1).

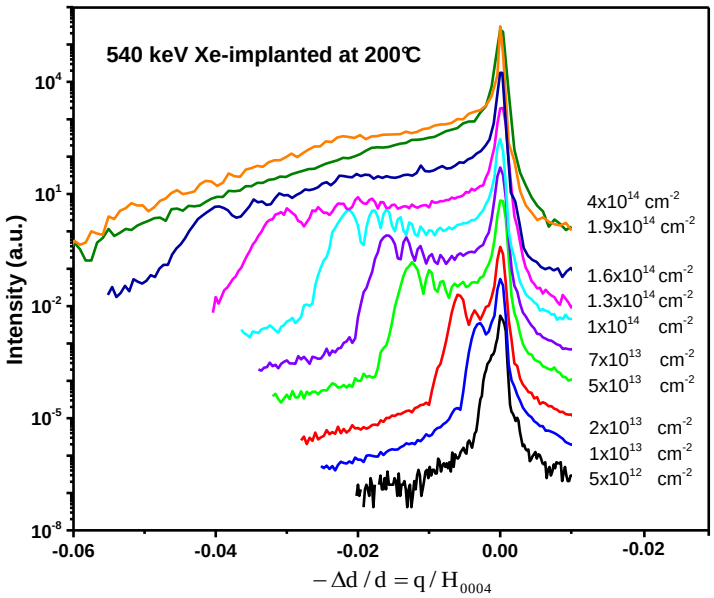


Figure 3.11: XRD curves for Xe-implanted 4H-SiC (540 keV) at 200 °C with increasing fluence from 5 x 10^{12} to 4 x 10^{14} cm^{-2}.

Moreover, it appears some noise in the XRD curves obtained for fluences larger than 1.6 x 10^{14} cm^{-2} (0.48 dpa). An asymmetric extending satellite peak seems to appear on the left side of the curves for 1.6 and 1.9 x 10^{14} cm^{-2}. Before the amorphous transition the evolution of the maximum strain is almost linear according to the increasing dose, see figure 3.12. At 200 °C, the apparent cross section is found to be $\sigma_{app}^{200°C} \sim 8 - 9\ \%.dpa^{-1}$.

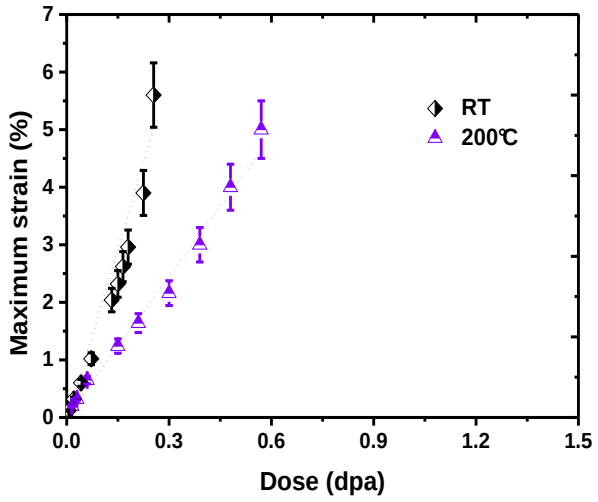
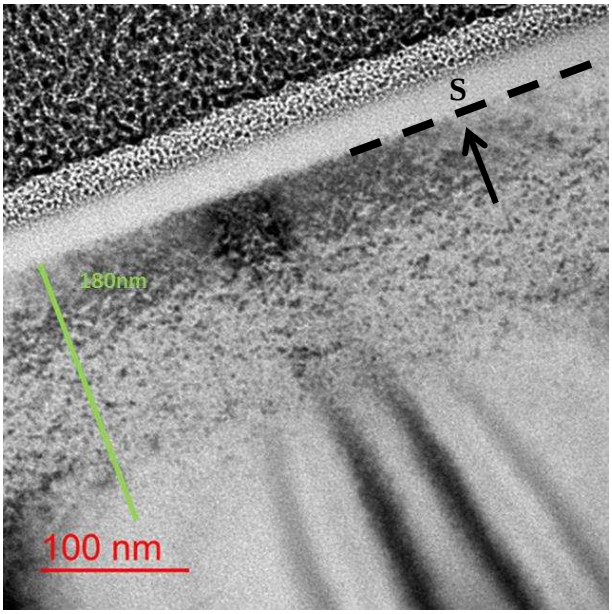


Figure 3.12: Evolution of the maximal elastic strain as a function of dose (dpa) in Xe ions implanted at **RT and 200 °C** for 540 keV (estimation of error: 10%).

XTEM observations were also carried out at this temperature of 200 °C and for two different fluences of 1.9 x 10^{14} cm^{-2} and 4 x 10^{14} cm^{-2}. Figure 3.13 summarizes the results obtained at the lowest fluence of 1.9 x 10^{14} cm^{-2} (0.6 dpa - ε_{max}~1.6 %). The XTEM analysis shows that the amorphous state is not reached. A damaged zone is visible up to approximately 180 nm in depth (~R_p + ΔR_p); the edges being less damaged – the defects are too small to be individually resolved or identified.



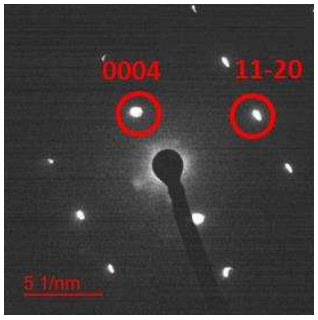
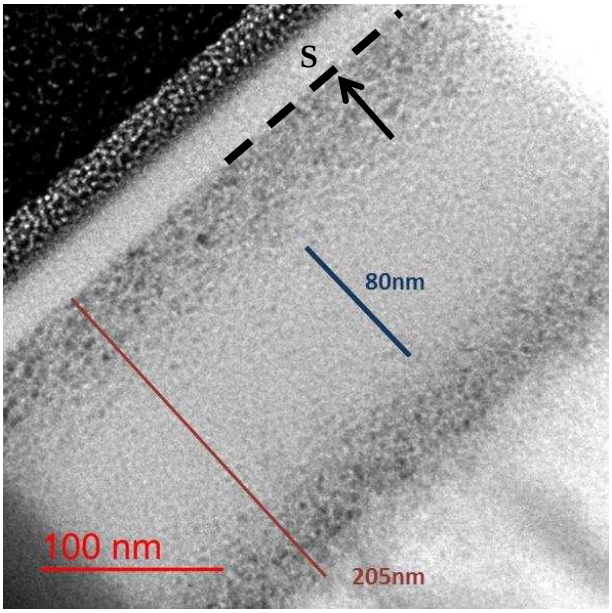


Figure 3. 13: XTEM image (FIB preparation) of 1.9 x 10^{14} cm^{-2} - 540 keV-Xe-implanted SiC at 200 °C (left) and the corresponding diffraction pattern (right) taken on the damaged area which is still crystalline.

With increasing fluence the amorphous transition is observed. This is clearly seen in the XTEM pictures, figure 3.14, obtained on the RT - 4 x 10^{14} Xe.cm^{-2} implanted SiC. The damaged band extends from the surface up to 200 nm approximately. The amorphous state is only observed in the middle of the band and its width is estimated close to 80 nm. HRTEM observation carried out on the deeper edge of the band shows that the highly perturbed zone beyond the amorphous zone contains amorphous pockets of less than 5nm, see figure 3.15.



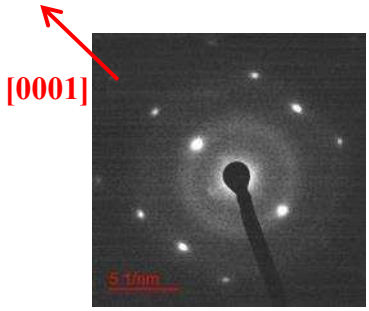


Figure 3.14: XTEM image (FIB preparation) of 4 x 10^{14} cm^{-2} - 540 keV-Xe-implanted SiC at 200 °C (left) and the corresponding diffraction pattern (right) taken on the whole damaged area showing that a part of the zone is in the amorphous state (halo ring).

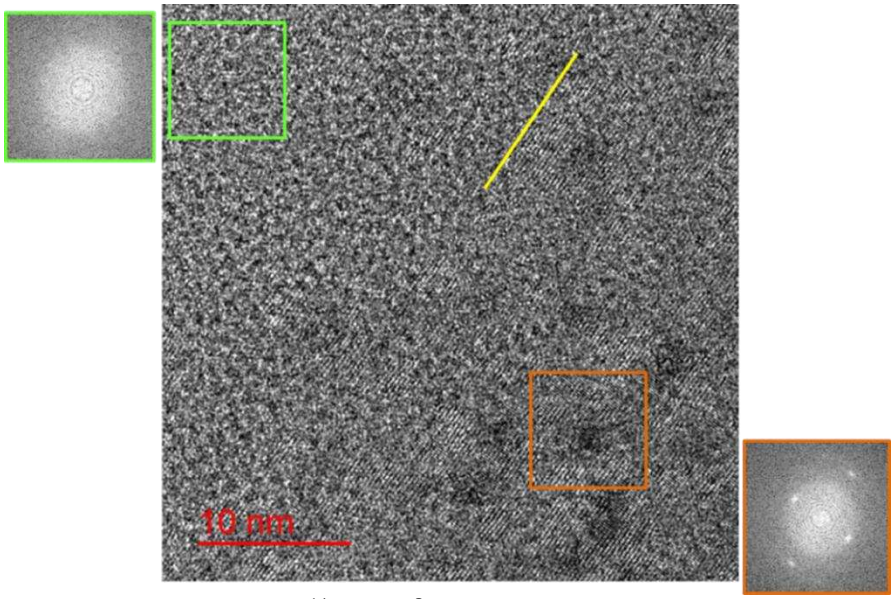


Figure 3.15: HRTEM image of 4 x 10^{14} Xe.cm^{-2} implanted SiC at 200 °C and the corresponding TF taken in the middle of the amorphous zone and towards the end of the damaged zone. The yellow line indicates the full amorphous transition.

250°C implantations

Figure 3.16 displays the XRD curves obtained for the 250 °C Xe-implantation and also plotted the evolution of the maximal strain versus dose. It can be noted that the amorphous transition occurs for fluence larger than 2.4 x 10^{14} cm^{-2}, so in the range 0.72 - 0.84 dpa. For lower fluences, the maximal strain linearly increases as function of dose with an effective cross-section of $\sigma_{app}^{250°C} \sim 4-5\ \%.dpa^{-1}$. The singularity reported at 200 °C, i.e. the appearing of a satellite peak, also occurs for fluences larger than 2 x 10^{14} cm^{-2}. Its position does not seem to vary with increasing fluence.

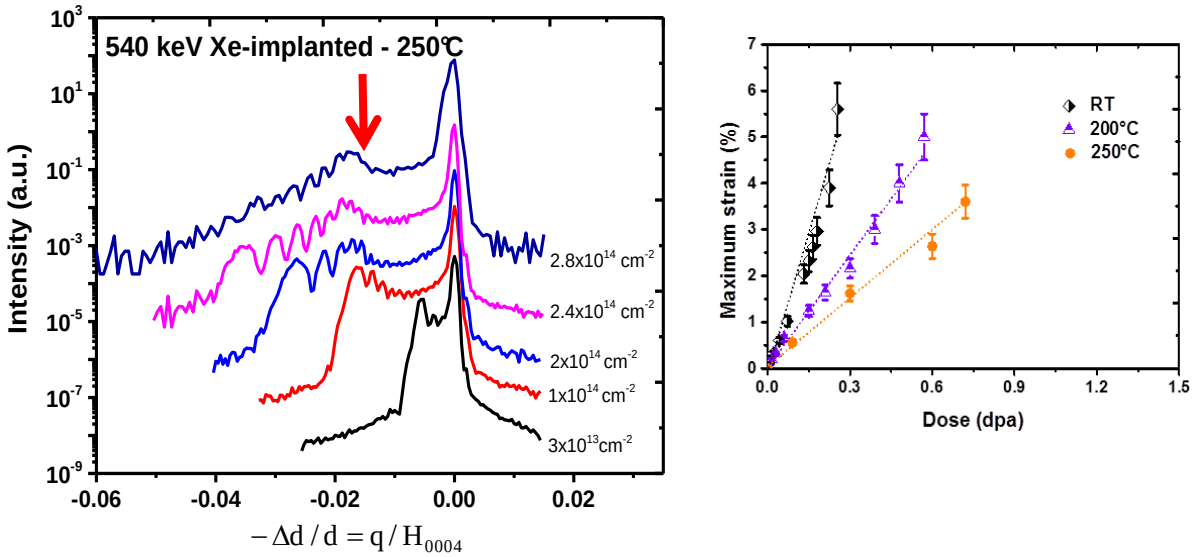


Figure 3.16: XRD curves for Xe-implanted 4H-SiC at 250°C, The arrow shows the satellite peak. (left) and the variation of the maximum strain with increasing dose (right).

300 °C implantations

Figure 3.17 shows the results obtained for 300 °C implantations. Up to a fluence of 2.4 x 10^{14} Xe.cm^{-2}, the curves show interference patterns indicating that the amorphous state is not reached. The variations of the maximal elastic strain are no more linear in the whole range of studied doses. After a period of increasing, it levels off toward a saturation value. These variations $\varepsilon_{max}(\emptyset)$ can thus be fitted according to:

$$\varepsilon_{max}(\emptyset) = \varepsilon_{max}^{sat}(\infty)\left[1 - exp\left(-\sigma_{eff}.\emptyset\right)\right] \qquad \textbf{(Eq. 3.5)}$$

where $\varepsilon_{max}^{sat}(\infty)$ is the maximal strain at saturation and σ_{eff} the effective cross section for elastic strain accumulation. A good fit is obtained by taking $\varepsilon_{max}^{sat}(300\,°C) \sim 2\,\%$ and $\sigma_{eff}(300\,°C) \sim 3\ dpa^{-1}$ (see the dotted "pink" line in figure 3.17).

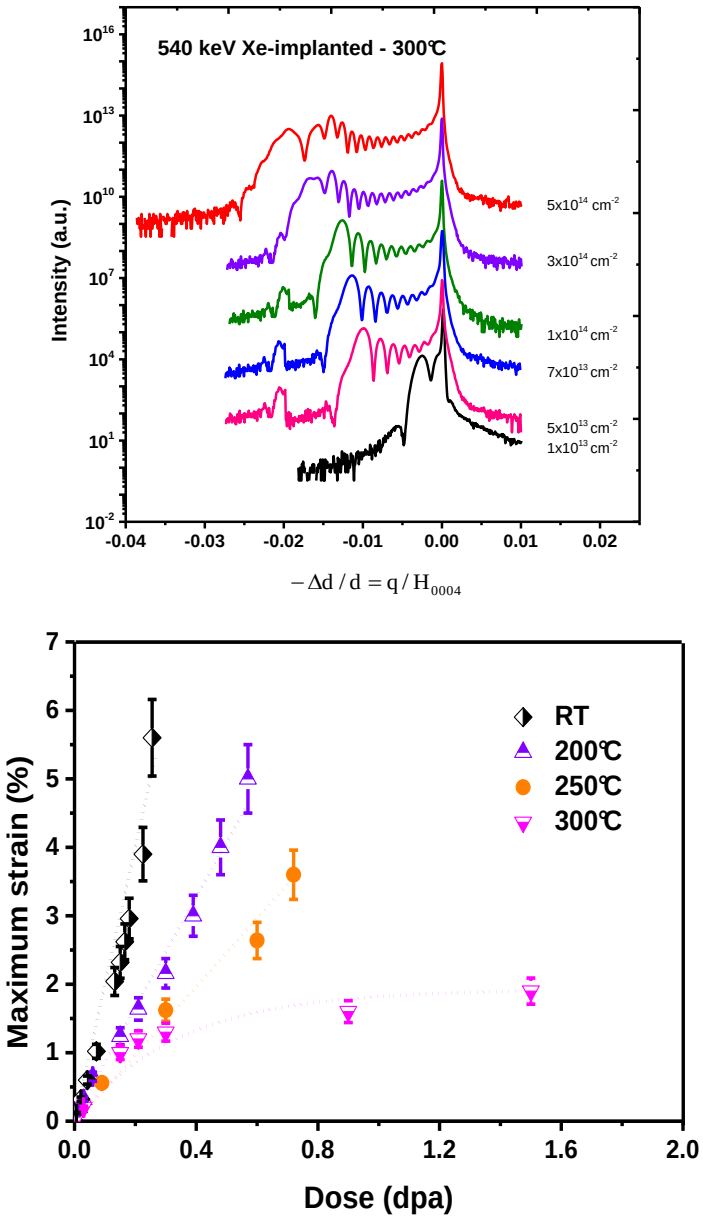


Figure 3.17: XRD curves for Xe-implanted 4H-SiC at 300 °C (top) and the variation of the maximal strain with dose (bottom)

At low doses, Eq. 3.6 is linear given thus:

$$\sigma_{app}^{T} = \varepsilon_{max}^{sat}(T).\sigma_{eff} \qquad \textbf{(Eq. 3.6)}$$

So, at low doses for 300 °C implantation, we obtain $\sigma_{app}^{300°C} \sim 6\ \%.dpa^{-1}$ similar to the 250 °C implantations.

Again, the satellite peak appears at $3x10^{14}$ cm^{-2} and then stays at the same position around 1.4% with increasing fluence. XRD simulations were thus carried out at this temperature of implantation to understand or to get more information on the strain profile and in particular to understand the origin of the satellite appearing at high fluence. In a first step, we used the program of Stepanov (chapter 2). To confirm the results, data were sent to A. Boulle (Limoges) who developed a specific program for the strain determination of implanted materials. Both simulations gave similar results; only those obtained by A. Boulle are presented. Figure 3.18 shows the fits obtained of the XRD curves and the corresponding profiles of strains. The fringe patterns, as well as the intensity, are well fitted. All the as-obtained strain profiles present a similar shape roughly described by a broad Gaussian-like curve. As expected the maximal strain increases with increasing fluence. We note however that the maximal strain shifts toward the bulk with increasing fluence and that the profile spreads out up to 350 nm approximately at the highest fluence. We also can note that for the two highest fluences for which singularities were observed in the XRD curves, that the near surface strain underwent a modification to tend toward a bi-modal distribution. This strain accumulation appearing in the near surface region with dose suggests different zones of damage accumulation (2 zones).

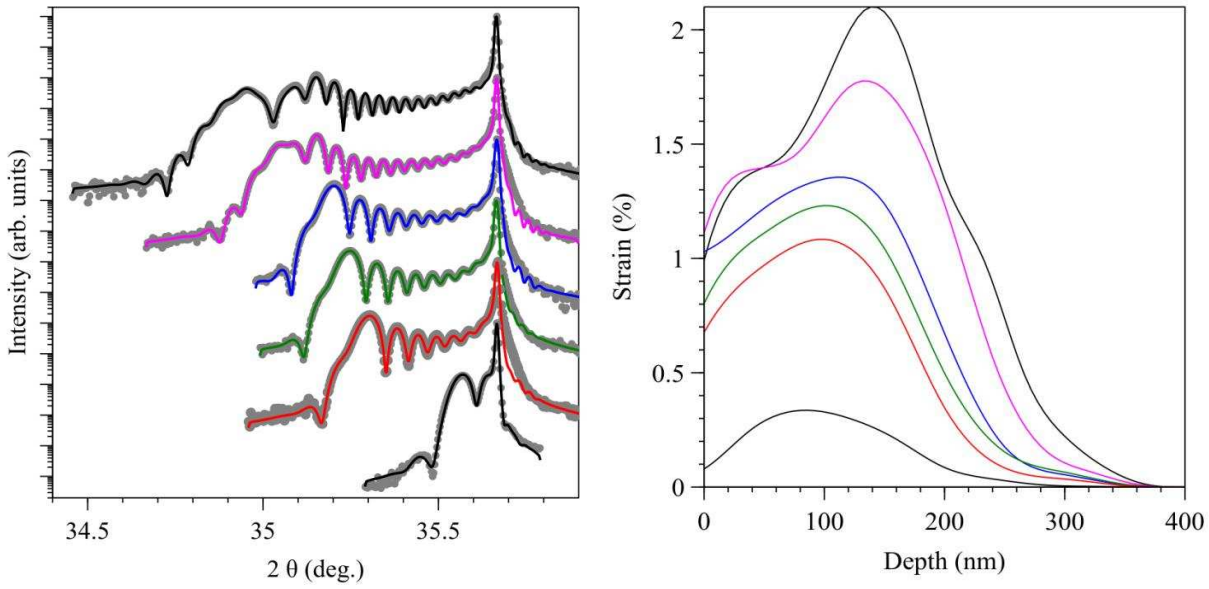


Figure 3.18: Simulation result of the XRD curves for Xe-implanted 4H-SiC at 300 °C with fluence from 1 x 10^{13} to 5 x 10^{14} cm^{-2} (left), the as-deduced variation of the maximal strain with dose (right).

3.2.3 Discussion on the low-temperature regime of implantation

Damage buildup in Xe-implanted SiC was studied in the low-temperature regime (T_{impl} 300 °C) by combining different techniques. The following table 3.2 summarizes the main characteristics observed in this study.

T (°C)	σ_{app}(%.dpa^{-1})	$\emptyset_c$ (Xe.cm^{-2})	$\emptyset_c$ (dpa)	$\emptyset_{amorp}$ (Xe.cm^{-2})	$\emptyset_{amorp}$ (dpa)
RT	20	No satellite peak		0.85 - 1.45 x 10^{14}	0.26 - 0.44
200	8 - 9	1 - 1.3 x 10^{14}	0.3 - 0.39	1.6 - 1.9 x 10^{14}	0.46 - 0.57
250	4 - 5	2 - 2.4 x 10^{14}	0.6 - 0.72	2.4 - 2.8 x 10^{14}	0.72 - 0.84
300	4 - 5*	1 - 3 x 10^{14}	0.3 - 0.9	No amorphization	

Table 3.2: Parameters of Xe-implanted SiC at different temperatures for 540 keV: σ_{app} is the apparent cross-section for strain buildup, $\emptyset_c$ the fluence or dose at which the satellite peak appears and $\emptyset_{amorp}$ the fluence or dose for amorphization.

In the low-temperature regime, i.e. for temperatures lower than 300 °C, the dose for amorphization increases (or the apparent cross-section for defect stimulated amorphization decreases) with temperature suggesting an increased efficiency of simultaneous dynamic recovery during implantation. Supposing that the irradiation-induced recovery process is dominant a relationship between the temperature and dose required for complete amorphization has been proposed by Weber et al. [33, 36, 72, 73]. This equation, given for a constant ion flux, can be written as:

$$\emptyset_{amorp} = \frac{\emptyset_0}{1 - K.e^{\frac{-E_a}{kT}}} \qquad \textbf{(Eq. 3.7)}$$

where $\emptyset_0$ is the dose for complete amorphization at 0 K, $K = 1/\sigma_{app}.\emptyset_{amorp}$ is a constant and E_a the activation energy. It is difficult to obtain an accurate value of K from table 3.2 due to the indetermination of the amorphization threshold as well as the insufficient data. However, the critical temperature T_c above which amorphization does not occur can be well defined in the range 250 – 300 °C (from XRD experiments, figure 3.16 and 3.17). This temperature T_c can be defined by Eq. 3.8 for $\emptyset_{amorh} \rightarrow \infty$, giving:

$$T_c = \frac{E_a}{k}.\frac{1}{\ln(\frac{1}{\sigma_{app}.\emptyset})} \qquad \textbf{(Eq. 3.8)}$$

So, by taking an extrapolated amorphization dose $\emptyset_0 \sim 0.32$ dpa the energy activation, E_a, for dynamic recovery processes has been estimated to be 0.11 ± 0.02 eV, in good agreement with the value of 0.12 eV ± 0.01eV found in 1.5 MeV Xe^+ 6H-SiC [74]. The low activation energy may reflect the almost athermal nature of the irradiation-assisted process. Figure 3.19 shows the temperature dependence of the critical dose for complete amorphization; data were fitted by using Eq. 3.8 and are compared with those obtained for 1.5 MeV Xe^+ ions in 6H-SiC [74]. Even if the kinetic processes controlling the amorphous transformation are more complex than the single-activated process described by the Eq. 3.7 both curves fit rather well the data.

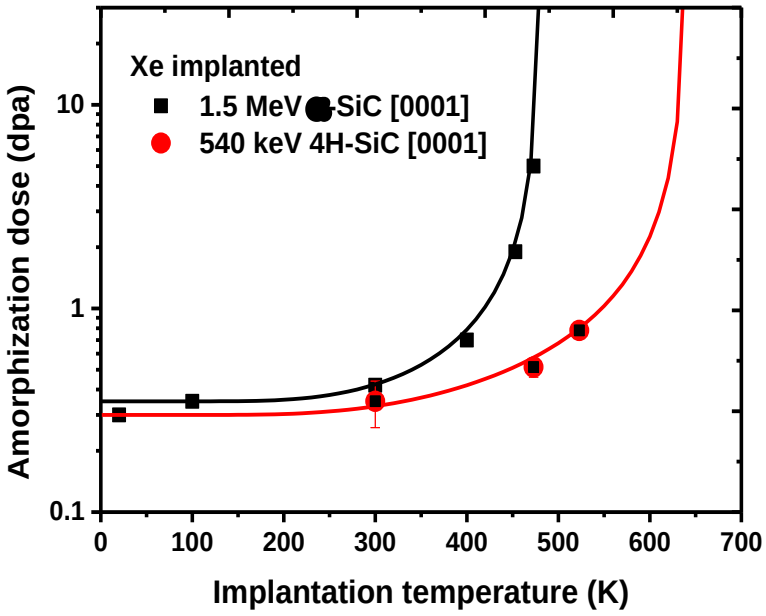


Figure 3.19: Fits of the temperature dependence of the critical dose for amorphization by using Eq. 3.4 to our data (red line) and in 6H-SiC [31].

The shift in T_c mainly comes from the values of K, i.e, is associated with the damage cross-section and ion flux. As previously stated the process of amorphization of SiC by ion bombardment is different of Si; it is only related to the energy deposited in elastic collision and secondary effects are negligible [75]. Moreover, there is an increased efficiently or simultaneous damage recovery with decreasing particles mass [36]. At RT, it has also been shown in helium implantation that the energy of implantation also plays a major role in the amorphization [32]; a higher concentration of defects is required with increasing energy (from keV to MeV). Eq. 3.7 is valid for complete amorphization, but the formation of amorphous pockets (or very disordered zones) can take place for lower doses. In this way isolated tiny amorphous zones of 1 nm in diameter are reported in 6H-SiC implanted with 420 keV – 10^{11} Xe.cm^{-2}, so for µdpa [76]. On the contrary [36] suggests that amorphization of SiC may occur homogeneously, i.e., not directly in cascades (HRTEM picture only reveals a mottled contrast at 0.16 dpa). In this work nano-size isolated amorphous zones were also observed beyond the amorphous buried layer, see figure 3.19, i.e, in a zone of dpa close to 0.2. The real picture of the amorphous transition is still complex.

The shift of the maximum damage peak has also been reported by RBS measurements in 6H-SiC samples implanted at 600 °C with a high fluence of Si^+ ions [34]. This shift in depth increases with temperature and dose, and is ascribed to an increase in the average of the diffusion length of the defect with implantation temperature. The simulation of the XRD curves shows that for xenon implantation 2 different zones of damage accumulation could be distinguish leading to a bi-modal distribution of strain. These last points will be discussed later in the highlight of TEM results obtained after annealing. This effect is not observed for RT implantation. At 300 °C amorphization will not occur: saturation is strain is reported: the production rate of defects tends to become equal to the recovery rate.

3.3 Damage buildup for implantations at 400 °C

This part is devoted to implantations conducted at 400 °C in a wide range of fluences ranging from 1 x 10^{13} to 1 x 10^{16} cm^{-2}, referring to doses from 0.03 to 30 dpa. For clarity, it is separated into three different subsections. Results obtained up to doses lower than 4 dpa are firstly presented and analyzed mainly through XRD measurements. Then results for severe dose (30 dpa) are detailed especially with the help of TEM observations. The last sub-paragraph is devoted to their evolution upon subsequent annealing (up to 1400 °C) including the swelling measurements.

3.3.1 Low and medium dose regimes (< 6dpa)

In this regime (medium dose and temperature), the evolution of the maximal strain was studied through the XRD curves. The XRD curves are displays in figure 3.20. All the curves show a similar shape, and again the position of the last fringe represents the maximum of the elastic strain.

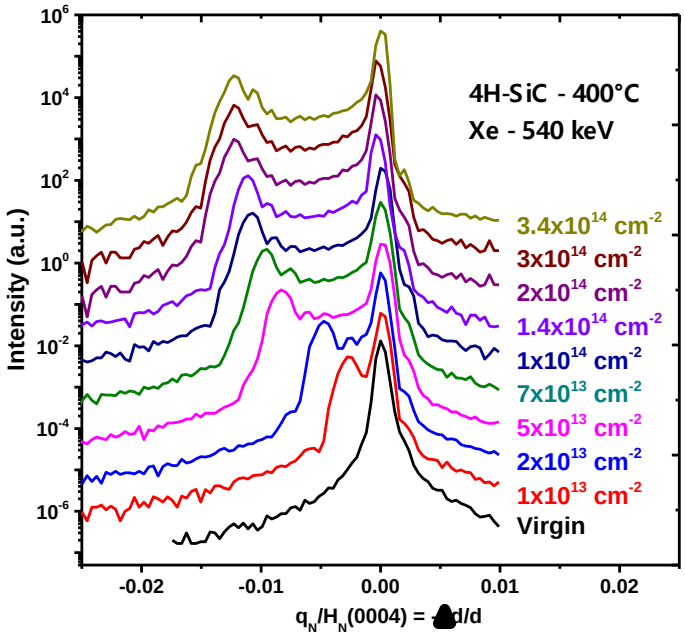


Figure 3.20: X-ray scattered intensity distributed along the normal surface direction close to the (0004) reflection, of 400 °C Xe-implanted 4H-SiC with fluences ranging from 1 x 10^{13} (0.03 dpa) to3 x 10^{14} cm^{-2} (1 dpa).

It may be noted that the strain evolves with fluence and then has tended to level off. This trend clearly appears in figure 3.21. For comparison, the variations obtained for the 300 °C implantation are also plotted. The only difference between the two temperatures of implantation arises from the saturation level which decreases with increasing temperature $\varepsilon_{max}^{sat}(300\,°C) \sim 2\,\% > \varepsilon_{max}^{sat}(400\,°C) \sim 1.3\,\%$. The curves are well fitted according to Eq. 3.5 (dotted lines). We can note that the effective cross section is taken roughly constant of about $\sigma_{eff.} = 6 \pm 2\ dpa^{-1}$ as obtained at 300 °C.

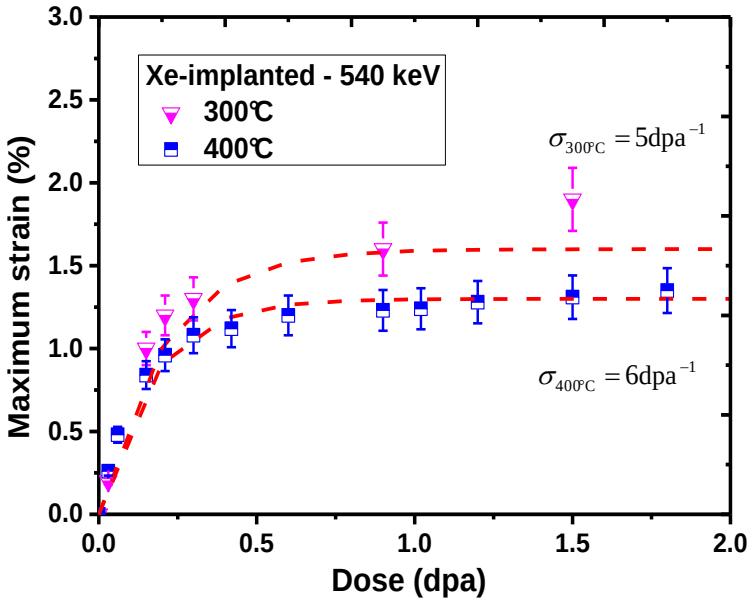


Figure 3.21: Evolution of the maximal elastic strain as function of dose (dpa) in Xe ions implanted at 400 °C (estimation of error of 10 %). For comparison data obtained at 300 °C are also reported. The dotted lines are simulations by using Eq. 3.5.

Comparison with implantation of other noble gases

In this low dpa regime, the effects of implantation were compared according to the mass of the noble gas (He, Ne, Ar, Xe). The conditions of implantation were chosen to obtain a similar dpa profile with the help of SRIM simulations. To obtain a similar profile with light gas the incident energy must be reduced (22 keV for helium ions). However, it was not possible to perform implantation at energies lower than 30 keV. So, since a lot of results were previously obtained at 160 keV we decided to keep this incident energy for helium, giving rise to a projected range for helium ions around 590nm with a longitudinal straggling of 80nm. Anyway, only a few differences are reported with the helium behavior in SiC according to the energy of implantation, from keV to MeV (Ph.D. S. Leclerc [49]). Table 3.3 summarizes the conditions of implantation according to NG. As seen according to the ion mass the number of vacancies generated by one incident ion increases with mass (50 times more for Xe than for He ions). All the implanted gas atoms are supposed to be trapped by vacancy-type defects induced by the ion implantation process, see section 3.1 for Xe atoms and in [50] for helium.

Ion	He	Ne	Ar	Xe
Energy (keV)	160	110	210	540
Fluence (0.6dpa)	1.5 x 10^{16} cm^{-2}	1.35 x 10^{15} cm^{-2}	6.2 x 10^{14} cm^{-2}	2 x 10^{14} cm^{-2}
Vacancies/ion	90	659	1303	4319
Concentration %	1.13	0.13	0.07	0.02

Table 3.3: Conditions of implantation at 400 °C - 0.6 dpa for different noble gases (SRIM calculations)

Figure 3.22 shows the damage profiles of the different ions are for a maximal value of 0.6 dpa (the corresponding fluences are given in table 3.3). As expected the damage profile is similar for Xe, Ar and Ne implanted atoms (R_D ~ 100nm). On the contrary helium ions implanted at 160 keV leads to a damage profile roughly constant over a wide depth, up to 300 nm (~0.1 dpa for 1.5 x 10^{16} $He^+.cm^{-2}$) and then shows a negative skewed Gaussian behavior. The associated XRD curves are also reported and compared. For a dose of 0.6 dpa it is clear the maximal strain does not depend on the gas itself (1.2-1.3 % for all the ions). For similar damage profiles (Xe, Ar, and Ne) the XRD curves well overlap. For a different damage profile, He implantation at 160 keV, an asymmetric broadened satellite peak appears also at the left of the main Bragg peak $(\Delta d/d)_N$ ~ 0.5%) and spreads toward the low angle side. Previous studies showed that this peak is ascribed to the near surface region and that the scattered intensity then provides from the most damaged zone [55]. This behavior suggests that the damage mainly results from ballistic effects and that the NG contribution to the elastic strain is negligible (c_{at} ~ 0.006 % for Xe and 0.7 % for He at the maximum for a dose of 0.6 dpa).

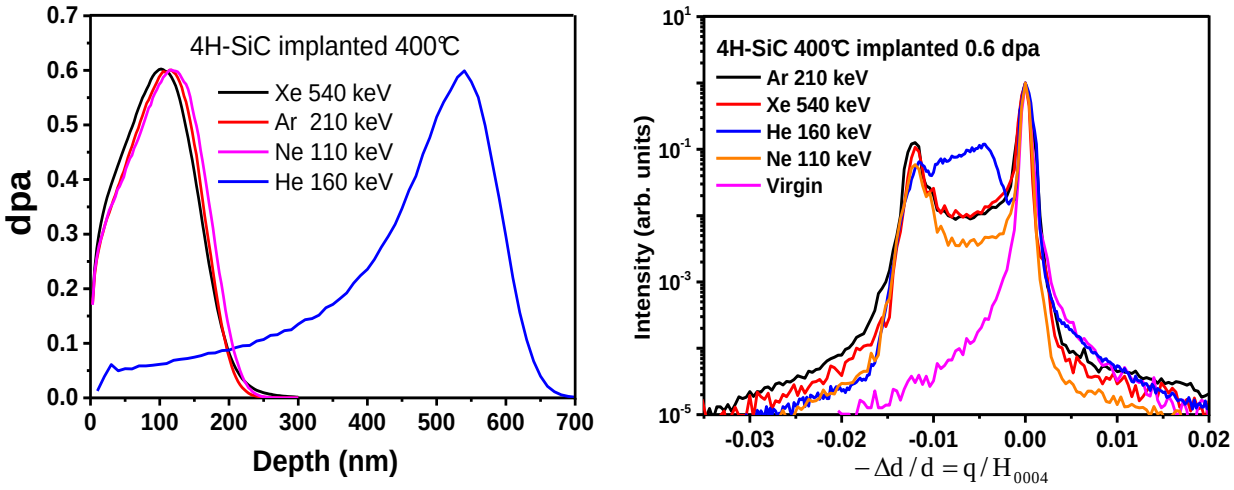


Figure 3.22: (left) Damage profiles for 540 keV- 2 x 10^{14} $Xe.cm^{-2}$, 210 keV - 6.2 x 10^{14} $Ar.cm^{-2}$, 110 keV – 1.35 x 10^{15} $Ne.cm^{-2}$ and 160 keV-1.5 x 10^{16} $He.cm^{-2}$ implantations in 4H-SiC; (right) the corresponding X-ray scattered intensity distributions along the normal direction close to the (0004) refection to a given dose of 0.6 dpa at the maximum in 4H-SiC implanted at 673 K.

Figure 3.23 plots the variations of the $\varepsilon_{max}(\%)$ versus dose (dpa) for the different incident ions implanted at 400 °C. For comparison results obtained at RT are also plotted. For RT implantations the variations of $\varepsilon_{max}(\%)$ with dpa are linear whatever the ion mass may (He and Xe) giving rise to an apparent cross section (Eq. 3.3) of 18 ± 2 $\%.dpa^{-1}$. On the contrary at 400 °C curves diverge from a critical dose of about 0.6 dpa for helium implantation: a second step of strain buildup clearly appears. But surprisingly no differences are observed for the other noble gases (Xe, Ar and Ne). Helium atoms are thus supposed to behave differently. This difference in strain buildup can be related to the concentration of implanted gas (for a given dose of about 75 times less atoms of Xe are implanted in comparison to helium, and of about 10 times less for Ne).

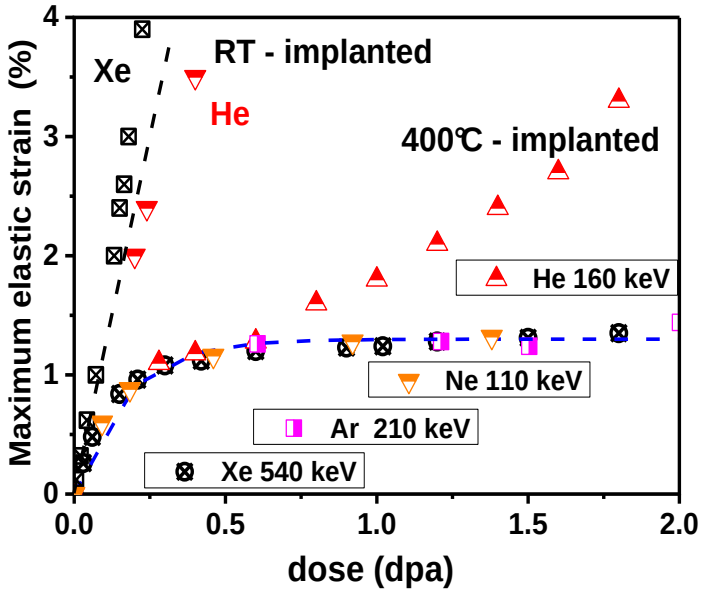


Figure 3.23: Evolution of the maximal elastic strain as a function of dose (dpa) until 2 dpa, implantation of Xe-540 keV and He-160 keV at RT, implantation at 400 °C.

TEM observations were then carried out at a dose range of 1.5-2 dpa (where curves are different), to compare the as-introduced damage for He and Xe atoms. Figure 3.24 shows the TEM images taken at a similar level of damage.

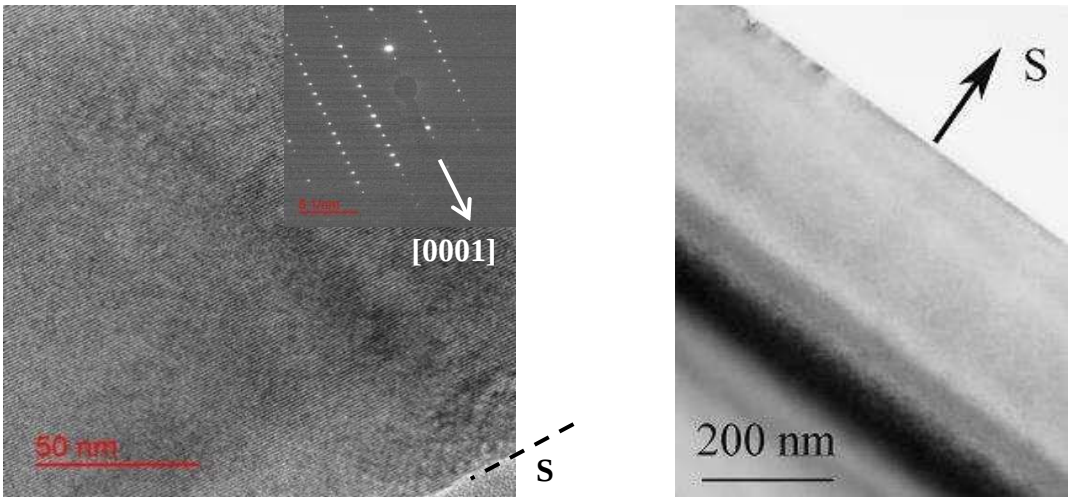


Figure 3.24: XTEM images of 400°C implanted SiC with 1.5 dpa of Xe (left) and 2 dpa with He (right). c_{max}^{Xe}~0.06% ≪ c_{max}^{He}~3.8 %.

The TEM images, figure 3.24, support this different behavior; it is difficult or impossible to distinguish any damage due to the implantation of xenon (1.5 dpa) while with implantation of helium (2 dpa) a wide band of dark contrast is observed close to the maximal of deposited energy (570 nm). The NG seems to have a stabilizing effect on the damage induced by the incident ions reducing thus the dynamic recombination. This effect could be also heightened by the differences in mobility.

Model of the strain buildup

As written in chapter 1 different phenomenological models of damage accumulation are used according to irradiation conditions in ceramics to describe the amorphous transition. Models are related to the amorphous fraction measured by ion channeling techniques detecting the presence of defects along the channeling axis (the RBS technique is relatively insensitive to vacancies and antisites) whereas XRD is more sensitive to investigate any variation of the structure as the lattice strain. Nevertheless, the models developed to understand the variation of the amorphous fraction according to dose have formed the basis of our simulations. Results at 400 °C suggest that the strain progressively accumulates in two regimes or two steps according to the dose. This second step is clearly evidenced for helium (see figure 3.23) but does not clearly appear for the other NG. Experiments were thus being carried out at higher doses up to 6 dpa, see figures 3.25 and 3.26.

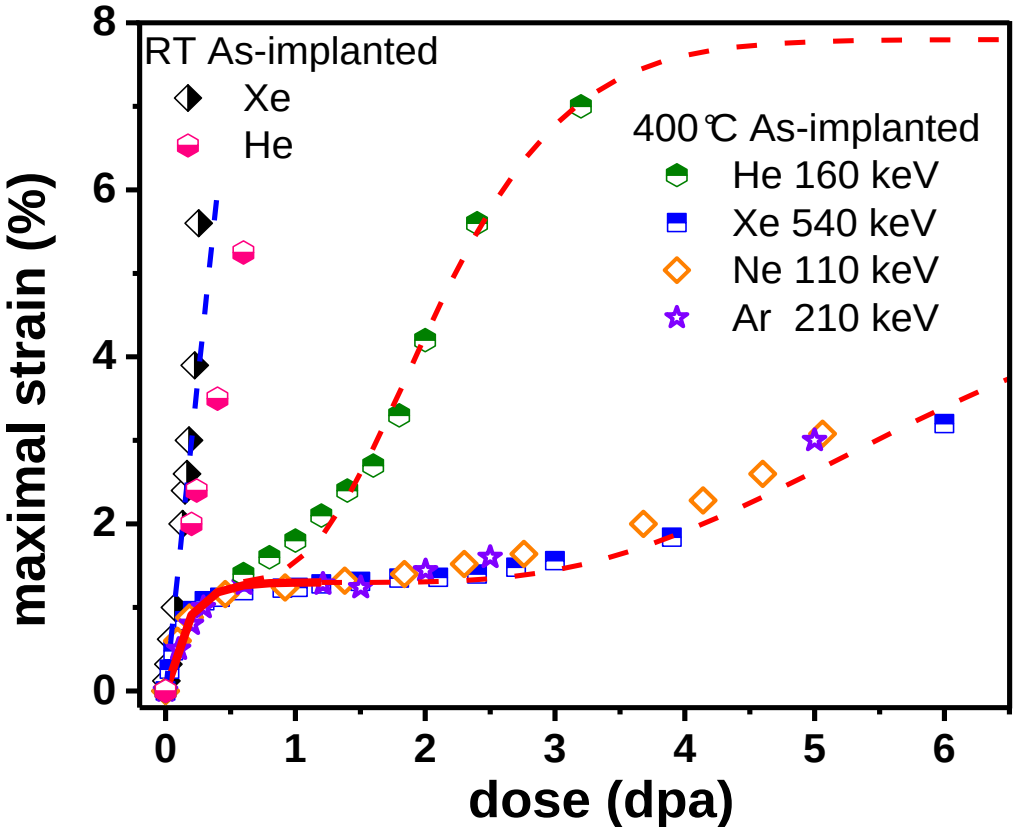


Figure 3.25: Evolution of the maximal strain $\varepsilon_{max}(\%)$ with dose in NG implanted SiC at RT and 400 °C. The dotted lines are fits according to Eq. 3.9.with following parameters:

σ_{eff}^{NG}	$= 6\ dpa^{-1}$	$\varepsilon_{max}^{sat}(400\ °C) = 1.3\ \%$	
σ_{eff}^{He}	$= 3\ dpa^{-1}$	$\varepsilon_{max}^{sat}(He) = 6.5\ \%$	with n = 3
$\sigma_{eff}^{Xe,Ar,Ne}$	$= 1\ dpa^{-1}$	$\varepsilon\ _{max}^{sat}(Xe, Ar, Ne) = 4\ \%$	with n = 5

For doses larger than 2 dpa we can note a slight increase of the maximal strain with dose, suggesting the occurrence of a new (or second) process in the damage accumulation. According to molecular dynamic simulation made on 3C-SiC [77] energetically ions primarily produce interstitials,

monovacancies, antisite defects and small defect clusters within cascades. The first step of strain accumulation is thus related to the creation of such primary defects, via a direct impact mechanism described by the Eq. 3.5 which at low doses is approximated by a straight line (as observed, Eq. 3.6). The second step occurs at higher doses and seems to depend on the number of incident ions, so seems to be related to the probability that an incident ion hits a partially damaged region as already proposed by Gibbons for overlapping of collision cascades. Figure 3.25 shows the plot of strain as well as the fitted curves (dotted lines) according to Eq. 3.9 with the following parameters. The strain buildup determined through XRD measurements is described by the following equation Eq. 3.9 derived from a modified Gibbons model [39]:

$$\varepsilon_{max}(T) = \varepsilon_{max}^{sat1}(T)\left[1 - e^{-\sigma_{eff}^{1}.\emptyset}\right] + h(\emptyset - \emptyset_c)\varepsilon_{max}^{sat2}(T)\left[1 - \sum_{k=0}^{n-1}\frac{\left(\sigma_{eff}^{2}.\emptyset\right)^{k} e^{-\sigma_{eff}^{2}.\emptyset}}{k!}\right] \quad \textbf{(Eq. 3.9)}$$

Where h(x) is the Heaviside function [h(x) = 0 for x < 0 and h(x) = 1 for x > 0], and n is the number of overlapping cascades required to produce elastic strain. It should be noted that in case of direct-hit strain, that is, strain buildup occurs within a single cascade (no overlap), Eq. 3.9 reduces to Eq. 3.5. At very low dose Eq. 3.5 is also reduced to Eq. 3.6. Fitting parameters are summarized in Table 3.4 and in figure 3.25.

Ion	$\varepsilon_{max}^{sat\,1}$	σ_{eff}^{1}	$\emptyset_c$	σ_{eff}^{2}	$\varepsilon_{max}^{sat\,2}$	n
He	1.25 ± 0.5	6 ± 2	0.5 ± 0.1	3 ± 1	7 ± 1	3 - 5
Ne, Ar, Xe			1.3 ± 0.3	1 ± 0.5	4.5 ± 2	5 - 7

Table 3.4: Parameters used in the strain build-up model, described in the text (Eq.3.9).

As seen, despite its simplicity our model (Eq. 3.6) provides an excellent fit at this temperature of 400 °C (and at RT due to the low implanted doses). Importantly, these fitting can exhibit dependencies on temperature as observed for the value at saturation $\varepsilon_{max}(T)$. Previous results obtained in helium implanted SiC in a large range of temperature showed that the efficient cross section are not (or few) dependent on temperature underlining the intrinsic nature of the as-created strain-related defects or the specific defect interaction processes [59]. The similarity between the effective cross section $\sigma_{eff}^{1,2}$ in step 1 and 2 infers more for a change of process (from direct impact to

cascade overlap) for strain buildup rather than for another type of defects. Thus, point defects or clusters of defects are supposed to be created or accumulated with dose. In all the previous amorphization models, as for example the MSDA model, the cross sections of each step were found to be different: higher values of σ_{eff}^2 mean that the volume transformed by each incident ion in the second step (formation of amorphous zones) is much larger than in step 1 for which interstitials clusters are supposed to be created ($\sigma_{eff}^2/\sigma_{eff}^1$~100) in [28]. The non-(or few-) dependence of $\emptyset_c$with the ion mass (except helium) suggests or points out the importance of NG-defects interaction (NG-vacancy complexes for example, see section 3.1) rather than a damage accumulation efficiency on the defect generation rate.

3.3.2 High dose regime (6 to 30 dpa)

Figure 3.26 shows that in the high fluence regime the shape of XRD curves evolves; a drop in the diffracted intensity is clearly observed, there is much less more coherent diffracting volume. At 6 dpa (2 x 10^{15} Xe.cm^{-2}) the shape of the curve changes, the maximal strain can, however, be estimated to 3.2 % while with increasing dose 15 and 30 dpa (1 x 10^{16} Xe.cm^{-2}) it is impossible.

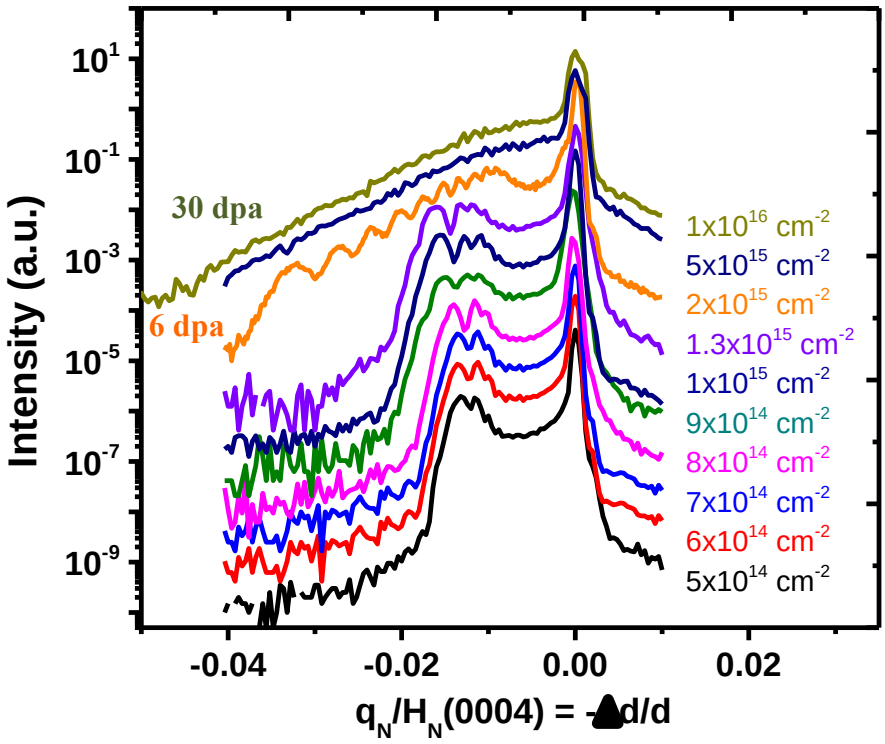


Figure 3.26: X-ray scattered intensity in 400 °C Xe-implanted 4H-SiC with fluences ranging from 5 x 10^{14} (1.5 dpa) to 1 x 10^{16} cm^{-2} (30 dpa).

XTEM observations were thus carried out on the 30 dpa implanted SiC at 400 °C to study the as-damaged zone. Figure 3.27 summarizes the observations. Figure 3.27a shows that the highly damaged zone is still crystalline. It is 150 nm wide and made of small clusters of dark contrast not individually resolvable, figure 3.27b. This damaged zone is not centered on the nuclear energy loss

profile but rather on the xenon distribution (calculated by SRIM). This is confirmed by the HAADF-STEM image, figure 3.27c, showing that the ion distribution is in good agreement with SRIM simulations: there is thus no noticeable diffusion of xenon under implantation at 400 °C. Figure 3.27d highlights the strong correlation between TEM visible defects and the presence of xenon. The interaction between Xe-atoms and defects is thus efficient as suggested in the previous paragraph. This is also clearly evidenced by the lack of TEM-visible defect in the near surface region in which the nuclear energy loss is maximal. RBS experiments conducted at the CSNSM-Orsay (A. Debelle) are in agreement with the TEM observations; no diffusion of xenon under irradiation (red-steps in figure 3.27) and a deformed fraction close to f ~ 0.3 in the near surface region (figure 3.28). RBS suggests also that the damage zone extends up to a depth of 300 nm. It is also interesting to note that the damage fraction is 1, so close to the amorphization whereas TEM observation shows that it is still crystalline.

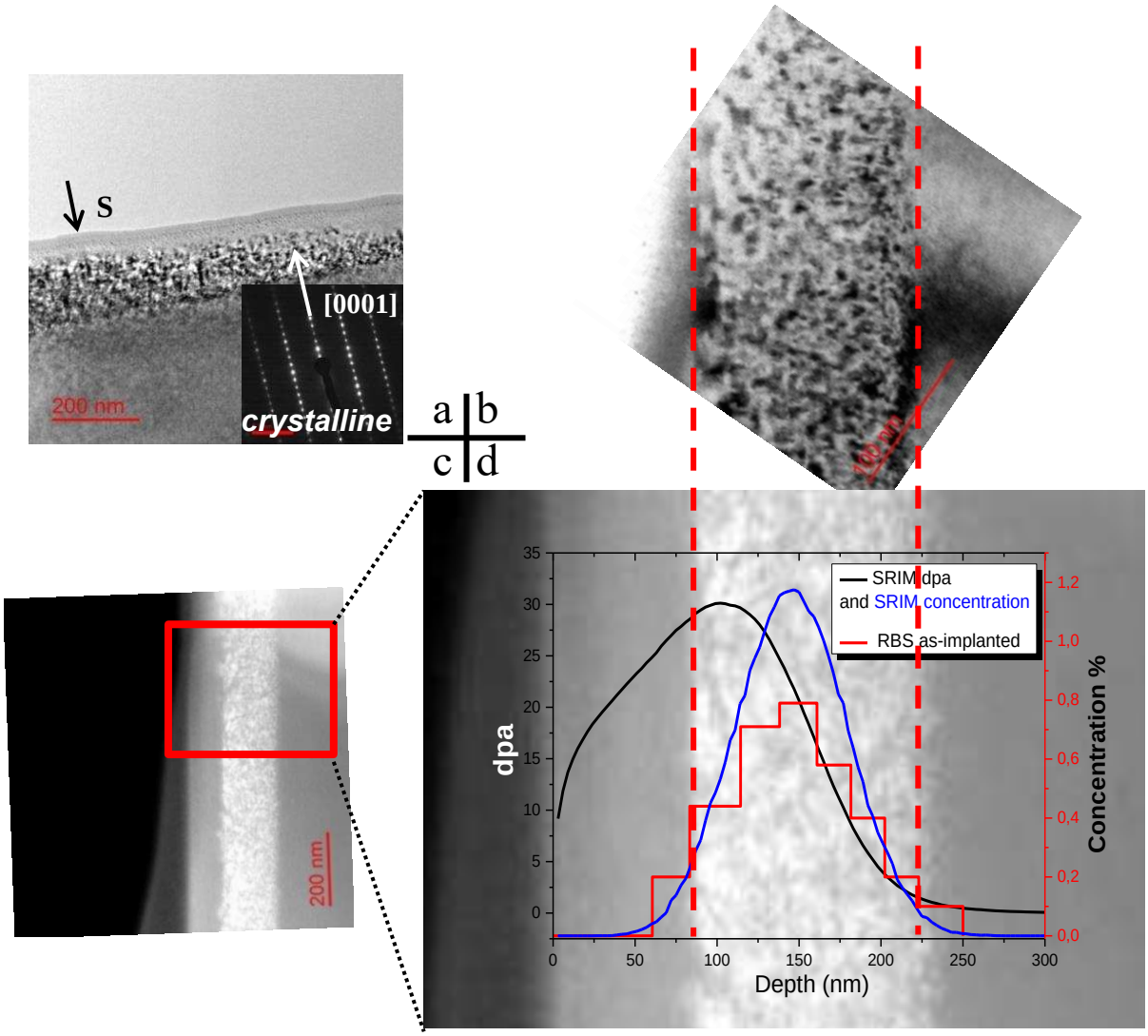


Figure 3.27: XTEM experiments on 30 dpa Xe-implanted SiC at 400 °C. (a) and (b) bright field images, (c) and (d) STEM-HAADF, general views – comparison with SIRM simulations and the Xe-profile determined by RBS/C (red curve).

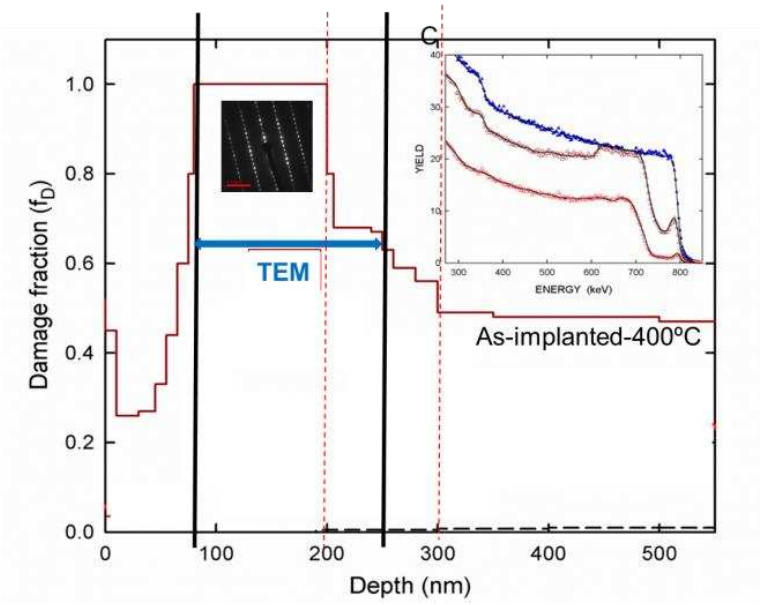


Figure 3.28: RBS experiments and analysis (damage fraction) on Xe implanted SiC at 400 °C for 30 dpa.

Experiments/analyses (A. Debelle and A. Thomé : CSNSM Orsay)

3.3.3 Discussion on the damage buildup at 400°C implantation

According to our observations, the implantation-induced strain buildup can be divided into three main regimes versus dose, independently of incident ions:

- A linear strain accumulation regime in which the dynamic recombination is limited. At lower temperature of implantation, this leads to amorphization. Each incident ion takes part to the strain according to its efficiency. Ballistic effects are dominant.
- A regime of saturation where the dynamic recombination is preponderant. The direct impact model is sufficient to explain the saturation of strain again independent of the incident ions.
- A regime of strain buildup acceleration in which the number of atoms as well as their interaction for the as-introduced defects become preponderant. The NG atoms operate as defect stabilizers inhibiting the recombination. The occurrence of this regime is thus strongly dependent of the amount of gas as well as their interaction with defects that could be very different [78].

The similarity between the effective cross-sections of the three regimes suggests that similar defects are produced with the dose. Their small values also suggest that point defects or small clusters of defects are involved all along the process of accumulation. The proposed model derived from Gibbon's equation fits relatively well the damage buildup.

The TEM observations and RBS analysis combined with the XRD simulations done on the 300°C implanted sample (previous section) show that the strain/damage buildup could be divided into three different zones. A highly damaged zone around the mean projected range of the Xe-atoms is surrounded by a near-surface region highly deformed but containing no visible defects and by a defect-tail deeper. TEM visible defects formed from a damage fraction above 0.6.

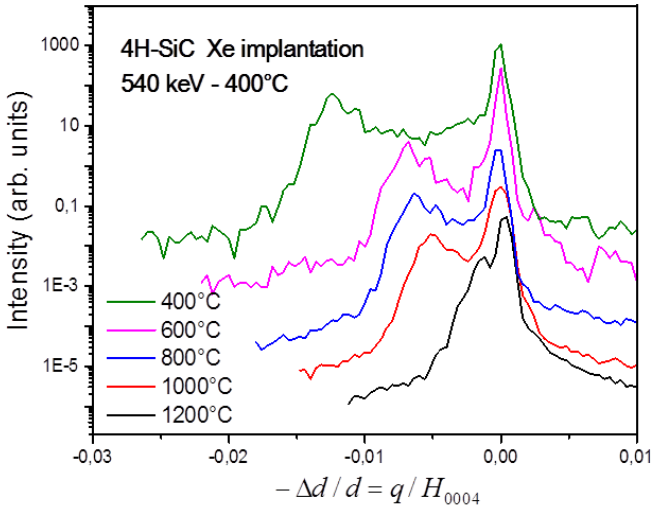
3.4 Evolution upon subsequent annealing

All the 4H-SiC samples were implanted at 400 °C and then annealed in the lamp oven (chapter 2). The evolution upon annealing was studied for the following doses: 1 dpa (named low dose regime), 3 dpa and 6 dpa (medium regime), and 15 dpa (high dose regime). The annealing temperatures were set at 600, 800, 1000, 1200 and 1400 °C.

3.4.1 Low dose: 1 dpa

Strain recovery at low dose (1dpa)

The low dose of 1dpa corresponds to a fluence of 3.4 x 10^{14} Xe.cm^{-2}. Figure 3.29 shows the evolution of XRD curves with increasing annealing temperature. The XRD patterns show the peak of maximum strain approaches to the Bragg peak. This means the maximum strain decreases with annealing temperature from 1.24 % (400 °C) to 0.16 % (1200 °C). The strain relaxation occurs for all the annealing temperatures up to 1200 °C.



Annealing temperature	Maximum strain %
As-implanted 400 ºC	1.24
600 ºC	0.76
800 ºC	0.64
1000 ºC	0.48
1200 ºC	0.16

Figure 3.29: Evolution upon annealing of XRD curves in the as-implanted SiC at 400 °C with fluence 3.4 x 10^{14} cm^{-2} (1 dpa).

All of the experimental points obtained after annealing for 4 or 30 minutes and by using single or multi annealing procedures are plotted in figure 3.30. The relaxation strain was fitted by using an Arrhenius law. Two stages of strain relaxation are distinguished. The first stage takes place for temperatures in the range 600 - 1000 °C. In this stage, the strain relaxes progressively upon thermal annealing with an activation energy of E_a = 0.1 ± 0.02 eV. With increasing annealing temperature, a second stage can be identified, from ~ 1000 to 1200 °C. The activation energy for this stage is modified to 0.9 ± 0.1eV. This change in activation energy with temperature suggests that another mechanism of recovery takes place above a critical temperature close to 1000 °C.

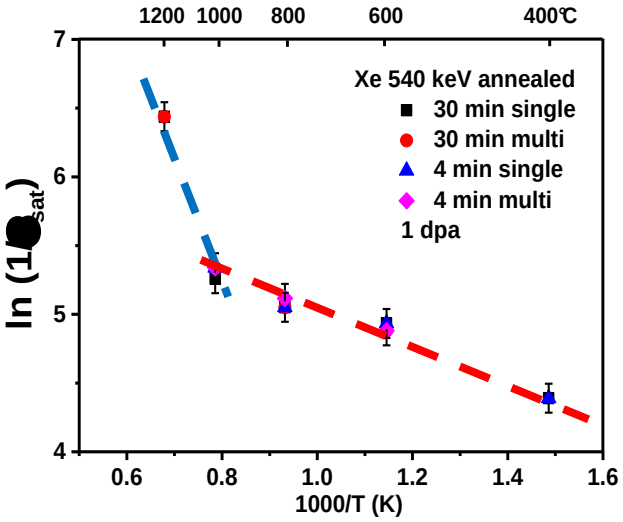
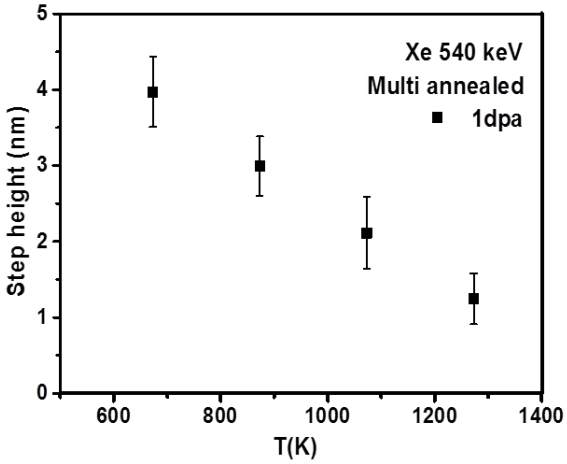


Figure 3.30: Evolution (Arrhenius plot) of strain recovery according to the increasing annealing temperature for Xe 1 dpa as-implanted at 400 °C.

Swelling measurement (1dpa)

The evolution of step height with increasing annealing temperature is plotted in figure 3.31. The associated table reports the values as well as the swelling calculated by Eq. 3.10.

$$\text{Swelling (\%)} = \frac{Step\ Height}{damage\ layer}.100 \qquad \textbf{(Eq. 3.10)}$$



Annealing temperature	Step height (nm)	Swelling (%)
As-implanted 400 ºC	4.0 ± 0.5	2.0 ± 0.25
600 ºC	3.0 ± 0.4	1.5 ± 0.2
800 ºC	2.1 ± 0.5	1.1 ± 0.3
1000 ºC	1.3 ± 0.3	0.6 ± 0.2

Figure 3.31: Evolution of the step height in low dose (1dpa) 400 °C-implanted SiC with annealing temperature. The table shows the step height with an estimation of standard deviation and swelling. The step height at 1200 °C was too small to be determined (< 1 nm).

With annealing temperature, the step height is reduced from 4 nm at 400 °C to 1.3 nm at 1000 °C. The reduction of the step height seems to vary linearly with increasing temperature. With increasing thermal annealing temperature higher than 1000 °C, the step height cannot be measured by the interferometry method. It is supposed that the step height descends to lower than 1nm.

Strain recovery compared with step height

For comparison, the step height evolution upon temperature annealing was also fitted with an Arrhenius law and compared with the strain recovery, see figure 3.31. As seen the slope E_a = 0.12 ± 0.01 which corresponds to the first stage of recovery, is very close to the one of strain recovery suggesting that both evolutions are strongly associated. If we suppose that a second stage occurs at higher temperatures (see the dotted blue line on top in figure 3.32) temperature of annealing of 1200 °C would lead to a step height lower than 0.5 nm; the interferometry technique has not the capacity to measure this height.

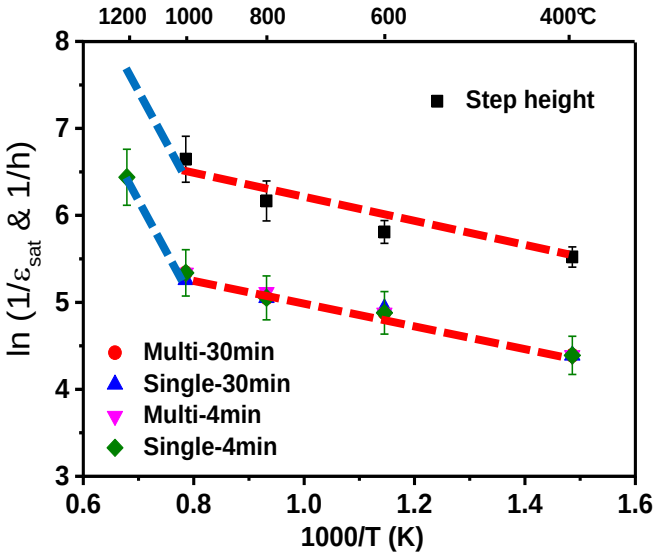


Figure 3.32: Evolution of strain recovery and step heights (fitted with a red dotted line for 400 - 1000 °C and blue dotted after 1000 °C) according to the increasing annealing temperature for the 1 dpa implanted SiC at 400 °C. Fits were done assuming an Arrhenius law and assuming 2 stages of recovery with increasing temperature.

3.4.2 Medium doses: 3 and 6 dpa

SiC samples were implanted at 400 °C to a dose close to 3 dpa corresponding to a fluence of 1 x 10^{15} Xe.cm^{-2}. The XRD curves, figure 3.33, show the strain recovery with increasing annealing temperature from 1.6 % to 0.5 % at 1400 °C. Results were analyzed with an Arrhenius law giving rise to two stages of recovery as observed for the 1dpa implanted sample. The first stage (up to 1000 °C – red line) shows the activation energy E_a = 0.085 eV ± 0.005 eV similar to the first stage in low dose implanted sample (1 dpa). On the contrary, the second stage (blue line) observed at higher temperature presents activation energy E_a of 0.2 eV ± 0.05 eV which is much lower than the one observed for 1dpa. No step heights were measured in these 3dpa implanted samples.

With increasing dose to 6 dpa the decreasing in XRD intensity is observed (previous paragraph). Nevertheless, the relaxation of maximal strain is observed with increasing annealing temperature to reach 1.6 % at 1400 °C, see figure 3.36.

The analysis via an Arrhenius plot is not straightforward as shown in figure 3.36. It is possible to fit the results by considering one stage only or two stages as discussed at lower doses. Taking only one stage in the whole range of temperatures leads to the activation energy of E_a = 0.06 eV ± 0.02 eV (black dotted line in figure 3.34 - right). As suggested at lower doses, the curve can be also broken down into 2 parts revealing two stages of strain recovery with activation energies of E_a = 0.055 eV ± 0.005 eV (red line) in the low temperature regime (400 – 1000 °C) and E_a = 0.11 eV ± 0.05 eV at higher temperature (blue line).

We also note that for both doses the XRD curves again present some kind of satellite peak showing that the damage zone could be divided into different zones of strain (or different lattice parameter), i.e. different kind of point-like defects. Simulations are required to conclude.

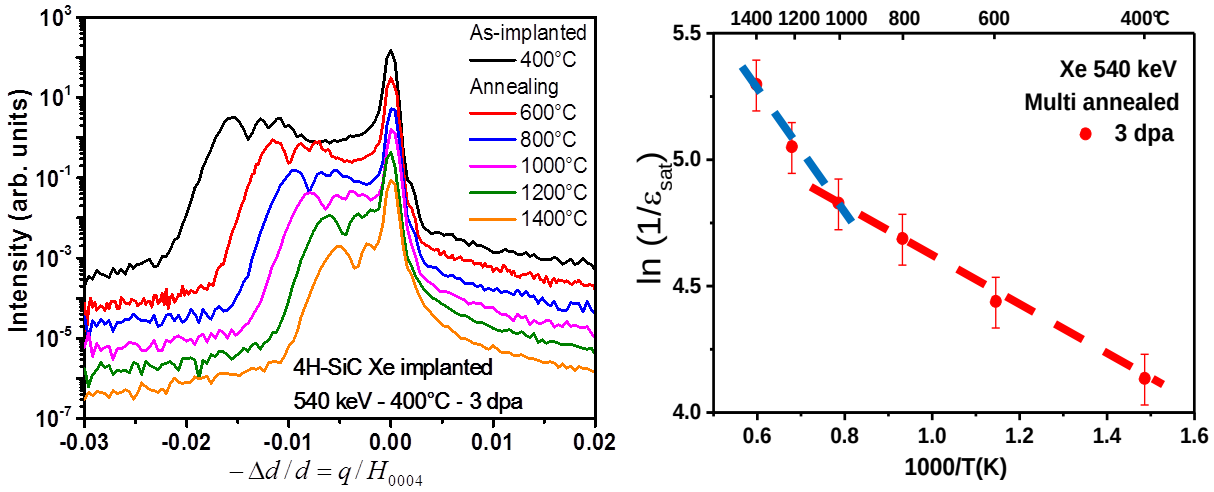


Figure 3.33: Evolution of the X-ray scattered intensity with annealing for the sample Xe-implanted at 400 °C with a dose of 3 dpa (left) - Arrhenius fit (right).

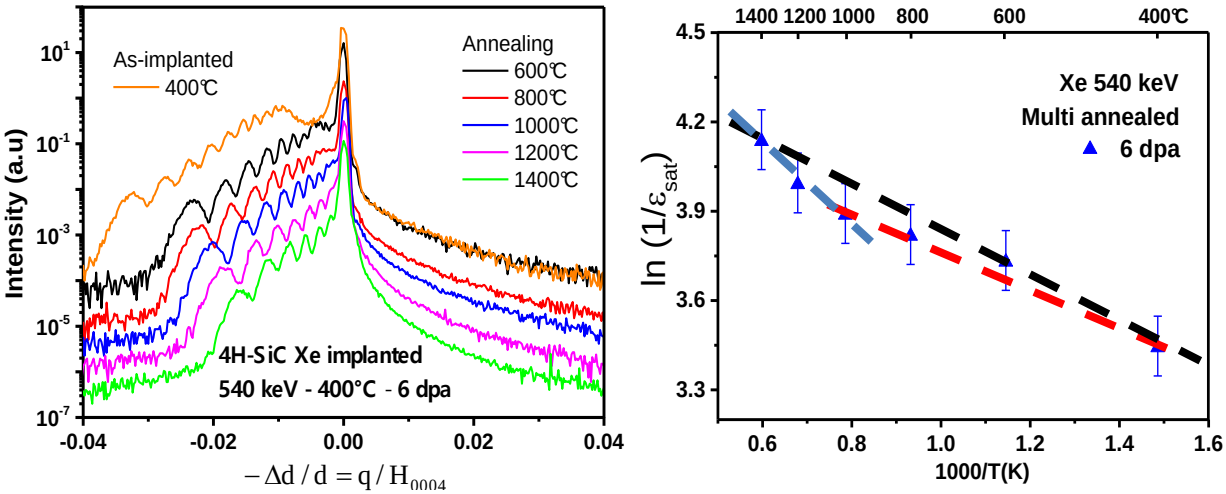


Figure 3.34: Evolution of the XRD curves with annealing for the Xe-implanted sample at 400°C with a dose of 6 dpa (left) – Tentative of Arrhenius fit (right).

Swelling and roughness evolution at 6dpa with annealing

Figure 3.35 plots the evolution of step height and roughness R_q (root mean square) with annealing temperature and the results are listed in the associated table 3.5. Once again one may ask whether the Arrhenius plots highlight two regimes as already stated for 1 dpa. This will be discussed thereafter (3.4.4). The surface roughness does not appear to change up to 1200 °C, R_q = 0.6 nm ± 0.1 nm, and then drastically decreases to ~ 0.1 nm at 1400 °C. This unexpected effect not discussed later is only ascribed to surface effects (especially to surface sublimation process). Elevated temperature implantation is known to reduce the roughness of SiC whereas a high-temperature annealing (> 1600°C) increases it [79] A roughened surface is known to lead to deleterious effects on inversion layer motilities and specific on-resistances of SiC devices [80]. A SiC cap is generally used during high-temperature annealing.

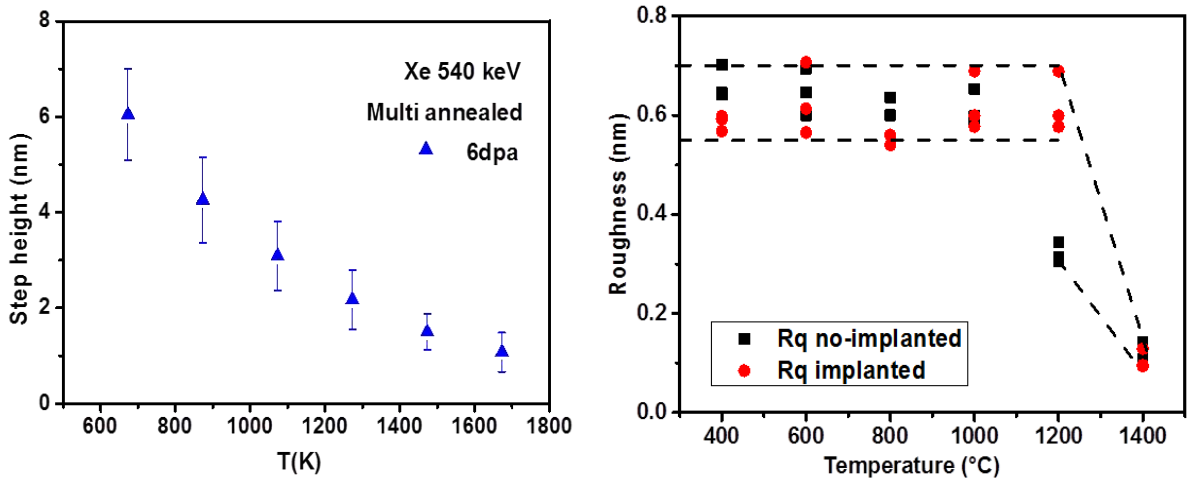


Figure 3.35: Evolution of the step height (left) and surface roughness (right) with annealing temperature for medium dose (6 dpa) implanted SiC.

Annealing temperature	Step height (nm)	swelling (%)	R_q non-implanted (nm)	R_q implanted (nm)
As-implanted 400 ºC	6.0 ± 1.0	3.0 ± 0.5	0.6 ± 0.1	0.6 ± 0.1
600 ºC	4.3 ± 0.9	2.1 ± 0.4		
800 ºC	3.1 ± 0.7	1.5 ± 0.4		
1000 ºC	2.2 ± 0.6	1.1 ± 0.3		
1200 ºC	1.5 ± 0.4	0.7 ± 0.2	0.3 ± 0.05	
1400 ºC	1.1 ± 0.4	0.5 ± 0.2	0.1 ± 0.05	

Table 3.5: The table reports the different values of swelling and roughness according to the temperature of annealing. Samples were implanted with Xe^+ at 400°C.

3.4.3 High dose: 15 dpa

It this regime of dose, the XRD curves show a strong decrease of the diffracted intensity. Even after elevated temperature annealing, only a weak restoration of the crystal is observed, see figure 3.36. Thus, no strain recovery can be measured.

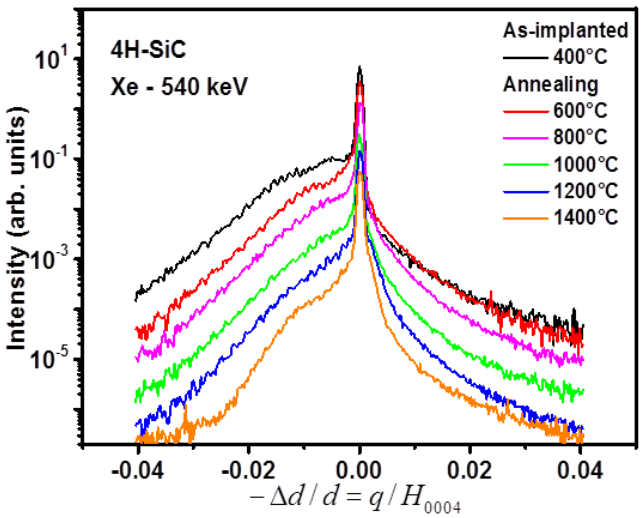
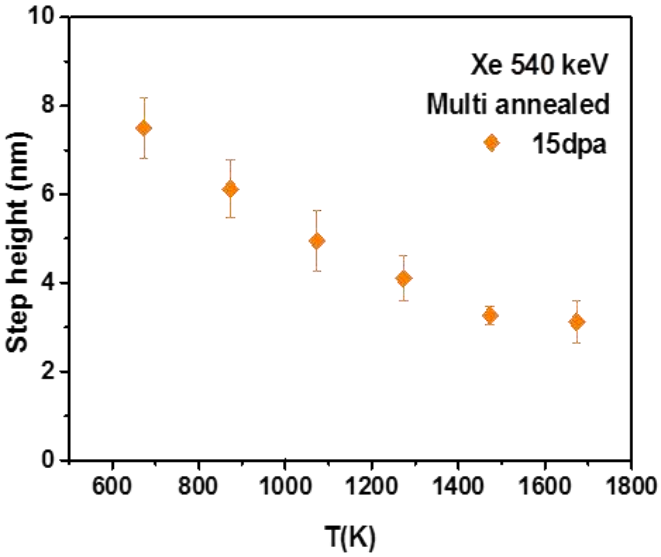


Figure 3.36: X-ray scattered intensity after thermal annealing, for the Xe-sample implanted SiC at 400 °C with a fluence of 5 x 10^{15} cm^{-2} (15 dpa).

However, the step heights could be measured. With the increasing annealing temperature, the step height is found to decrease from 7.5 nm ± 0.7 nm at 400 °C to 3.1 nm ± 0.4 nm after annealed at 1400 °C, see figure 3.37.

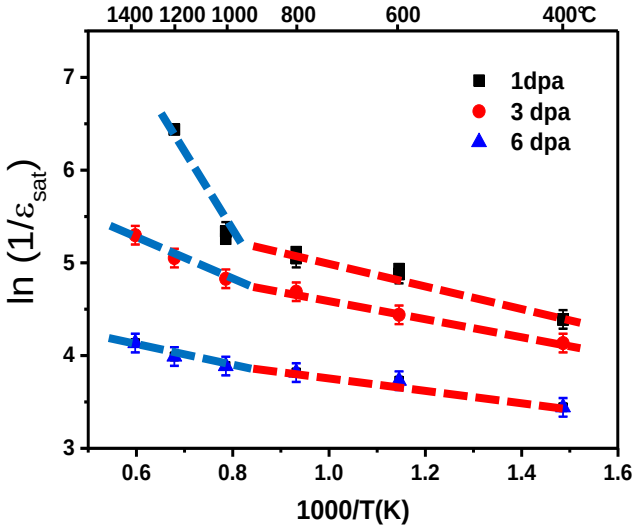


Annealing temperature	Step height (nm)	Swelling (%)
As-implanted	7.5 ± 0.7	3.7 ± 0.2
400 ºC		
600 ºC	6.1 ± 0.7	3.1 ± 0.2
800 ºC	4.9 ± 0.7	2.5 ± 0.2
1000 ºC	4.1 ± 0.5	2.1 ± 0.1
1200 ºC	3.3 ± 0.2	1.6 ± 0.1
1400 ºC	3.1 ± 0.4	1.6 ± 0.1

Figure 3.37: Evolution of the step height in high dose (15 dpa-400°C) implanted SiC with thermal annealing temperature. The table shows the measured values.

3.4.4 Discussion of strain and swelling recovery under annealing

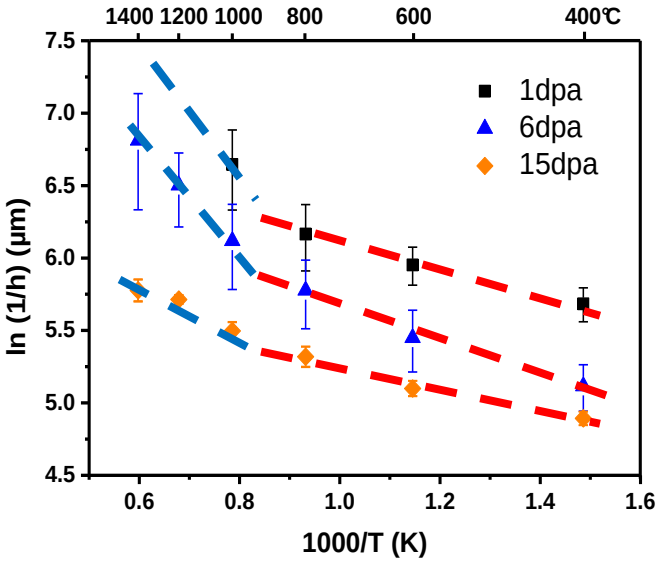
The strain relaxation under subsequent annealing for the different regimes of doses is plotted in figure 3.38, according to an Arrhenius analysis. As seen, whatever the dose the analysis seems to lead to two stages of strain recovery; the transition temperature being in the range 900 – 1000 °C. The different activation energies are listed in the associated table. We also note that the activation energies are higher in the high-temperature regime and that they decrease with dose. In addition, this decrease is more pronounced in the high-temperature regime.



Dose	E_a^1 (eV)	E_a^2 (eV)
1 dpa	0.1 ± 0.02	1 ± 0.2
3 dpa	0.08 ± 0.01	0.3 ± 0.05
6 dpa	0.06 ± 0.015	0.11 ± 0.05

Figure 3.38: Evolution of strain recovery for different doses 1, 3, and 6 dpa at 400 °C – Xe – implanted 4H-SiC. The table at right gives the activation energies (stage 1 and 2).

The step height analyzes lead to similar conclusions, namely two regimes of step reduction with a transition temperature close to 900 °C, see figure 3.39.



Dose	E_a^1 (eV)	E_a^2 (eV)
1 dpa	0.11 ± 0.02	X
6 dpa	0.1 ± 0.02	0.3 ± 0.02
15 dpa	0.07 ± 0.02	0.13 ± 0.02

Figure 3.39: Evolution of step heights after annealing on Xe – SiC samples implanted at 400 °C for different doses. The results were fitted by an Arrhenius law leading to activation energies listed in the associated table.

The damage states in the 400 °C-implanted specimen at the lowest dose of 1 dpa are expected to contain isolated point defects and possibly few defects cluster. This hypothesis is supported by the fact that the strain buildup can be modeled by the direct impact model (& 3.2). The strain relaxation in

the low-temperature stage (< 900 °C) seems to be thus primarily associated with recombination of such isolated defects. Interstitial type defects are supposed to migrate resulting in annihilation or clustering and thus leading to a decrease of the elastic strain. The migration of vacancies was observed to take place above 800 °C [81]. Close pair recombination is supposed to play the most important role in defect recovery but at a lower temperature (~ 300 K [82]). On the contrary, the probability for the annihilation of uncorrelated mobile interstitials and motionless vacancies increases with temperature. This process also shall increase with dose due to the increase in their concentration. Besides Interstitial-type defects can also form clusters acting as aggregation centers of point defects; they are known to resist annealing because of their high barrier of migration. As an example, the barrier to migration of carbon tri-interstitial cluster in cubic SiC was calculated to be larger than 4 eV [83]. The transition temperature, around 900 °C, between both stages suggests that vacancy-type defects unaffected by the recovery process in the low-temperature stage become mobile. Thus, in the first stage of annealing (from 400 °C up to 900 – 1000 °C) the elastic strain reduction is ascribing to point defect recombination and interstitial clustering. The activation energies are weak and seem to decrease with increasing dose (figure 3.38) characteristic of a process slowing suggesting that the increasing point defect concentration with dose enhances the defect clustering over the point defect recombination. In the second stage, for temperatures higher than 900 – 1000 °C where vacancies are supposed to be mobile, the elastic strain reduction is quickened and larger activation energies are estimated. Migration of vacancy-type defects is thus supposed to be operative in this regime. However, the Xe-trapping could inhibit their long-distance migration (& 3.1). Several processes may, therefore, be involved in this acceleration of strain relaxation such the migration of different types of clusters and in particular the interstitial-type clusters. Again, the decrease in the activation energy of strain reduction with dose shows that the clustering is favored over recombination.

A similar behavior of surface swelling (step height) is reported in figure 3.39, an acceleration of reduction of the step height for temperatures higher than 900 – 1000 °C. It is thus clear that the implantation-induced defects take part of swelling. Their participation is predominant at low dose (1 dpa) especially the point defects contribution since the step evolution with annealing tends towards zero (figure 3.31). With increasing dose (15 dpa) the swelling did not entirely disappear suggesting that other types of defects also contribute to surface swelling. The variations in activation energies also support the idea of different defect contributions to swelling.

Void swelling in neutron irradiated SiC is observed to start at temperature of about 1100 °C [17] and of about 1000 °C in severe helium implanted SiC [17]. The transition temperature of swelling reduction is very close suggesting similar processes. Determining the nature of defects as well as the processes associated with each stage of relaxation/recovery (strain and surface swelling) shall require more careful experimental studies in parallel with computer simulations, both of which are planned (or

in progress) in the near future. We should point out that most defects cause the cell to expand [84]. TEM observations were nevertheless performed to get a better picture of the evolution of defects under subsequent annealing.

3.4.5 TEM observations

Low dose regime: 1.5 dpa (5 x 10^{14} Xe.cm^{-2})

The TEM images figure 3.40 shows the evolution of the microstructure of Xe 400 °C - implanted SiC at 1.5 dpa in the as-implanted state (a) and after annealing at 1400 °C during 30 min (b). As already described (&3.3.1) no defects are visible in the as-implanted state suggesting that only point defects or tiny defect clusters are generated during the implantation in agreement with previous results. After annealing, a huge density of dark contrast spots is observed around the mean projected range of Xe ions. No spots are visible in the near surface region and beyond 250 nm in depth highlighting the strong interaction between ions and defects. No cavities (bubbles, voids, Xe-precipitates) are evidenced.

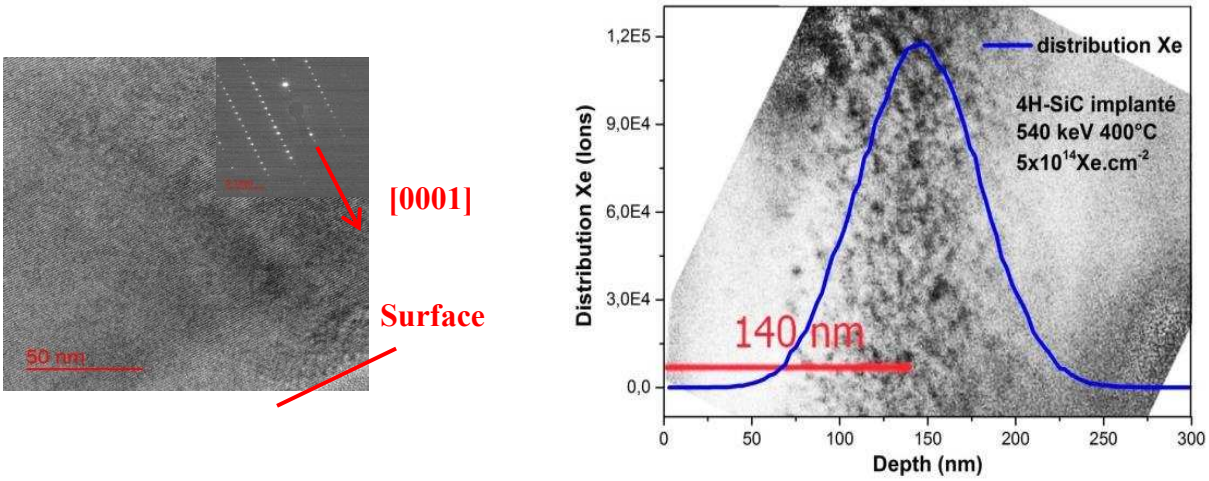


Figure 3.40: XTEM image of 400 °C as-implanted with 1.5 dpa of Xe (left), and after annealing at 1400 °C compared with the ion distribution profile simulated by SRIM (right).

It is interesting to compare with helium implantation for which a larger amount of ions in required for a similar level of damage. In He-implanted SiC at 2 dpa (50 keV) the resulting microstructure is different [56]. In the as-implanted state, a wide band of dark contrast is observed close to the maximal of deposited energy see the XTEM image shown in figure 3.41.

After annealing a layer of spherical cavities (he-bubbles of a mean diameter of 7 nm with a deviation of 2 nm) is formed around R_p~270 nm. The corresponding weak beam image (b) highlights the high density of point defects (or clusters) located in the zone of high nuclear stopping. In that respect, NG stabilizes the vacancy-type defects by reducing the dynamical recombination. Under annealing at high temperature, the relative motion of clusters is operative leading to the formation of

larger clusters of both types. In helium implanted sample the concentration of vacancy-type defects (called bubble precursor) is so high due to the large quantity of He (2 % at the maximum) that the formation of a dense and homogeneous population of bubbles located around R_p. In the near surface region in which no helium stopped, the whole strain recovery occurs and no defects are visible. For Xe implantation, the amount of gas is too small to observe such image (0.04 % at the maximum).

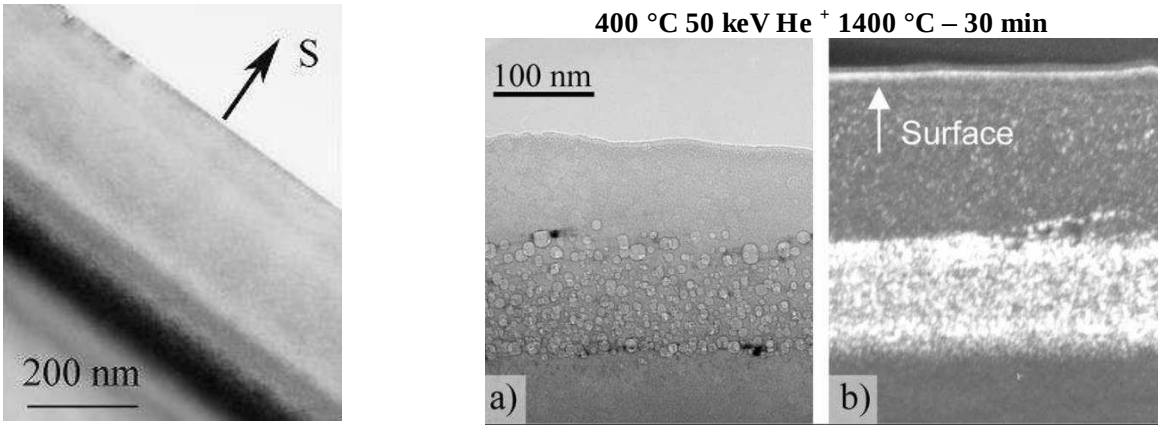


Figure 3.41: XTEM image of 400 °C as-implanted with 2 dpa of He (left), and after annealed (right) at 1400 °C (a) bright field image, (b) weak beam dark field image [56].

High dose regime 30 dpa (1 x 10^{16} Xe.cm^{-2})

To highlight the role of Xe in the stability of defects a large fluence of gas was implanted, 1x10^{16} cm^{-2} corresponding to 30 dpa, so 20 times more than the previous experience. In this high dose regime, the maximal concentration of ions is 1.2 % compared with only 0.06 % at 1.5 dpa. The figure 3.42 shows the XTEM image after annealing at 1400 °C (figure 3.27 shows the XTEM image in the as-implanted state).

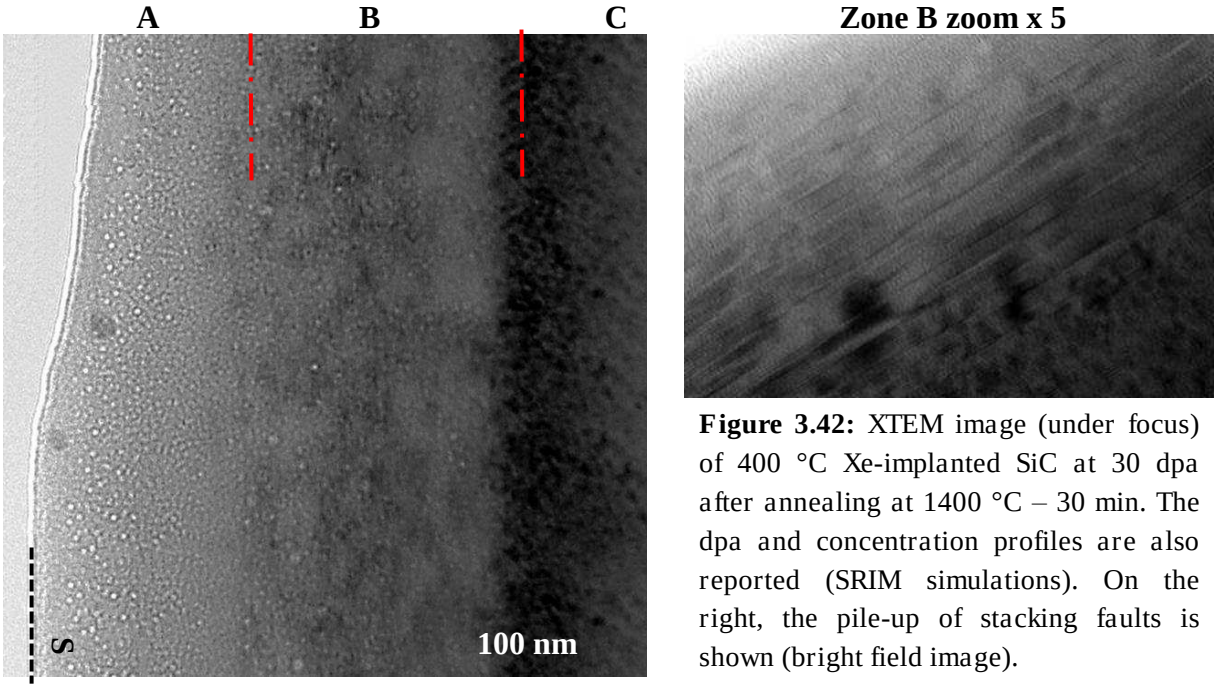


Figure 3.42: XTEM image (under focus) of 400 °C Xe-implanted SiC at 30 dpa after annealing at 1400 °C – 30 min. The dpa and concentration profiles are also reported (SRIM simulations). On the right, the pile-up of stacking faults is shown (bright field image).

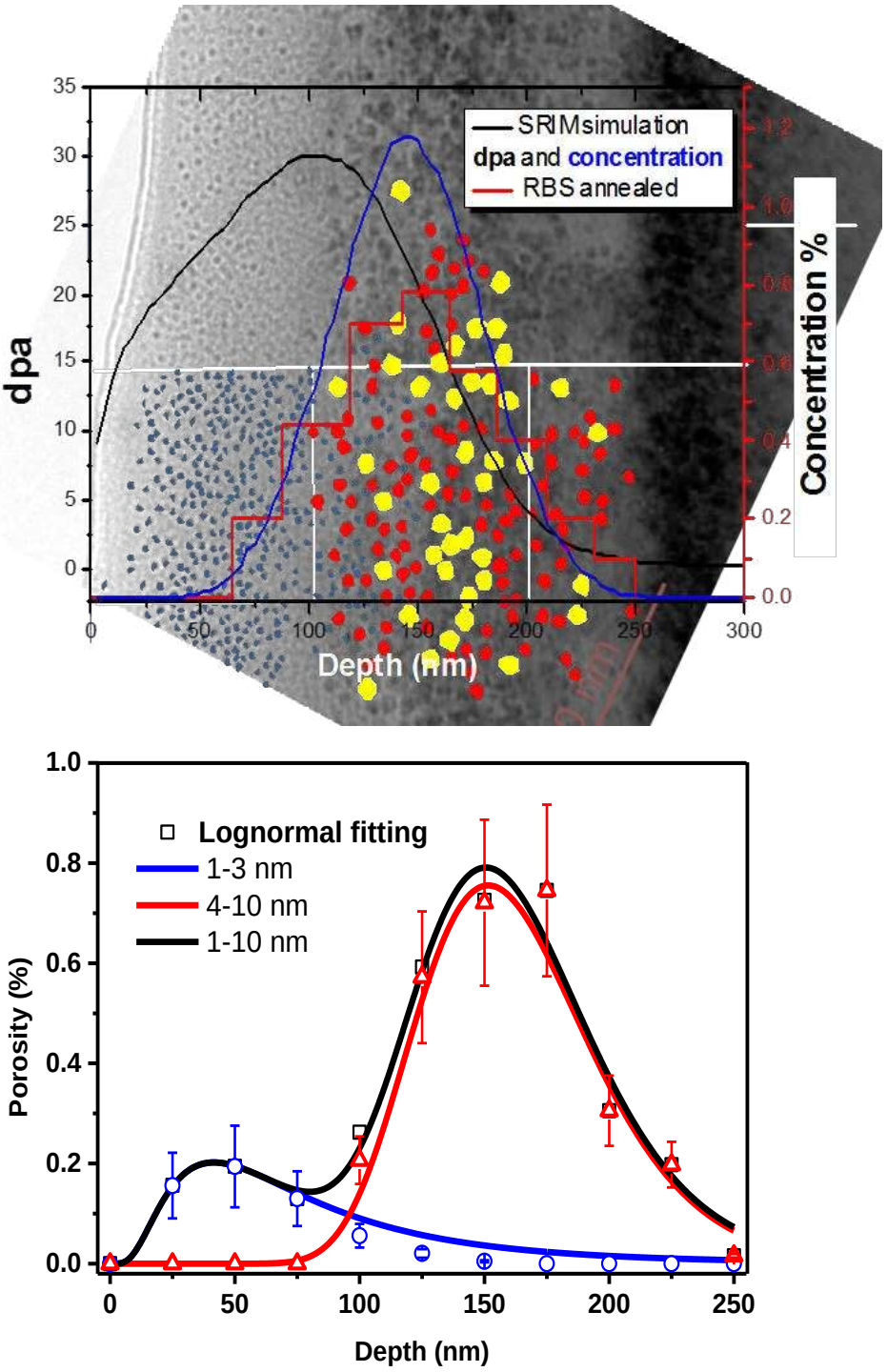


Figure 3.48: Analysis of cavities (over focus) along the Xe path. The profiles of dpa and concentration (SRIM) as well as the Xe concentration (RBS) are also reported for comparison.
(top) XTEM images showing the distribution of cavities along the Xe path. Three sizes of cavities have been distinguished (blue 1-3nm, red 4-6nm, and yellow 7-10nm).
(bottom) The porosity has been fitted by taking, for a better statistic) two populations of cavities only and then fitted according to a log-normal distribution.

This image has been analyzed by considering three different zones: zone A from the sample surface to 90 nm, zone B from 90 to 200 nm and zone C from 200 to 300 nm approximately, and then the bulk SiC. Zone A, free of visible defects before annealing shows tiny spherical cavities. Zone B, in

which the concentration of Xe is high, shows larger cavities as well as others defects as the pile-up of stacking faults (not studied in this work). The zone C, unrecognized in the as-implanted state contains a lot of dark spots. The analysis of cavities was first analyzed by considering three populations (blue, red and yellow) of cavities according to the figure 3.48.

A count of cavities was performed according to the TEM image on a surface of 300 x 250 nm^2. The cavities were counted according to their diameters: small cavities 1 - 3 nm in blue, medium cavities 4-6 nm in red and large cavities 7-10 nm in yellow. Therefore, the density of cavities and the porosity can be calculated with the quantity and the distribution of these cavities, see table 3.5. To determine the thickness of the sample, EELS experiment was carried out according to the depth, giving a linear variation (at a depth of 90nm the thickness was estimated at 130 nm). So, the densities of cavities were evaluated and the porosity versus depth determined (figure 3.43 down). As seen the total distribution is bimodal resulting of two right-skewed distributions. Both distributions were then fitted according to log-normal distribution given by:

$$P\ \ (x) = \frac{A}{\sqrt{2\pi}wx} e^{\frac{-\left[ln\frac{x}{x_c}\right]^2}{2w^2}} \qquad \textbf{(Eq. 3.11)}$$

where x_c^1 represents the maximum concentration (median) for the small cavities (1 – 3 nm), and x_c^2 for the large cavities (5 – 10 nm) and $w^{1,2}$ the shape parameter of the distribution; A reproduces the intensity of the distribution. The fitting parameters are listed in the following table 3.6. Such distribution is quite common in many fields of physics as the random growth and nucleation of nanoparticles.

Parameter lognormal fitting	x_c^1	w^1	A^1	x_c^2	w^2	A^2
	67	0.69	18.6	160	0.23	66.7

Table 3.6: Fitting parameters of the bimodal distribution of the porosity.

The analysis of the distribution parameters shows the distribution of large cavities fits the Xe-distribution calculated by using SRIM. RBS experiment confirms that no long-range Xe-diffusion occurs during annealing (red curves in figure 3.43 - top) in agreement with TDS experiments (&3.1). Note, however the difference in Xe-concentration between SRIM calculations and RBS experiments. On the contrary, the distribution of small cavities is located in the area of heavy damage and low NG concentration. These observations suggest that the small cavities are empty cavities (voids) resulting from vacancy-defects agglomeration whereas large cavities are rather full-gas cavities (bubbles or nanoparticles). STEM - HAADF experiments actually showed that the large cavities are full of gas and

not the small. Running experiments (M. F. Beaufort et al.) show that the xenon-full cavities are rather Xe-nanoparticles (solid xenon) whose the study of the structure is in progress. This is in good agreement with the estimation of the ratio of Xe inside a full-cavity that is close to one Xe for a vacancy (1 = Xe/V). All the Xe-atoms are thus supposed to be confined inside the large cavities located around the mean projected range of Xe atoms. The analysis of two cavities diameters suggests the coarsening of full cavities (via an Oswald ripening process) upon annealing whereas a homogenous distribution of voids infers for a limited coarsening.

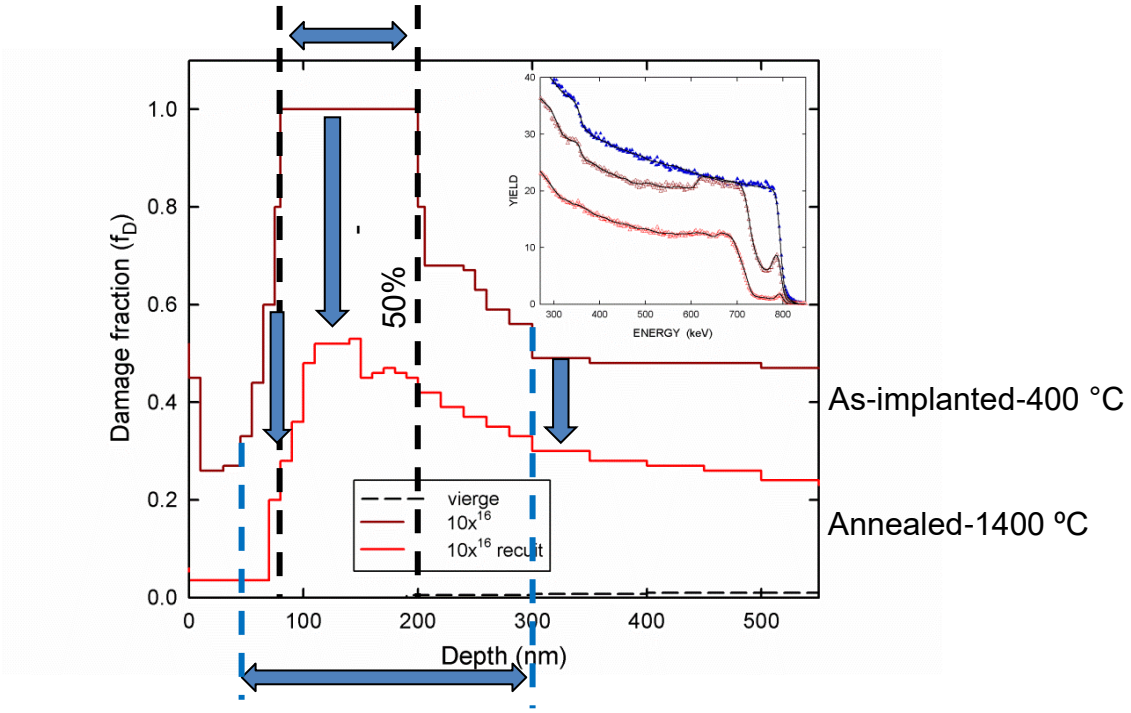


Figure 3.44: Damage fraction with depth of 400 °C Xe-implanted SiC before and after annealing (Experiments done by A. Debelle – Orsay).

The presence of defects located beyond the Xe-distribution, and extending up to 300-350 nm was not expected and remains us the EOR (End-of-Range) defects reported in semiconductors as in silicon and germanium for example. RBS experiments coupled with XRD simulations conducted on as-implanted samples (400 and 300°C, respectively), nevertheless revealed the presence of damage beyond the nuclear energy loss spectrum. They originate from the presence of a high supersaturation of “excess” Si self-interstitial atoms located just beneath the c/a interface and evolve through an Ostwald ripening process upon subsequent annealing [85]. Figure 3.44 shows that in the near surface region where voids form the damage fraction is close to zero after annealing (restoration of the crystal) and also shows the presence of defects until 300nm. In a general way, the damage fraction is reduced by a factor 2. The drift of interstitials toward the deeply damaged region under the actions of strain gradient and temperature was also reported in helium-implanted SiC [86]. Over-saturation of interstitial-type defects in the highly damaged zone upon high-temperature annealing seems to be at

the origin of both the formation of stacking faults (via the formation of Shockley partials [52]) and of the flow of free interstitials diffusing out of this region. This scenario must be confirmed by physical models. Note that these clusters of point defects may also participate in the residual swelling (as observed for the 15 dpa annealing sample) as recently studied in C- and Kr-implanted SiC [72].

3.4.6 Summary of defect evolution upon annealing

The implantation of heavy NG (Xe) in SiC leads to the formation of a damaged zone that can be divided into three different zones.

In the near-surface region, where the deposited energy is high, the strain or the damage fraction only result in small point defects or defect clusters not resolvable by TEM observation. After annealing the structure is restored via the formation or gathering or vacancy-type defects leading to the formation of tiny voids homogeneously in size but not in density. No interstitials type defects are visible.

In the stopping zone of incident Xe-atoms, the association vacancy-defects and a well as interstitial clustering highly perturb the area, close to the amorphization state from the RBS point of view. The as-resulting strain is also very high. Annealing at high temperature causes the growth of vacancy-Xe defects up to large cavities which finally are Xe-precipitates. The two populations of cavities also suggest a growth mechanism as the Ostwald ripening. The damage fraction diminishes by 50%. The interstitial-type defects invoke in the strain buildup are supposed to be at the origin of the stacking faults pile up (as reported in helium-implanted SiC under severe conditions of implantation). The drift of interstitial defects toward this zone is also a possible mechanism to reach a large I's supersaturation.

Deeper than the Xe-concentration the presence of as-resulting strain (XRD simulation) and damage fraction (RBS) suggests an implantation-assisted interstitial-defect diffusion. During annealing, they agglomerate to form larger defects visible par TEM participating in the partial restoration of the crystal.

3.5 Strain evolution for implantation at higher temperatures (400-800 °C)

For 600 and 800°C-implantation the same study was carried out, see figure 3.50. The maximum elastic strains obtained by XRD curves were plotted with increasing dose and modeled by the direct impact model (Eq. 3.4). The fitting parameters listed in table 3.6 show that the effective cross section is roughly constant whatever the temperature of implantation suggesting the production of similar defects, $\sigma_{eff.} = 6 \pm 2\ dpa^{-1}$. The values of strain at saturation are, however, temperature dependent. The energy activation was determined according an Arrhenius fitting, see figure 3.50. For

comparison results have been compared with different previous works [34], [67], [87]. As seen a good agreement is observed between the different authors.

In this low dose regime, it can say that ballistic effects are dominant effects compared to chemical effects. $\varepsilon_{max}(\mathrm{T}) = \varepsilon_{max}^{sat}(\mathrm{T})\left[1 - exp\left(-\sigma_{eff}.\emptyset\right)\right]$.

In this regime (first step) only the dynamical recombination is operative during the implantation leading to the temperature dependence of the strain at saturation.

These experiments show that the same mechanism is operative for implantation temperatures in the range (300 – 800 °C).

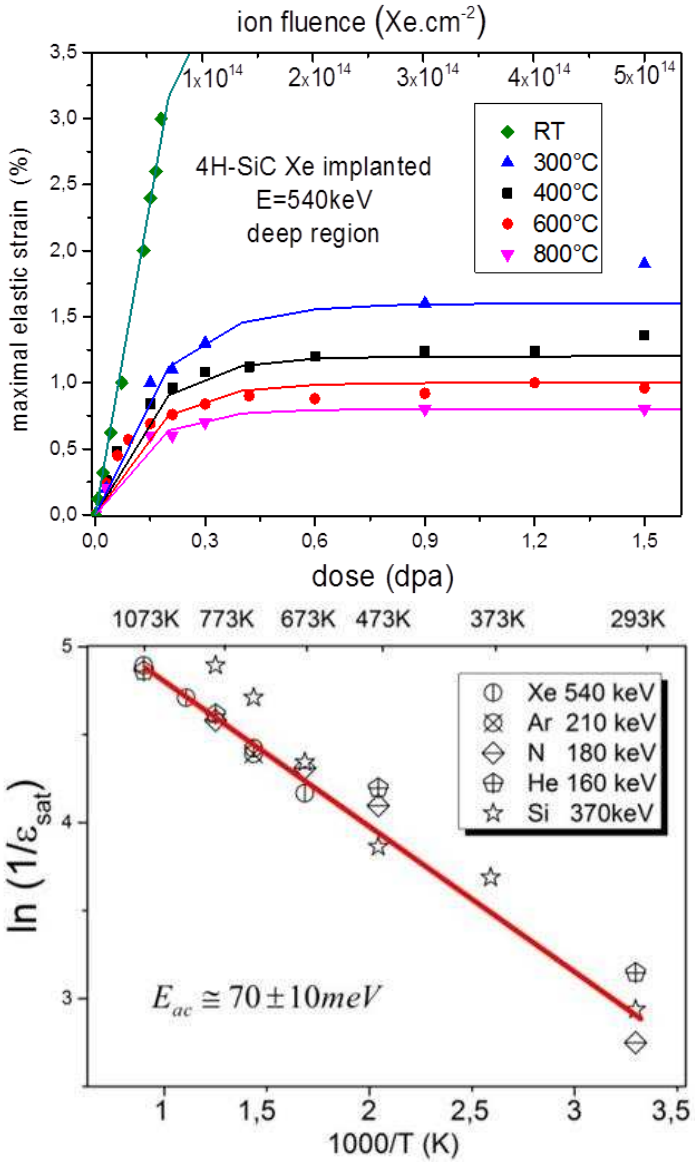


Figure 3.50: Evolution of the maximal strain $\varepsilon_{max}(\%)$ with dose in Xe implanted SiC at temperature up to 800°C. The evolution of strain is fitted according to Eq. 3.7. Arrhenius plots of different results Si[34], He[87], Ne[67].

Temperature of implantation °C	Effective cross section σ_{eff} (dpa^{-1})	Strain saturation ε_{max}^{sat} (%)
300	4	2
400	5	1.3
600	6	1.2
800	7	1.1

Table 3.6: Parameters for fitting the strain evolution at different implantation temperature.

Conclusion

Damage induced by xenon implantation into single crystals 4H-SiC has been studied as a function of implantation conditions (fluence and temperature in the range RT – 800 °C) and under subsequent thermal annealing (up to 1400 °C). XRD is a very sensitive technique to study the implantation-induced strain, it was used as the main technique. Under more severe conditions of implantation TEM observations have also been conducted. The step height measurements called surface swelling have been realized to study the indirect effects of damage on the surface. A complete amorphization transition is known to produce a surface expansion of 15 – 20 % [49]. In agreement with previous works, the amorphous transition was reported for implantation temperatures in the range 200 – 300 °C. In this low-temperature regime, the strain is supposed to result from direct impact with incident ions with a decreasing efficiency with temperature.

The implantation at 400 °C for a wide range of dose has been studied in more details. The points that need to be taken from this are that all the NG-atoms associate with vacancy-type defects to evolve under annealing into full cavities and even nano-precipitates in case of Xe-implantation. The vacancy-type defects generated in the region of high energy losses leads to the formation of empty cavities called voids. This last fact was not reported in case of helium implantation meaning that the collision cascades (more dense with the ion mass) enhance this phenomenon (as the formation of larger vacancy-type clusters …).

The implantation-induced strain (out-of-plane displacements) and its evolution under annealing were the object of a detailed study. A phenomenological approach based on pre-existing models and according to the Gibbon's approach has been developed to better understand damage accumulation and recovery microstructural evolution. It does not include the complexity of defect interaction as well as the NG-vacancy interaction dynamics. This requires a more complex (but more realistic) model that would be capable of describing and predicting damage accumulation in the dynamic regime. Nevertheless, it highlights three different regimes of strain accumulation with doses independently of incident ions and temperatures of implantation larger than T > 300 °C for 540 keV Xe ions. After a regime of linear accumulation, the strong dynamic recombination takes place leading to a saturation of strain followed by a regime of enhanced defect stability due to concomitant effects of cascade overlapping and association NG-defects. Thermal annealing up to 1400 °C shows an acceleration of the defect recovery above 900 °C suggesting the participation to strain recovery of other defects as the vacancy-type defects. The surface swelling totally disappears at low dose of implantation suggesting a point defect swelling. On the contrary, for higher doses, a residual swelling is still observed even after high-temperature annealing showing that other defects participate in the swelling.

In the implantation temperature range from RT to 800 °C the physical phenomena operating in strain buildup are the same. The transition between the different domains needs, however, to be still

studying to determine according to the NG the critical fluences of transition and its dependence on temperature. In the model developed by Wallace et al. [44], it has been found thermally activated.

This work opens up perspectives.

For validation of the proposed phenomenological model, detailed studies at different temperatures should be conducted. This was partially done on previous results obtained on helium implanted samples SiC samples up to 800 °C [88]; however, the number of data is not sufficient to definitive conclusions. The temperature dependence of parameters does be specified.

Experiments are in progress to determine the structure of the Xe-precipitates. Small Xe precipitation in silicon is known to be formed under high fluence implantation and annealing [89]. Furthermore, metals implanted with an inert gas (Ar, Xe, Kr) have revealed that they form solid fee precipitates [90]. It has been however shown that the nanometer-sized Xe-particles can change in structure under different circumstances [91]. Therefore it will be interesting to compare the structure of Xe-particles in 4H- and 3C-SiC. And what about other heavy gas? A recent study conducted on Kr-implanted 3C-SiC also revealed that the as-created cavities are filled with gas only in the region of stopping incident Kr-ions [92], but the authors did not report the formation of particles.

Another interesting study would be to monitor the synergistic effects likely to occur when Xe-cavities are submitted to displacing radiation from heavy ions accelerated under high energy. A similar study on individual He-bubbles conducted by using in situ TEM showed bubbles shrinkage concomitant with the formation of satellite tiny-bubbles close to the one previously formed [93]. This project was submitted to a PHC XU GUANGQI (collaboration Pr. C. Zhang) in 2016 but not accepted.

Reference

[1] Lely, “Sublimation process for manufacturing silicon carbide crystals,” 30-Sep-1958.

[2] V. Nikolaev, V. Shpeiwman, and B. Smiirnov, “GaN, InN, and AIN-structures and devices,” presented at the The Second Russian Workshop, St Petersburg Technical University Russia, 06-Feb-1998.

[3] L. Matus, L. Tang, M. Mehregany, D. Larkin, and P. Neudeck, “no. 137,” Inst. phys. conf. ser (UK), pp. 185–8, 1993.

[4] K. Fekade, Q. Su, M. Spencer, M. Wuttig, and P. Neudeck, “no. 137,” Inst. phys. conf. ser (UK), pp. 189–92, 1993.

[5] K. E. Spear and J. P. Dismukes, Synthetic Diamond: Emerging CVD Science and Technology, Wiley. 1994.

[6] R. M. Van Ginhoven, A. Chartier, C. Meis, W. J. Weber, and L. René Corrales, “Theoretical study of helium insertion and diffusion in 3C-SiC,” J. Nucl. Mater., vol. 348, no. 1, pp. 51–59, Jan. 2006.

[7] J. Wong-Leung, M. K. Linnarsson, B. G. Svensson, and D. J. H. Cockayne, “Ion-implantation-induced extended defect formation in (0001) and (1120) 4 H − SiC,” Phys. Rev. B, vol. 71, no. 16, Apr. 2005.

[8] M. Skowronski and S. Ha, “Degradation of hexagonal silicon-carbide-based bipolar devices,” J. Appl. Phys., vol. 99, no. 1, p. 011101, Jan. 2006.

[9] V. Heera, D. Panknin, and W. Skorupa, “p-Type doping of SiC by high dose Al implantation—problems and progress,” Appl. Surf. Sci., vol. 184, no. 1, pp. 307–316, Dec. 2001.

[10] M. Bruel, “Silicon on insulator material technology,” Electron. Lett., vol. 31, no. 14, pp. 1201–1202, Jul. 1995.

[11] L. D. Cioccio, Y. L. Tiec, F. Letertre, C. Jaussaud, and M. Bruel, “Silicon carbide on insulator formation using the Smart Cut process,” Electron. Lett., vol. 32, no. 12, pp. 1144–1145, Jun. 1996.

[12] S. Milita et al., “X-ray diffraction imaging investigation of silicon carbide on insulator structures,” Appl. Phys. A, vol. 75, no. 5, pp. 621–627, Nov. 2002.

[13] G. Celler, “SOI: Developments, Challenges, and Applications.” [Online]. Available: http://gme.tuwien.ac.at/forum2003/filter.php3?datei=Celler.htm. [Accessed: 01-Aug-2017].

[14] S. Tongay, M. Lemaitre, J. Fridmann, A. F. Hebard, B. P. Gila, and B. R. Appleton, “Drawing graphene nanoribbons on SiC by ion implantation,” Appl. Phys. Lett., vol. 100, no. 7, p. 073501, Feb. 2012.

[15] M. L. Diallo et al., “Fe-implanted 6H-SiC: Direct evidence of Fe 3Si nanoparticles observed by atom probe tomography and 57Fe Mössbauer spectroscopy,” J. Appl. Phys., vol. 117, no. 18, p. 183907, May 2015.

[16] S. E. Donnelly and J. H. Evans, Fundamental Aspects of Inert Gases in Solids. .

[17] Y. Katoh, L. L. Snead, T. Nozawa, N. B. Morley, and W. E. Windes, "Advanced radiation-resistant ceramic composites," in Advances in Science and Technology, 2006, vol. 45, pp. 1915–1924.

[18] L. L. Snead, Y. Katoh, and S. Connery, "Swelling of SiC at intermediate and high irradiation temperatures," J. Nucl. Mater., vol. 367–370, pp. 677–684, Aug. 2007.

[19] J. Chen, P. Jung, and H. Trinkaus, "Microstructural evolution of helium-implanted α-SiC," Phys. Rev. B, vol. 61, no. 19, p. 12923, 2000.

[20] E. Oliviero et al., "Formation of bubbles by high dose He implantation in 4H–SiC," J. Appl. Phys., vol. 91, no. 3, pp. 1179–1186, Feb. 2002.

[21] "ITER - the way to new energy," ITER. [Online]. Available: http://www.iter.org. [Accessed: 01-Sep-2017].

[22] T. J. Gerczak, J. D. Hunn, R. A. Lowden, and T. R. Allen, "SiC layer microstructure in AGR-1 and AGR-2 TRISO fuel particles and the influence of its variation on the effective diffusion of key fission products," J. Nucl. Mater., vol. 480, pp. 257–270, Nov. 2016.

[23] P. Hosemann et al., "Mechanical characteristics of SiC coating layer in TRISO fuel particles," J. Nucl. Mater., vol. 442, no. 1, pp. 133–142, Nov. 2013.

[24] J. Deng, H. Ko, P. Demkowicz, D. Morgan, and I. Szlufarska, "Grain boundary diffusion of Ag through polycrystalline SiC in TRISO fuel particles," J. Nucl. Mater., vol. 467, Part 1, pp. 332–340, Dec. 2015.

[25] H. Nabielek, P. E. Brown, and P. Offermann, "Silver Release from Coated Particle Fuel," Nucl. Technol., vol. 35, no. 2, pp. 483–493, Sep. 1977.

[26] J. B. Malherbe, "Diffusion of fission products and radiation damage in SiC," J. Phys. Appl. Phys., vol. 46, no. 47, p. 473001, 2013.

[27] C. J. McHargue and J. M. Williams, "Ion implantation effects in silicon carbide," Nucl. Instrum. Methods Phys. Res. Sect. B Beam Interact. Mater. At., vol. 80, pp. 889–894, Jan. 1993.

[28] A. Debelle et al., "Characterization and modelling of the ion-irradiation induced disorder in 6H-SiC and 3C-SiC single crystals," J. Phys. Appl. Phys., vol. 43, no. 45, p. 455408, 2010.

[29] J. Li et al., "Evolution of amorphization and nanohardness in SiC under Xe ion irradiation," J. Nucl. Mater., vol. 454, no. 1–3, pp. 173–177, Nov. 2014.

[30] E. Friedland, "Investigation of amorphization energies for heavy ion implants into silicon carbide at depths far beyond the projected ranges," Nucl. Instrum. Methods Phys. Res. Sect. B Beam Interact. Mater. At., vol. 391, pp. 10–13, Jan. 2017.

[31] W. J. Weber, L. Wang, Y. Zhang, W. Jiang, and I.-T. Bae, "Effects of dynamic recovery on amorphization kinetics in 6H-SiC," Nucl. Instrum. Methods Phys. Res. Sect. B Beam Interact. Mater. At., vol. 266, no. 12, pp. 2793–2796, Jun. 2008.

[32] S. Leclerc, M. F. Beaufort, J. F. Barbot, and A. Declémy, "Strain and amorphization under light-ion implantation in SiC," EPL Europhys. Lett., vol. 98, no. 4, p. 46001, May 2012.

[33] W. Jiang, W. J. Weber, S. Thevuthasan, and V. Shutthanandan, “Accumulation and recovery of disorder on silicon and carbon sublattices in ion-irradiated 6H–SiC,” J. Nucl. Mater., vol. 289, no. 1, pp. 96–101, Feb. 2001.

[34] R. Héliou, J. L. Brebner, and S. Roorda, “Role of implantation temperature on residual damage in ion-implanted 6H-SiC,” Semicond. Sci. Technol., vol. 16, no. 10, p. 836, 2001.

[35] W. Jiang, W. J. Weber, S. Thevuthasan, and D. E. McCready, “Damage formation and recovery in C+-irradiated 6H–SiC,” Nucl. Instrum. Methods Phys. Res. Sect. B Beam Interact. Mater. At., vol. 148, no. 1, pp. 562–566, Jan. 1999.

[36] W. J. Weber, L. M. Wang, N. Yu, and N. J. Hess, “Structure and properties of ion-beam-modified (6H) silicon carbide,” Mater. Sci. Eng. A, vol. 253, no. 1, pp. 62–70, 1998.

[37] F. F. J. Morehead and B. L. Crowder, “A model for the formation of amorphous Si by ion bombardment,” Radiat. Eff., vol. 6, no. 1, pp. 27–32, Jan. 1970.

[38] W. J. Weber, “Models and mechanisms of irradiation-induced amorphization in ceramics,” Nucl. Instrum. Methods Phys. Res. Sect. B Beam Interact. Mater. At., vol. 166–167, pp. 98–106, 2000.

[39] J. F. Gibbons, “Ion implantation in semiconductors #8212;Part II: Damage production and annealing,” Proc. IEEE, vol. 60, no. 9, pp. 1062–1096, Sep. 1972.

[40] J. Jagielski and L. Thomé, “Multi-step damage accumulation in irradiated crystals,” Appl. Phys. A, vol. 97, no. 1, pp. 147–155, Oct. 2009.

[41] L. Thomé, S. Moll, G. Sattonnay, L. Vincent, F. Garrido, and J. Jagielski, “Radiation effects in cubic zirconia: A model system for ceramic oxides,” J. Nucl. Mater., vol. 389, no. 2, pp. 297–302, May 2009.

[42] A. Debelle, A. Boulle, A. Chartier, F. Gao, and W. J. Weber, “Interplay between atomic disorder, lattice swelling, and defect energy in ion-irradiation-induced amorphization of SiC,” Phys. Rev. B, vol. 90, no. 17, Nov. 2014.

[43] W. Jiang, Y. Zhang, and W. J. Weber, “Temperature dependence of disorder accumulation and amorphization in Au-ion-irradiated 6 H − Si C,” Phys. Rev. B, vol. 70, no. 16, Oct. 2004.

[44] J. B. Wallace, L. B. Bayu Aji, T. T. Li, L. Shao, and S. O. Kucheyev, “Damage buildup in Ar-ion-irradiated 3 C -SiC at elevated temperatures,” J. Appl. Phys., vol. 118, no. 10, p. 105705, Sep. 2015.

[45] A. Höfgen, V. Heera, F. Eichhorn, and W. Skorupa, “Annealing and recrystallization of amorphous silicon carbide produced by ion implantation,” J. Appl. Phys., vol. 84, no. 9, pp. 4769–4774, Oct. 1998.

[46] W. Jiang, W. J. Weber, S. Thevuthasan, and D. E. McCready, “Damage accumulation and annealing in 6H–SiC irradiated with Si+,” Nucl. Instrum. Methods Phys. Res. Sect. B Beam Interact. Mater. At., vol. 143, no. 3, pp. 333–341, Sep. 1998.

[47] V. Heera et al., “Density and structural changes in SiC after amorphization and annealing,” Appl. Phys. Lett., vol. 70, pp. 3531–3533, Jun. 1997.

[48] E. Oliviero, “Défauts induits par l’implantation d’hélium dans les matériaux à base silicium,” Université de Poitiers, 2001.

[49] S. Leclerc, “Damage induced by Helium implantation in silicon carbide,” Université de Poitiers, 2007.

[50] E. Oliviero et al., “Damage formation and recovery in temperature helium implanted 4H–SiC,” Mater. Sci. Eng. B, vol. 102, no. 1–3, pp. 289–292, Sep. 2003.

[51] S. Leclerc, M. F. Beaufort, A. Declémy, and J. F. Barbot, “Evolution of defects upon annealing in He-implanted 4H-SiC,” Appl. Phys. Lett., vol. 93, no. 12, p. 122101, Sep. 2008.

[52] M. Texier, B. Pichaud, M.-F. Beaufort, and J.-F. Barbot, “Structural disordering and extended defects produced by He-implantation in silicon carbide,” J. Phys. Appl. Phys., vol. 46, no. 48, p. 485105, 2013.

[53] J. F. Barbot et al., “Helium implantation into 4H-SiC,” Phys. Status Solidi A, vol. 206, pp. 1916–1923, 2009.

[54] J. Li, L. Porter, and S. Yip, “Atomistic modeling of finite-temperature properties of crystalline b-SiC II. Thermal conductivity and effects of point defects,” J. Nucl. Mater., vol. 255, pp. 139–152, 1998.

[55] S. Leclerc, A. Declémy, M. F. Beaufort, C. Tromas, and J. F. Barbot, “Swelling of SiC under helium implantation,” J. Appl. Phys., vol. 98, no. 11, p. 113506, Dec. 2005.

[56] J. F. Barbot, M. F. Beaufort, M. Texier, and C. Tromas, “Swelling and stacking fault formation in helium implanted SiC,” J. Nucl. Mater., vol. 413, no. 3, pp. 162–165, Jun. 2011.

[57] J. F. Barbot, M. F. Beaufort, and V. Audurier, “Effects of Helium Implantation on the Mechanical Properties of 4H-SiC,” Mater. Sci. Forum, vol. 645–648, pp. 721–724, 2010.

[58] C. Tromas, V. Audurier, S. Leclerc, M. F. Beaufort, A. Declémy, and J. F. Barbot, “Evolution of mechanical properties of SiC under helium implantation,” J. Nucl. Mater., vol. 373, no. 1–3, pp. 142–149, Feb. 2008.

[59] J.-F. Barbot, M.-F. Beaufort, and A. Declémy, “Strain build-up in SiC implanted at different temperatures,” Nucl. Instrum. Methods Phys. Res. Sect. B Beam Interact. Mater. At., vol. 327, pp. 59–62, May 2014.

[60] J. J. Li et al., “Lattice damage and nanohardness in 6H–SiC implanted with multiple-energy Xe ions,” Nucl. Instrum. Methods Phys. Res. Sect. B Beam Interact. Mater. At., vol. 286, pp. 124–128, Sep. 2012.

[61] J. F. Ziegler, M. D. Ziegler, and J. P. Biersack, “SRIM : the stopping and range of ions in matter,” CERN Document Server, 2008. [Online]. Available: http://cds.cern.ch/record/1525729. [Accessed: 29-Aug-2017].

[62] G. Lucas and L. Pizzagalli, “Ab initio,” Phys. Rev. B, vol. 72, no. 16, p. 161202, Oct. 2005.

[63] Aboalbiss, *Bragg’s law*. 2009.

[64] Stepanov, “Dynamical x-ray diffraction from multilayers on the Web.” [Online]. Available: http://sergey.gmca.aps.anl.gov/gid_sl.html. [Accessed: 30-Aug-2017].

[65] N. Sousbie, L. Capello, J. Eymery, F. Rieutord, and C. Lagahe, “X-ray scattering study of hydrogen implantation in silicon,” J. Appl. Phys., vol. 99, no. 10, p. 103509, May 2006.

[66] M. F. Beaufort, F. Pailloux, A. Declémy, and J. F. Barbot, “Transmission electron microscopy investigations of damage induced by high energy helium implantation in 4H–SiC,” J. Appl. Phys., vol. 94, no. 11, pp. 7116–7120, Dec. 2003.

[67] M. Amigou, M. F. Beaufort, A. Declémy, S. Leclerc, and J. F. Barbot, “Strain Measurements on Nitrogen Implanted 4H-SiC,” Mater. Sci. Forum, vol. 679–680, pp. 185–188, Mar. 2011.

[68] F. Linez, E. Gilabert, A. Debelle, P. Desgardin, and M.-F. Barthe, “Helium interaction with vacancy-type defects created in silicon carbide single crystal,” J. Nucl. Mater., vol. 436, no. 1–3, pp. 150–157, May 2013.

[69] E. Friedland and N. G. van der Berg, “Influence of radiation damage on the thermal properties of silicon carbide implanted with heavy noble gas ions,” Nucl. Instrum. Methods Phys. Res. Sect. B Beam Interact. Mater. At., vol. 371, no. Supplement C, pp. 240–244, Mar. 2016.

[70] A. Charaf Eddin and L. Pizzagalli, “First principles calculation of noble gas atoms properties in 3C–SiC,” J. Nucl. Mater., vol. 429, no. 1–3, pp. 329–334, Oct. 2012.

[71] P. H. Dederichs, “The theory of diffuse X-ray scattering and its application to the study of point defects and their clusters,” J. Phys. F Met. Phys., vol. 3, no. 2, p. 471, 1973.

[72] B. Tyburska-Püschel et al., “Size distribution of black spot defects and their contribution to swelling in irradiated SiC,” J. Nucl. Mater., vol. 476, pp. 132–139, Aug. 2016.

[73] W. J. Weber, N. Yu, L. M. Wang, and N. J. Hess, “Temperature and dose dependence of ion-beam-induced amorphization in α-SiC,” J. Nucl. Mater., vol. 244, no. 3, pp. 258–265, Apr. 1997.

[74] W. J. Weber, Y. Zhang, and L. Wang, “Review of dynamic recovery effects on ion irradiation damage in ionic-covalent materials,” Nucl. Instrum. Methods Phys. Res. Sect. B Beam Interact. Mater. At., vol. 277, pp. 1–5, Apr. 2012.

[75] P. Musumeci, L. Calcagno, M. G. Grimaldi, and G. Foti, “Optical defects in ion damaged 6H-silicon carbide,” Nucl. Instrum. Methods Phys. Res. Sect. B Beam Interact. Mater. At., vol. 116, no. 1–4, pp. 327–331, 1996.

[76] T. Bus et al., “Thermal recovery of amorphous zones in 6H-SiC and 3C-SiC induced by low fluence 420 keV Xe irradiation,” Mater. Sci. Eng. B, vol. 102, no. 1–3, pp. 269–276, Sep. 2003.

[77] F. Gao and W. J. Weber, “Computer simulation of disordering and amorphization by Si and Au recoils in 3C–SiC,” J. Appl. Phys., vol. 89, no. 8, pp. 4275–4281, Apr. 2001.

[78] L. Pizzagalli, A. Charaf-Eddin, and S. Brochard, “Numerical simulations and modeling of the stability of noble gas atoms in interaction with vacancies in silicon,” Comput. Mater. Sci., vol. 95, pp. 149–158, Dec. 2014.

[79] C. F. Zhe, Silicon Carbide: Materials, Processing & Devices. CRC Press, 2003.

[80] S. G. Sundaresan et al., “Ultra-low resistivity Al+ implanted 4H–SiC obtained by microwave annealing and a protective graphite cap,” Solid-State Electron., vol. 52, no. 1, pp. 140–145, Jan. 2008.

[81] W. Puff, P. Mascher, A. G. Balogh, and H. Baumann, “Vacancy-Type Defects in Proton-Irradiated SiC,” Mater. Sci. Forum, vol. 258–263, pp. 733–738, 1997.

[82] Z. Rong, F. Gao, W. J. Weber, and G. Hobler, “Monte Carlo simulations of defect recovery within a 10 keV collision cascade in 3C–SiC,” J. Appl. Phys., vol. 102, no. 10, p. 103508, Nov. 2007.

[83] H. Jiang, C. Jiang, D. Morgan, and I. Szlufarska, “Accelerated atomistic simulation study on the stability and mobility of carbon tri-interstitial cluster in cubic SiC,” Comput. Mater. Sci., vol. 89, pp. 182–188, Jun. 2014.

[84] J. Li, L. Porter, and S. Yip, “Atomistic modeling of finite-temperature properties of crystalline β-SiC: II. Thermal conductivity and effects of point defects,” J. Nucl. Mater., vol. 255, no. 2, pp. 139–152, Jun. 1998.

[85] C. Bonafos, D. Mathiot, and A. Claverie, “Ostwald ripening of end-of-range defects in silicon,” J. Appl. Phys., vol. 83, no. 6, pp. 3008–3017, Mar. 1998.

[86] S. Leclerc, M. F. Beaufort, A. Declémy, and J. F. Barbot, “Strain-induced drift of interstitial atoms in SiC implanted with helium ions at elevated temperature,” J. Nucl. Mater., vol. 397, no. 1–3, pp. 132–134, Feb. 2010.

[87] J. F. Barbot et al., “Strain Build-Up, Swelling and Stacking Fault Formation in Implanted 4H-SiC,” Mater. Sci. Forum, vol. 717–720, pp. 485–488, May 2012.

[88] J. F. Barbot, A. Declémy, and M.-F. Beaufort, “Damage accumulation in He implanted SiC at different temperatures,” Phys. Status Solidi A, vol. 210, no. 1, pp. 218–221, Jan. 2013.

[89] C. Templier, B. Boubeker, H. Garem, E. L. Mathé, and J. C. Desoyer, “Precipitation of implanted xenon in silicon,” Phys. Status Solidi A, vol. 92, no. 2, pp. 511–516, Dec. 1985.

[90] S. E. Donnelly and C. J. Rossouw, “Lattice images of inert gas bubbles in aluminium,” Nucl. Instrum. Methods Phys. Res. Sect. B Beam Interact. Mater. At., vol. 13, no. 1, pp. 485–489, Mar. 1986.

[91] M. Song, K. Mitsuishi, K. Furuya, C. W. Allen, R. C. Birtcher, and S. E. Donnelly, “Structure of nanometre-sized Xe particles embedded in Al crystals,” J. Microsc., vol. 215, no. 3, pp. 224–229, Sep. 2004.

[92] H. Zang et al., “Vacancy effects on the formation of He and Kr cavities in 3C-SiC irradiated and annealed at elevated temperatures,” Nucl. Instrum. Methods Phys. Res. Sect. B Beam Interact. Mater. At., vol. 389–390, pp. 40–47, Dec. 2016.

[93] M.-F. Beaufort, M. Vallet, J. Nicolaï, E. Oliviero, and J.-F. Barbot, “In-situ evolution of helium bubbles in SiC under irradiation,” J. Appl. Phys., vol. 118, no. 20, p. 205904, Nov. 2015.

Résumé

Le carbure de silicium (SiC) est un matériau qui est considéré comme un semi-conducteur à large bande interdite ou une céramique suivant ses applications en microélectronique ou comme matériau nucléaire. Dans ces deux domaines d'application les défauts générés par l'implantation/irradiation d'ions (dopage, matériau de structure) doivent être contrôlés. Ce travail est une étude des défauts générés par l'implantation de gaz rares suivant les conditions d'implantation (fluence et température). La déformation élastique a plus particulièrement été étudiée dans le cas d'implantation de xénon à des températures pour lesquelles la recombinaison dynamique empêche la transition amorphe. Un modèle phénoménologique basé sur le recouvrement des cascades a été proposé pour comprendre l'évolution de la déformation maximale avec la dose. Des observations complémentaires en particulier par microscopie électronique à transmission nous ont permis de préciser la nature des défauts créés et d'étudier leur évolution sous recuit. La formation de cavités a été observée pour des conditions sévères d'implantation/recuit ; ces cavités sont de nature différente (vide ou pleine) suivant la répartition du xénon. Cette étude est également reliée aux propriétés de gonflement sous irradiation, gonflement qui doit être anticipé dans les domaines d'application du SiC.

Mots clefs : SiC, implantation ionique, dégâts, déformation élastique, cavités, gonflement

Abstract

Silicon carbide is a material that can be considered as a wide band gap semiconductor or as a ceramic according to its applications in microelectronics and in nuclear energy system (fission and fusion). In both fields of application defects or damage induced by ion implantation/ irradiation (doping, material structure) should be controlled. This work is a study of defects induced by noble gas implantation according to the implantation conditions (fluence and temperature). The elastic strain buildup, particularly in the case of xenon implantation, has been studied at elevated temperatures for which the dynamic recombination prevents the amorphization transition. A phenomenological model based on cascade recovery has been proposed to understand the strain evolution with increasing dose and for different noble gases. In addition, with the help of transmission electron microscopy, the evolution of defects under subsequent annealing was studied. The formation of nanocavities was observed under severe implantation/annealing conditions. These cavities are of different nature (full of gas or empty) according to the xenon and damage distribution. This study is also linked to swelling properties under irradiation that should be projected in the SiC application fields.

Keywords: SiC, ion implantation, damages, elastic strain, cavities, swelling